Spin Resonance Excitation of Gd-Based Contrast Agents for Thermal Energy Deposition

Steven Conrad Dinger

A thesis submitted to the Faculty of Engineering and the Built Environment, University of the Witwatersrand, Johannesburg, in fulfilment of the requirements for the degree of Doctor of Philosophy.

Johannesburg, 2016

DECLARATION

I declare that this thesis is my own unaided work. It is being submitted for the Degree of Doctor of Philosophy at the University of the Witwatersrand, Johannesburg. It has not been submitted before for any degree or examination to any other University.

....
(Signature of Candidate)

...............day of..................year....2016....

ABSTRACT

The theoretical and experimental investigation of electron spin-resonance relaxation to deposit thermal energy into liquid gadolinium-based contrast agents for cancer hyperthermia treatment is presented. Previous works suggest that using protons in water are inadequate, with a thermal deposition rate of approximately 1 °C per two years. A novel component of this research relies on the use of gadolinium-chelated molecules, which are currently used as contrast agents in clinical MRI scans. The chelating agents, or ligands, investigated are Gadobenate (MultiHance®), Gadopentetate (Magnevist®), Gadoterate (Dotarem®) and Gadoteridol (ProHance®). The gadolinium atom has seven unpaired electrons in its inner f shell orbital and as a result has a 660 times stronger paramagnetic response when placed in an external magnetic field. The research tests the hypothesis that by using an appropriate external homogeneous DC magnetic field, together with a radiofrequency excited resonator, that a measurable amount of thermal energy is deposited into a liquid gadolinium-based contrast agent. The aim of this research is to ultimately discover a new cancer hyperthermia treatment. The research theory suggests that a temperature rate of 13.4 $°\mathrm{C} \cdot \mathrm{s}^{-1}$ can be achieved using the gadolinium-based contrast agents under certain experimental conditions, and a maximum of 29.4 $°\mathrm{C} \cdot \mathrm{s}^{-1}$ under more optimal conditions. The temperature rates are calculated using parameter values commonly found in literature and practice. The simulation and design of the DC magnetic field coil system is discussed, together with the simulation results and design parameters of the radiofrequency loop-gap resonator. The experimental results and analysis indicate that the selected contrast agents have varied responses based on their chemical nature and that only two out of the four contrast agents, Dotarem and ProHance, show a measurable effect albeit sufficiently small that statistical techniques were necessary to distinguish the effect from background. A model fit to the data is performed in order to determine the spin-lattice relaxation time of the contrast agents under the specified experimental conditions. The model estimate is significantly smaller than the values found in literature under similar conditions, with a spin-lattice relaxation time τ_{1e} of approximately 0.2 ps compared to the literature value of 0.1 ns. Although the observed electron spin resonance heating rate is in the milli-Watt range it is still notably larger (167 000 times) compared to the heating rate obtained using protons. The low temperature rates suggest that a more suitable agent or molecule with a larger spin-relaxation time be used, in order to achieve clinical useful temperature rates in the range of 14 $°\mathrm{C} \cdot \mathrm{s}^{-1}$.

ACKNOWLEDGEMENTS

The research presented in this thesis was performed under the Biomedical Engineering Research Group within the School of Electrical & Information Engineering at the University of Witwatersrand, Johannesburg. The research was funded by the School of Electrical & Information Engineering and the Biomedical Engineering Research Group.

The author would like to acknowledge and thank the following people and departments for their advice, support and guidance throughout the research period:

> David M. Rubin and Brian Wigdorowitz as supervisors, for their continued support in the hypothesis behind this research and for their facilitation of the project.
>
> Famabirai Takawira, as head of the School of Electrical & Information Engineering, for funding this project and allowing access to the necessary equipment and facilities within the department.
>
> Keagan Malan and Mark Goossens for their assistance in design and construction of the DC coil magnetic field system.
>
> Alan Clark for use of the anechoic chamber and radiofrequency equipment used in experimentation.
>
> Chris Vale for his expert advice and support in designing the radiofrequency components used for experimentation.
>
> Llewellyn Holt, Marc Slabbert, Valérie Bousson and Guillaume Haïat for the procurement of contrast agents.
>
> Jonathan Keartland for his interest and advice on magnetic resonance.
>
> Sebastian Rast and Lothar Helm for their detailed discussions on the characteristics of electron spin resonance.
>
> My loved ones and friends for their continuous support and patience throughout the entire process.

Contents

LIST OF FIGURES

LIST OF TABLES

LIST OF SYMBOLS

absolute temperature	T	Eq. (4)
Bohr magneton	μ_B	Eq. (10)
Boltzmann's constant	k	Eq. (4)
bulk magnetisation	M_0	Eq. (53)
characteristic impedance	Z_0	Eq. (73)
conductivity of loop	σ	Eq. (79)
Curie constant	C	Eq. (9)
electrical resistance	R	Eq. (79)
electron charge	q_e	Eq. (20)
electron mass	m_e	Eq. (20)
electron transition probability	w_e	Eq. (59)
external magnetic field	B_0	Eq. (4)
free-electron g-factor	g_e	Eq. (20)
g-factor	g	Eq. (10)
gyromagnetic ratio	γ	Eq. (4)
heat	Q_h	Eq. (56)
input power	P	Eq. (82)
inside loop radius	r	Eq. (76)
Landé g-factor	g_L	Eq. (34)
Larmor frequency	ω_0	Eq. (2)
length of loop-gap resonator	z	Eq. (76)
longitudinal relaxation time	τ_1	Eq. (3)
loop area	A	Eq. (80)
loop current	I	Eq. (81)
mass	m	Eq. (29)

mean helix diameter	d	Eq. (73)
number of loop gaps	n_g	Eq. (77)
number of turns of helix	N_h	Eq. (74)
nutation magnetic field	B_1	Eq. (60)
permeability of free space	μ_0	Eq. (1)
permittivity of free-space	ϵ_0	Eq. (77)
proton transition probability	w_p	Eq. (2)
quality factor	Q	Eq. (75)
reduced Planck constant	$\hbar$	Eq. (2)
relative permittivity	ϵ_r	Eq. (77)
resonant frequency	f_0	Eq. (73)
resultant spin quantum number	S	Eq. (25)
rf power absorbed	P_{rf}	Eq. (2)
secondary spin quantum number	m_S	Eq. (22)
secondary total angular momentum number	m_J	Eq. (10)
spin energy levels	U	Eq. (22)
spin particle density	N	Eq. (4)
steady-state spin population difference	n_0	Eq. (4)
thermal input-power	P_t	Eq. (67)
thickness of gap	t	Eq. (77)
total linearly polarised nutation field	B_{1t}	Eq. (80)
total loop magnetic flux	ϕ	Eq. (80)
transverse relaxation time	τ_2	Eq. (61)
volumetric magnetic moment	M	Eq. (7)
width of gap	w	Eq. (77)

NOMENCLATURE

AC	alternating current
CAD	computer-aided design
DC	direct current
EM	electromagnetic
EMF	electromotive force
EPR	electron paramagnetic resonance
FBP	filtered back projection
FEM	finite element method
FID	free-induction decay
LGR	loop-gap resonator
MoM	method of moments
MRI	magnetic resonance imaging
NMR	nuclear magnetic resonance
NRMSE	normalised root-mean-square error
PTFE	polytetrafluoroethylene
RF	radiofrequency
SAR	specific absorption rate
SE	spin-echo
VEP	volume equivalence principle
VSWR	voltage standing wave ratio

1 INTRODUCTION

1.1 Background

The various clinical treatments of neoplasms using energy sources such as electromagnetic, ultrasound and radioactivity have been intensively studied over the last 50 years [1]. The side effects of chemotherapy and other chemical cancer treatments are well documented [1]. The use of non-invasive cancer therapy is aimed at reducing the adverse side effects of chemotherapy and highly probable post-surgery complications.

1.1.1 Hyperthermia treatments

The rationale for using hyperthermia ($40 - 44$ °C) in cancer treatment is based on the fact that tumour cells have insufficient blood perfusion [2]. The resulting low pO_2 and low pH environment of the tumour cells increases the cytotoxic effect at elevated temperatures [2]. The three main methods of hyperthermia include [2]:

- Local hyperthermia by external or internal power sources,
- Regional hyperthermia by heated fluid perfusion of organs, limbs or body cavity,
- Whole body hyperthermia.

In local hyperthermia the objective is primarily to increase the tumour temperature. Electromagnetic or ultrasound energy is directed towards the treatment volume [2]. The aim is to increase the tumour temperature as high as possible without compromising the surrounding normal tissue and exceeding temperature tolerance limits [2].

A study of the complications encountered in clinical practice, using a percutaneous internally cooled radio-frequency (RF) ablation technique, showed that RF ablation is a relatively low-risk procedure for the treatment of focal liver tumours [3]. The overall response rates however due to these hyperthermia techniques is only about 13 % [2].

Superparamagnetic iron oxide nanoparticles

An interesting class of magnetic particles called superparamagnetic iron oxide nanoparticles (SPIONs) show promising features as magnetic hyperthermia theragnostic agents (both therapeutic and diagnostic). The particles exhibit unique magnetic properties and remarkable biocompatibility [4].

The conventional approach of SPION hyperthermia is to submit the patient to electromagnetic waves in the order of several hundred MHz [4]. Magnetic fluid or SPION hyperthermia involves spreading magnetic particles across the target tissue followed by applying an alternating current (AC) magnetic field with adequate strength and frequency in order to generate heat by magnetic hysteresis losses and Néel relaxation [4].

Heat dissipation using magnetic particles is a result of the delay in the relaxation of the magnetic moment through either the rotation inside the particle, called Néel relaxation, or from the rotation of the whole particle, called Brownian relaxation, when exposed to an alternating magnetic field with comparatively shorter reversal times [4]. The amount of heat dissipated is given by

$$P = \mu_0 \chi'' f H^2, \tag{1}$$

where P is the thermal power, μ_0 the magnetic permeability of free space, χ'' the imaginary part of the AC magnetic susceptibility and H the AC magnetic field strength [4]. SPIONs as a therapeutic agent however remains a challenge due to the difficulty in particle concentration in the tumour tissue, which results in a relatively low-temperature increase [4].

High-intensity focused ultrasound

High-intensity focused ultrasound (HIFU) relies on the same principles as conventional ultrasound. If the ultrasound beam however is focused and has sufficient energy then it is possible to cause tissue necrosis. The first real evidence that ultrasound could be used therapeutically was introduced in 1942 [5]. Research into HIFU as a tool for neurosurgery continued from the 1950s to 1960s but limitations in technology impeded progress [6]. A typical set-up for lesion production using high intensity focused ultrasound is shown in Figure 1.1.

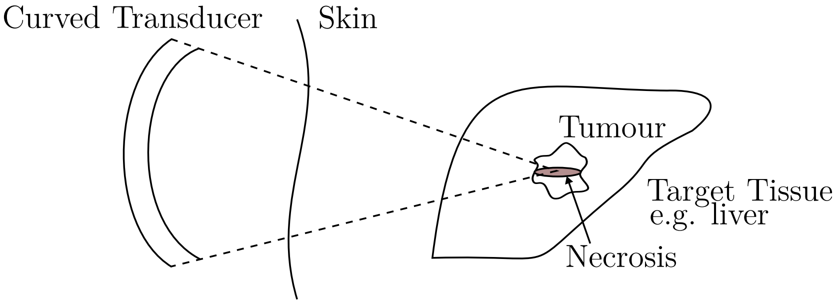

Figure 1.1: Illustration of lesion production using high intensity focused ultrasound.

Ultrasound is a mechanical vibration above that of human hearing (16 kHz), with diagnostic ultrasound typically in the frequency range of $1 - 20$ MHz [6]. The ultrasound energy causes tissue damage through two mechanisms, namely: mechanical-to-heat conversion and cavitation. The former mechanism occurs as the ultrasound propagates through the tissue, and if the rate of heating exceeds the rate of cooling a local temperature rise will occur [6]. The latter mechanism occurs when the ultrasound energy creates bubbles that implode, which generates excessive amounts of heat.

Coagulative necrosis occurs typically above a threshold of 56 °C, which causes cell death [6]. The cooling effect of blood perfusion limits other forms of hyperthermia treatments but is practically eliminated by HIFU, which currently can raise tissue temperatures to 80 °C for exposure times under 3 s [6]. HIFU therefore serves as a benchmark for this research with a temperature rate of $14.3\ {}^{\circ}\mathrm{C} \cdot \mathrm{s}^{-1}$.

Using alternative energy sources to ablate tumours has become popular from these successful hyperthermia technologies such as SPIONs and high-intensity focused ultrasound (HIFU) [6]. It is interesting to note that ultrasound, which has been primarily viewed as a diagnostic technology, can be altered to form a successful therapeutic technology. The idea that a diagnostic technology could be transformed into a therapeutic technology stimulated this research.

1.1.2 Spin-resonance heating

The central idea of this study is to use magnetic resonance imaging (MRI), or spin-resonance, as a therapeutic hyperthermia treatment of neoplasms. The mechanism of using spin resonance to deposit thermal energy into a paramagnetic substance is illustrated in Figure 1.2.

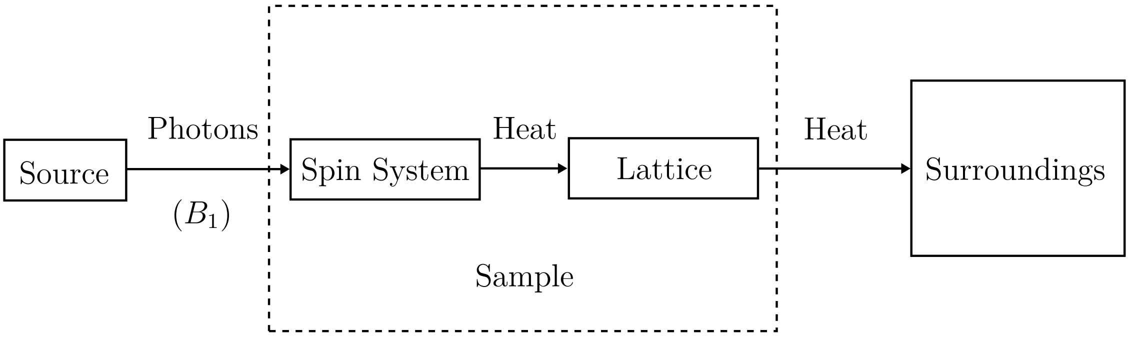

Figure 1.2: Thermal energy deposition using spin-resonance, with the heat capacity of the spin-system being significantly smaller than that of the lattice. Adapted from Weil [7].

A potential benefit of this technology is the increased confinement of heat deposition using spatial frequency selective RF pulses to excite the spin-system. The inherent duality of the technology also allows for thermal image acquisition during treatment which can be used to monitor the heat distribution in the surrounding tissue.

An investigation into MRI localized tissue heating using the spin relaxation of protons in water was performed in 1984 by Parker [8]. The Parker 1984 paper investigates the feasibility of using magnetic resonance of nuclear spin particles as an alternative heating modality. Parker showed using the power density at large (spin-saturated) rf magnetic field strengths, that it would take approximately two years to raise a 1 ml sample of water by one degree Celsius.

A derivation of the equations, as performed by Parker [8], is provided. The net-rate of energy absorption into the nuclear spin-system is given by

$$\begin{aligned} P_{\text{rf}} &= \hbar\omega_0 w_p n, \qquad (2)\\ &= \frac{n_0\hbar\omega_0 w_p}{1+2w_p\tau_1}, \qquad (3)\end{aligned}$$

where P_{rf} is the energy density transfer rate from the spin system into the liquid sample, $\hbar = 1.0546\times10^{-34}$ J · s is the reduced Planck's constant, ω_0 the Larmor frequency, w_p the proton RF stimulated emission and absorption probability, n_0 the steady-state population difference between the two spin-states and $\tau_1 = 0.1$ s the proton spin relaxation time.

The proton transition probability w_p is proportional to square of the RF field. Using the fact that $\hbar\gamma B_0 << kT$, the Boltzmann distribution reduces to

$$n_0 = \frac{N\hbar\gamma B_0}{2kT}, \qquad (4)$$

where the proton density $N = 0.66\times10^{23}$ protons $\cdot$ ml^{-1}, the proton gyromagnetic ratio $\gamma = 2.6752\times10^{8}$ s$^{-1}\cdot$ T^{-1}, $B_0 = 1$ T is the clinical MRI direct current (DC) magnetic field density, $k = 1.38\times10^{-23}$ J $\cdot$ K^{-1} and the body temperature $T = 310$ K. Under spin-saturation i.e. large RF excitation magnetic fields, Equation 3 is reduced to

$$\begin{aligned} P_{\text{rf}} &= \frac{N\gamma^2\hbar^2B_0^2}{4kT\tau_1}, \qquad (5)\\ P_{\text{rf}} &\cong 3\times10^{-9}\,\frac{B_0^2}{\tau_1} \quad \text{J}\cdot\text{s}^{-1}\cdot\text{ml}^{-1}, \qquad (6)\end{aligned}$$

The impractical heating rate using protons necessitates investigation for suitable spins.

1.2 Thesis Structure

The hypothesis, layout and structure of the thesis is as follows:

1.2.1 Hypothesis

It is hypothesised that electron spin-resonance, instead of proton-spin resonance, can be used to deposit a measurable amount of thermal energy into a liquid. The theoretical calculations, simulations and measurements of the temperature rises in paramagnetic gadolinium-based contrast agents due to electron spin-resonance, are the main contributions of this research.

1.2.2 Layout

Chapter 2 covers the review and details of the theories behind magnetism and spin-resonance which are used in this research. The fundamental physics of spin-resonance are covered with important parameters and terms discussed. The magnetic and spin-resonance properties of gadolinium are presented in this chapter, in order to illustrate gadolinium's unique physical properties.

Chapter 3 outlines the application of spin-resonance theory to calculate the predicted temperature rates in gadolinium-based contrast agents. The theory and estimated temperature rates are used as a basis for the design and procedures which are carried out in experimentation.

Chapter 4 describes the simulations and models used to characterise the performance of the various components used in experimentation. The design and simulation results of the DC coil system, resonator and sample-container are covered in this chapter.

Chapter 5 lists the various components that were custom-built and purchased for use in the experiments. The characteristics of the components and their performance is measured and presented in this chapter.

Chapter 6 presents and discusses the experimental results. The statistical and descriptive analysis is discussed in this chapter. The interpretation of the results is covered.

Chapter 7 concludes and summarises the research findings based on the presented theory and experimental procedures. The chapter also suggests future work and improvements to be made in order for the research to become a practical and viable technology.

2 BACKGROUND THEORY

A brief introduction to the physics of magnetism and the different types of magnetic materials is presented. The spin-resonance phenomena of paramagnetic materials with the focus on gadolinium is covered. The relaxation pathway involved with spin-phase decoherence and energy exchange of the spin-lattice system is detailed.

2.1 Magnetism in Matter

When a magnetic substance is placed in an external magnetic field with intensity H, the internal microscopic magnetic moments of the material respond accordingly, with the response given by

$$B = \mu_0 \left(H + M\right), \tag{7}$$

where μ_0 is the magnetic permeability of free space and M is the internal volumetric magnetic moment. The types of magnetic materials are classified according to their susceptibility χ by the following equation

$$M = \chi H. \tag{8}$$

2.1.1 Diamagnetism

Diamagnetic materials are those which have a negative susceptibility and repel the applied magnetic field, with water being a notable diamagnetic material. The other common type of magnetic materials are ferromagnet and ferrimagnet, which require no externally applied field to remain magnetised [4].

2.1.2 Ferromagnetism

Ferromagnetic materials generally have a high magnetic susceptibility and noticeably large residual magnetisation after the removal of the applied field [9]. The microscopic magnetic domains characteristic of ferromagnetic substances like iron are created due to long range ordering of the electron spins. The quantum mechanical interaction is able to order magnetic moments of neighbouring atoms over a large number of atoms [9].

2.1.3 Paramagnetism

Paramagnetic substances become magnetised only when there is an externally applied magnetic field, with χ in the range of $10^{-6} - 10^{-1}$ [9]. In 1895 Curie showed that the magnetic susceptibility, for a certain class of substance, is given by

$$\chi = \frac{C}{T}, \tag{9}$$

where T is the absolute temperature and C is called the Curie constant. Substances which obey this law to a first approximation are termed normal paramagnets. This type of susceptibility however is now recognised only for substances that contain permanent magnetic dipoles, and in fact not all paramagnetic substances obey Curie's law. An example of the types of materials and their temperature dependence is shown in Figure 2.1 [10].

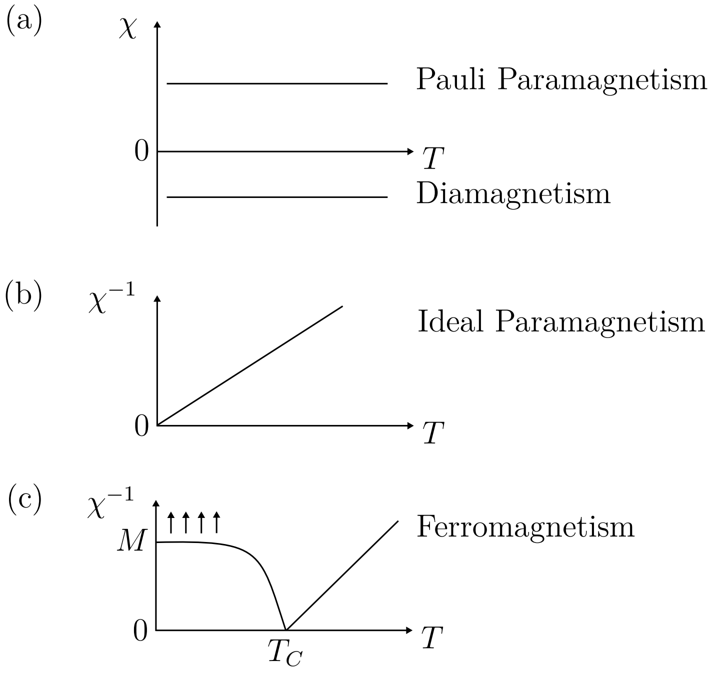

Figure 2.1: Temperature dependence of magnetic susceptibility χ and magnetisation M in different magnetic materials. Adapted from Buschow [10].

The rare earth $4f$ transition ions when placed in solution usually form a close approximation to the ideal paramagnetism [9]. The rare earth ions when in solution are also likely to behave as if they were approximately free, usually termed *quasi-free* ions [9].

Curie's law

A brief derivation of Curie's law is provided in order to illustrate the properties of paramagnetic substances and also to obtain the Curie constant C. The derivation follows that of which is provided by Morrish [9]. The model supposes that there is a volume of gas with N paramagnetic atoms per unit volume, with each atom having a permanent moment μ.

The thermal motion of the atoms ensures that on average the net magnetic moment of the gas is zero. When an external magnetic field is applied the dipoles will tend to align with the field but this alignment will also be opposed by thermal agitation. It is also assumed that no other interaction between the atomic dipoles exists, such that each dipole only responds to the external field.

Using this model together with Boltzmann statistics the net magnetisation per unit volume is calculated. The first case to consider is for wide multiplets compared to kT i.e. $E_{J'} - E_J \gg kT$, which is equivalent to assuming that all of the atoms are in their ground state given by J. According to quantum mechanics the permanent atomic magnetic moments can only have discrete components $m_J \mathrm{g} \mu_B$ in the field direction, where $m_J = J, (J-1), ..., -(J-1), -J$. The potential energy of the dipole in this field is

$$\Delta E = -m_J \mathrm{g} \mu_B B_0, \tag{10}$$

which when substituted into the Boltzmann factor gives $e^{\frac{m_J \mathrm{g} \mu_B B_0}{kT}}$. The net magnetisation is therefore given by

$$M = N \frac{\sum_{-J}^{+J} m_J \mathrm{g} \mu_B e^{\left(\frac{m_J \mathrm{g} \mu_B B_0}{kT}\right)}}{\sum_{-J}^{+J} e^{\left(\frac{m_J \mathrm{g} \mu_B B_0}{kT}\right)}}, \tag{11}$$

The exponential e^x is approximated as $e^x \approx 1 + x$ if $x \ll 1$. Under normal laboratory conditions this is valid since $m_J \mathrm{g} \mu_B B_0 \ll kT$. Equation 11 can therefore be approximated as

$$M \approx N \mathrm{g} \mu_B \frac{\sum_{-J}^{+J} m_J \left(1 + \frac{m_J \mathrm{g} \mu_B B_0}{kT}\right)}{\sum_{-J}^{+J} \left(1 + \frac{m_J \mathrm{g} \mu_B B_0}{kT}\right)}, \tag{12}$$

with the terms of the form $\sum_{-J}^{+J} m_J$ equal to zero, and

$$\sum_{-J}^{+J} 1 = 2J + 1, \tag{13}$$

$$\sum_{-J}^{+J} m_J^2 = \frac{J\left(J+1\right)\left(2J+1\right)}{3}. \tag{14}$$

The result of which is

$$M = \frac{N\mathrm{g}^2 J\left(J+1\right)\mu_B^2 B_0}{3kT}, \tag{15}$$

with the molar susceptibility given by

$$\chi = \frac{N\mathrm{g}^2 J\left(J+1\right)\mu_B^2 \mu_0}{3kT}, \tag{16}$$

and the following expression for the Curie constant

$$C = \frac{N\mathrm{g}^2 J\left(J+1\right)\mu_B^2 \mu_0}{3k}. \tag{17}$$

There is good agreement between theory and experimental results particularly for the rare earth ions both in solution and salt form at room temperature. An example is the gadolinium ion Gd^{3+} which has an effective Bohr magneton number $p_{eff} = 7.94$ [9]. The effective number for the ground state of gadolinium can obtained by substituting $J = \frac{7}{2}$ and $\mathrm{g} = 2$ into the defining equation

$$p_{eff} = \mathrm{g}\left[J\left(J+1\right)\right]^{\frac{1}{2}}, \tag{18}$$

which results in

$$p_{eff} \approx 7.94. \tag{19}$$

The experimental result for gadolinium is $p_{eff} = 8.0$, which shows that there is satisfactory agreement between theory and experiment. In fact, when corrections for the multiplet structure are taken into account the value obtained, by Van Vleck and Frank, is also $p_{eff} = 7.94$ [9].

Super-paramagnetism

In nano-sized (5 – 20 nm) ferromagnetic and ferrimagnetic particles there exists a form of magnetism called super-paramagnetism. A super-paramagnetic substance differs from ferromagnetic and ferrimagnetic materials, as it is able to transition from a paramagnetic state well below the Curie temperature [4]. The particles are much smaller than the single-domain limit; a limit in which the domain walls remain absent [4].

The super-paramagnetic nanoparticles have two main types of relaxation processes, Néel and Brownian relaxation [4]. The Néel relaxation time characterises the magnetisation return time to equilibrium after a perturbation. The Brownian relaxation time characterises the viscous rotation of entire particles [4]. Néel relaxation is preferred as the heat dissipation mechanism as it does not depend on the viscosity of the local environment [4]. The particles also exhibit an optimum relaxation time to achieve a maximum specific absorption rate [4].

2.2 Magnetic Resonance

2.2.1 Paramagnetic resonance

Precession of a magnetic dipole

To achieve a conceptual understanding of resonance and the two relaxation effects in paramagnetic substances, it is useful to consider a system of dipoles in an applied static magnetic field $\mathbf{B_0}$. If a dipole of moment $\boldsymbol{\mu}$ has an intrinsic angular momentum $\boldsymbol{J}$, then the moment will precess about the applied field $\mathbf{B_0}$, as illustrated in Figure 2.2.

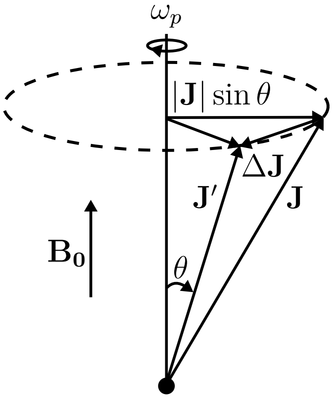

Figure 2.2: Illustration of a dipole moment μ precessing about a static magnetic field B_0.

The magnetic dipole moment is related to the intrinsic angular momentum by

$$\boldsymbol{\mu} = \mathrm{g}_e \frac{q_e}{2m_e}\mathbf{J} = \gamma\mathbf{J}, \tag{20}$$

The precession angular velocity ω_p, which is commonly known as the Larmor frequency, is derived using the torque τ associated with the change in angular momentum, as shown by the following:

$$\begin{aligned} \Delta J &= J\omega_p \Delta t sin\theta, \\ \tau &= \frac{dJ}{dt} = \omega_p J sin\theta, \\ \tau &= \mu B_0 sin\theta, \\ \Rightarrow \omega_p &= \frac{\mu}{J}B_0 = \gamma B_0. \end{aligned} \tag{21}$$

Zeeman energies

The Zeeman energies are the observed spectral line shifts of a particle in an applied external static magnetic field. The energy shifts occur due to the interaction between dipole moment μ of the particle and the applied external magnetic field B_0. The angular momentum, and therefore magnetic moment of an electron, is quantised which leads to a quantisation of energy levels U given by

$$U = \mathrm{g}_e \mu_B m_S B_0, \tag{22}$$

where g_e is the free-electron g-factor, μ_B the Bohr magneton and m_S the secondary spin quantum number. A single unpaired electron has only two m_S values, $+\frac{1}{2}$ and $-\frac{1}{2}$, which results in only two magnetic moment components about the z-axis $\mu_z = \pm \mathrm{g}_e \mu_B$ [7].

Transitions between the Zeeman energy levels can be induced by an alternating magnetic field, usually called the nutation field, B_1 which has the same precession frequency as the magnetic moment. Using the relationship between energy and frequency, the Larmor precession is:

$$\Delta U = \hbar\omega_0 = \mathrm{g}_e \mu_B B_0, \tag{23}$$

$$\omega_0 = \gamma B_0, \tag{24}$$

where γ is the gyromagnetic ratio and ω_0 the Larmor frequency. A selection rule, $|\Delta m_S| = 1$, is also associated with the type of transitions that can occur, even for systems with

$S > \frac{1}{2}$. The selection rule comes from the fact that photons have only one unit of angular momentum and must abide to the conservation of angular momentum [7].

2.2.2 Ferromagnetic resonance

A patent describing the use of ferromagnetic resonance on gadolinium doped yttrium iron garnet (YIG) nanoparticles as intracellular hyperthermia agents is of particular interest [11], as it illustrates the optimization problem between linewidth of the sample and saturation power. That is, the smaller the linewidth the more spatial resolution is obtained at the cost of lower power levels in order to avoid spin population saturation.

The particles described in the patent are about $20 - 50$ nm in size, and exhibit a self regulating phenomena when excited with rf pulsed radiation power. There are many benefits of this technology as shown in the patent by performing a calculation using a YIG nanopowder. The research presented however is focused on the novel use of electron spin resonance in paramagnetic substances and their associated spin heating properties.

2.3 Electron Energy Levels of Gadolinium

Gadolinium has some remarkable properties which make it an applicable substance for hyperthermia treatments. Gadolinium has an exceptionally large magnetic moment and a Curie temperature around 300 K. These magnetic and thermal properties of gadolinium are explained in detail.

2.3.1 Term symbol

A brief explanation on Hund's rules is provided so as to explain the ground state magnetic moment of Gadolinium. Hund arrived at three rules for predicting the magnetic moment of free atoms, or ions, in their ground states [9]. The term symbol, or Russell-Saunders term symbol, is an abbreviated description of the angular momentum quantum numbers for a many electron atom. There exist term symbols for each energy level of an atoms given electron configuration. The generic term symbol is given by

$$^{2S+1}L_J, \tag{25}$$

where S is the total spin quantum number, L is the total orbital angular momentum number and J is the total angular momentum number. The Hund's rules are stated as

1. The term symbol with maximal multiplicity lies lowest in energy,
2. Given a multiplicity, the term with the largest L lies in the lowest energy,
3. For atoms with less (more) than half-filled shells, the lowest (highest) J lies in the lowest energy.

The first rule follows from Pauli's exclusion principle in that when the electrons are close together (opposite spins) they shield each other more effectively from the nucleus which leads to a higher energy state. Thus, when the spins are parallel (higher multiplicity) the electrons will be further apart due to antisymmetry in space which leads to less shielding and a lower, more bound, energy state.

The second rule is permitted by rule 1 and from the basis that for electrons orbiting in the same direction they interact less often than when moving in the opposite direction. The reduced interaction between the electrons moving in the same direction leads to a lower, more bound, energy state.

The third rule is formulated from the spin-orbit coupling, which is that when the spin momentum S and angular momentum L are in opposite direction the interaction energy $\mathbf{L} \cdot \mathbf{S}$ is negative and a minimum.

There exists good agreement between experiment and theory for the rare earth ions, which is mainly due to the insensitivity of the $4f$ shell electrons to the neighbouring atoms caused by the shielding of the outer valence electrons. Gd^{3+} has been shown to follow Curie's law [9].

Using Hund's rules one can find the term symbol for Gadolinium in its ground state

1. $S = 7 \times \frac{1}{2} = \frac{7}{2}$,
2. $L = 3 + 2 + 1 + 0 - 1 - 2 - 3 = 0$
3. $J = L + S = \frac{7}{2}$

Which leads to the following term symbol ${}^{8}S_{\frac{7}{2}}$

Landé formula

The Landé formula for the splitting factor is given by

$$\mathrm{g} = 1 + \frac{J\left(J+1\right) + S\left(S+1\right) - L\left(L+1\right)}{2J\left(J+1\right)}. \tag{26}$$

A derivation is provided in order to help understand Equation 26. The Landé g-factor arises from the geometry of the vectorial magnetic moments and their consequential interaction energies. The magnetic interaction energy between a moment and external field B_0 is

$$\Delta E = -\boldsymbol{\mu} \cdot \mathbf{B_0}. \tag{27}$$

The orbital and spin magnetic moment is given by

$$\boldsymbol{\mu}_{orbital} = -\frac{q_e}{2m}\mathbf{L}, \tag{28}$$

$$\boldsymbol{\mu}_{spin} = -\mathrm{g}_e\frac{q_e}{2m}\mathbf{S}, \tag{29}$$

where the electron spin g-factor has value of approximately 2. The spin magnetic moment is thus approximately twice that of the angular magnetic moment. The interaction energy can therefore be written as

$$\Delta E = \frac{q_e}{2m}(\mathbf{L} + 2\mathbf{S}) \cdot \mathbf{B_0}, \tag{30}$$

The vector model of the angular momentums is shown in Figure 2.3.

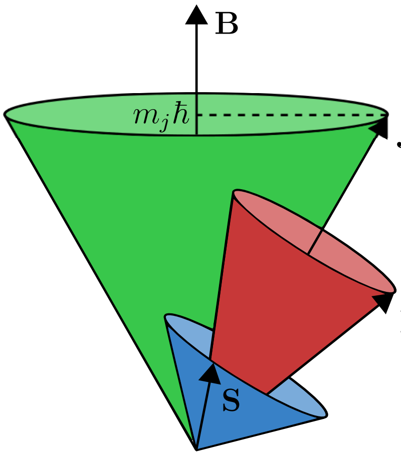

Figure 2.3: Vector model of precessing magnetic moments.

The scalar product in Equation 30 is evaluated by taking the total angular momentum J as the coordinate axis. The spin and angular momentum are projected onto the J axis

$$\Delta E = \frac{q_e}{2m}\frac{(\mathbf{L} + 2\mathbf{S}) \cdot \mathbf{J}}{J} \cdot \frac{\mathbf{J} \cdot \mathbf{B_0}}{J}. \tag{31}$$

Evaluating the dot products in Equation 31 leads to the following expression

$$\Delta E = \frac{q_e}{2m} \frac{\left(L^2 + 2S^2 + 3\mathbf{L} \cdot \mathbf{S}\right) m_J \hbar B_0}{J^2}, \tag{32}$$

Given the law of cosines the remaining dot product in the above equation can be written as

$$3\mathbf{L} \cdot \mathbf{S} = \frac{3}{2} \left(J^2 - L^2 - S^2\right), \tag{33}$$

which when substituted into Equation 32 leads to

$$\Delta E = \frac{q_e}{2m} \frac{\left(3J^2 - L^2 + S^2\right) m_J B_0}{2J^2} = \mathrm{g}_L m_J \mu_B B_0, \tag{34}$$

where μ_B is the Bohr magneton and g_L is the Landé g-factor. The Landé g-factor is simplified to

$$\mathrm{g}_L = 1 + \frac{J\left(J+1\right) + S\left(S+1\right) - L\left(L+1\right)}{2J\left(J+1\right)}. \tag{35}$$

Using the term symbol for gadolinium with the above equation, the Landé g-factor is 2.

2.3.2 Zero-field splitting

Paramagnetic ions are by no means isolated, they are surrounded by an agglomeration of diamagnetic ions, with distances of order 0.2 – 0.3 nm [12]. The charged 'ligand' ions produce a strong electrostatic field ('ligand' field), which interacts with the paramagnetic ions. The interaction may exceed the spin-orbit interaction in some circumstances. The problem of modelling this field is complex and is usually regarded in the 'crystal field' approach as an additional electrostatic potential which reflects the symmetry of the ions and their surroundings [12]. The result of this field is to split the levels, which leaves the groups with relatively small degeneracy.

Gadolinium zero-field splitting

The crystalline field effect on paramagnetic ions in solution is an important phenomena which can lead to splitting of the degenerate energy levels. The inhomogeneous electric fields are created by the diamagnetic neighbours of the paramagnetic ions. At the more ordinary temperatures however the effect on the rare earth ions is so small as to be assumed negligible in most cases [9]. Gadolinium has a $4f$ orbital filled with seven electrons which are well shielded by the outer electrons. The $4f$ electrons also have a small average radius which tends to reduce the crystalline field effect. The effect of the crystalline field on the splitting of the degenerate levels therefore remains negligible.

2.4 Spin Relaxation

Many experiments have been performed on paramagnetic ions belonging to the $3d$ group and Gd of the $4f$ group. These ions have magnetic dipole moments which are only a result of the electron spin [9]. There are two different time related effects involved in electron spin relaxation. The one type of relaxation involves the interaction between the spins in the *spin system*, and the other type involves the interaction between the spins and the vibrations of the surrounding medium, commonly termed the *lattice*.

The difference between the spin system and the lattice temperature depends on the thermal contact between the two systems, and ultimately depends on the spin-lattice interaction [9]. The spin system interacts with the lattice via thermal vibrations, which are called Debye waves or *phonons*.

2.4.1 Spin-spin relaxation

The measure of interaction between spins is termed the spin-spin relaxation time τ_2 [7]. An example is $\tau_2 = \infty$ which implies the spins are completely isolated from one another, a rare case to encounter in practice. The opposite case is $\tau_2 = 0$ which implies a strong connection between the spins and as a result no local variation in spin temperature [7]. The latter case is also not encountered often as it has to do with strongly coupled systems such as ferromagnetic or anti-ferromagnetic systems [7].

The spins can interact via magnetic dipolar coupling which will not cause an overall energy change in the system as a result of mutual spin flips. The mutual spin flips do however affect the lifetime τ_1 of each spin [7]. The movement or propagation of the flips through the lattice is termed spin diffusion, which results in equilibration of the spin temperature throughout the spin system [7]. The spin-spin relaxation time is therefore a measure of this equilibration rate.

2.4.2 Spin-lattice relaxation

The mechanisms by which energy is exchanged between the paramagnetic ions (spin system) with the electromagnetic thermal reservoir and the phonon radiation bath (lattice vibrations) are explained. A simplified diagram of the energy flow as shown in Figure 1.2, adapted from Weil [7], is repeated in Figure 2.4 for clarity.

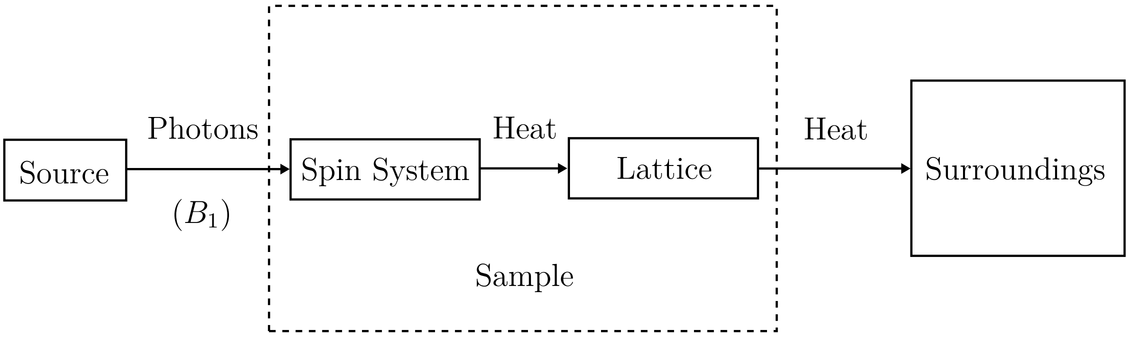

Figure 2.4: Energy flow during a magnetic resonance experiment with the absorbed spin energy lost as heat to the lattice at an exponential rate. Adapted from Weil [7].

The first reservoir to consider is that of the electromagnetic thermal reservoir. The rate at which thermal energy is exchanged between the two systems depends on their thermal capacitances. The following derivation of the spin-lattice relaxation time τ_1 follows that given by Abragam [12].

The initial step is to assume that the thermal capacitance of the surrounding system is much larger than that of the spin system. The spin system is assumed to be in thermal equilibrium with the surroundings which are at a definite temperature T_0.

An atomic system exchanges energy through transitions between two levels, assuming there are only two levels ($S = \frac{1}{2}$), the energy difference is written as

$$\Delta E = E_2 - E_1 = \hbar\omega, \tag{36}$$

The electron can exist in a degenerate state which is lifted once an external field is applied. Let the number of atoms in the lower and upper energy eigenstates at any given instant be denoted by n_1 and n_2 respectively. The lower and upper level states will transition at a rate proportional to their respective numbers, as shown

$$-\frac{dn_1}{dt} = \frac{dn_2}{dt}, \tag{37}$$

$$= w_{\uparrow}n_1 - w_{\downarrow}n_2, \tag{38}$$

where $w_{\uparrow}$ and $w_{\downarrow}$ are the rate constants at which the lower and upper states transition respectively. At thermal equilibrium the populations will be at their steady-state values N_1 and N_2, which is illustrated by

$$0 = w_{\uparrow} N_1 - w_{\downarrow} N_2, \tag{39}$$

and simplified to

$$\frac{N_1}{N_2} = \frac{w_{\downarrow}}{w_{\uparrow}}, \tag{40}$$

with the transition rate constants given by the Einstein coefficients [7],

$$\begin{align} w_{\uparrow} &= B\rho_{em}, \tag{41} \\ w_{\downarrow} &= A + B\rho_{em} = B\rho_{em} e^{\frac{\hbar\omega}{kT_0}}, \tag{42} \end{align}$$

where ρ_{em} is the radiation density, A the coefficient of spontaneous emission and B the coefficient of stimulated absorption and emission. The transition rates are substituted into Equation 40 to give the Boltzmann population ratio

$$\frac{N_1}{N_2} = \frac{(A + B\rho_{em})}{B\rho_{em}} = e^{\frac{\hbar\omega}{kT_0}}. \tag{43}$$

The situation when the spin system is not in equilibrium with the radiation bath can be analysed by using Equation 38

$$\begin{align} \frac{d\left(n_1 - n_2\right)}{dt} &= -2\left(w_{\uparrow} n_1 - w_{\downarrow} n_2\right), \tag{44} \\ &= \left(w_{\downarrow} + w_{\uparrow}\right) \{(N_1 - N_2) - (n_1 - n_2)\}, \tag{45} \end{align}$$

which comes from the fact that $n_1 + n_2 = N_1 + N_2 = N$ and by using Equation 40. The solution of Equation 45 is

$$(n_1 - n_2) = (N_1 - N_2) + \{(n_1 - n_2)_0 - (N_1 - N_2)\} e^{-\frac{t}{\tau_1}}, \tag{46}$$

where $(n_1 - n_2)_0$ is the population difference at $t = 0$, and τ_1 is given by

$$\frac{1}{\tau_1} = \left(w_{\downarrow} + w_{\uparrow}\right), \tag{47}$$

expanding the above equation leads to

$$\frac{1}{\tau_1} = A + 2B\rho_{em} = B\rho_{em}\left(e^{\frac{\hbar\omega}{kT_0}} + 1\right). \tag{48}$$

Substituting the electromagnetic radiation density ρ_{em} with the Planck's black body radiation formula

$$\rho_{em} d\omega = \frac{\hbar\omega^3}{\pi^2 c^3} \frac{d\omega}{\left(e^{\frac{\hbar\omega}{kT_0}} - 1\right)}, \tag{49}$$

leads to the well known expression for A and B

$$\frac{1}{\tau_1} = \frac{\hbar\omega^3}{\pi^2 c^3} B \coth\left(\frac{\hbar\omega}{2kT_0}\right) = A \coth\left(\frac{\hbar\omega}{2kT_0}\right). \tag{50}$$

An example is calculated for when $\omega = 2\pi \times 800 \times 10^6$ rad $\cdot$ s^{-1}, and substituted in Equation 50 results in the ratio A/B of order 10^{-32}. The result illustrates that the spontaneous emission of radiation is highly unlikely and is dominated by that of stimulated emission. If $\hbar\omega \ll kT_0$ then Equation 47 can be written as $\tau_1^{-1} = 2w$. It is also noted for this range and given that the coefficient B is not temperature dependent that τ_1^{-1} varies linearly against T_0.

The second reservoir is considered using the derivation of the spin-lattice relaxation time τ_1 for a two level spin system ($S = \frac{1}{2}$), as provided by Weil [7]. It is shown that for this two level system that the relaxation time is expressed as

$$\frac{1}{\tau_1} = (A_{ul} + 2B_{ul}\rho_\nu + w_\downarrow + w_\uparrow), \tag{51}$$

where A_{ul} is the Einstein coefficient for spontaneous photon emission, B_{ul} is the Einstein coefficient for stimulated emission, $w_\downarrow$ and $w_\uparrow$ are the upper and lower transition probability rates induced by the lattice respectively. Generally under normal laboratory conditions, i.e. no power saturation, the transition probability terms w dominate in Eq. (51).

The relaxation of the spin-system occurs primarily through electron-spin flips induced by dynamic interactions with the surrounding environment, known as the 'lattice' [7]. The approach of τ_1 to zero implies an instantaneous energy exchange between the electromagnetic reservoir and the lattice via the spin system.

Considering a two level system with energy levels $\hbar\omega = \mathrm{g}\gamma B_0$, the bulk magnetisation M is written as

$$M = \frac{1}{2}\mathrm{g}\gamma\left(n_1 - n_2\right), \tag{52}$$

$$M_0 = \frac{1}{2}\mathrm{g}\gamma\left(N_1 - N_2\right), \tag{53}$$

which when substituted into Equation 45 leads to

$$\frac{dM}{dt} = \frac{1}{\tau_1}\left(M_0 - M\right). \tag{54}$$

The spin-lattice time τ_1 also therefore describes the interval it takes the magnetisation to return to its thermal equilibrium value. A different equation for τ_1 is obtained using a classical thermodynamics approach, as performed by Abragam [12], which solves for τ_1 in terms of the specific heat C_B of the spin system at a constant field B.

Using the assumption in this approach, which is that the rate of energy transfer between the two systems is proportional to their temperature difference with constant α, one obtains the following result

$$\tau_1 = \frac{C_B}{\alpha}. \tag{55}$$

The equation shows that if the specific heat capacity C_B is small and there is good thermal contact between the systems, $\alpha \gg 1$, the result is that τ_1 will be small with the system having a relatively fast spin-relaxation process.

A spin temperature can also be defined for a many level spin system provided that the population ratio is given by the usual Boltzmann relationship $e^{\frac{\hbar\omega}{kT_s}}$, the condition of which is met if the spin system is internally equilibrated. The spin-spin interaction achieves this equilibrium state provided it is fast enough i.e. $\tau_2 \ll \tau_1$.

There are generally three common types of spin-lattice relaxation mechanisms, namely the *direct*, the *Raman* and the *Orbach* processes, shown in Figure 2.5. In the direct process the electron spin is flipped by the absorption or emission of a single phonon with the same Larmor frequency.

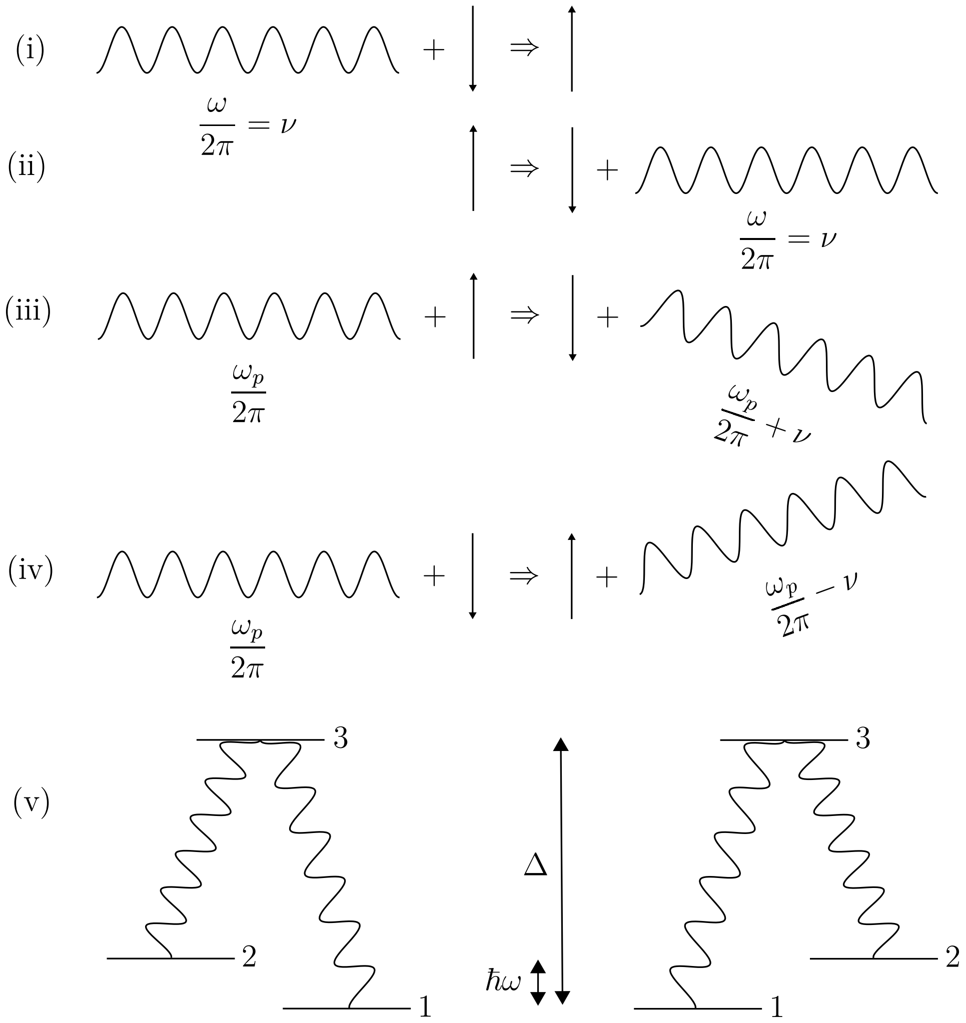

Figure 2.5: Schematic illustration of the three spin-phonon relaxation processes, where (i-ii) direct process, (iii-iv) Raman process and (v) Orbach process. (i-ii) A phonon with frequency ν is absorbed and emitted by spin system respectively. (iii-iv) A phonon with frequency $\frac{\omega_p}{2\pi} \pm \nu$ is scattered by the spin system respectively. (v) Phonons with frequencies corresponding to Δ, $\Delta - h\nu$ energies are absorbed or emitted by direct processes which cause transitions $1 \longleftrightarrow 3$ and $2 \longleftrightarrow 3$ respectively. Adapted from Abragam [12].

The Raman process involves the absorption of one phonon followed later by an emitted phonon, the difference in energy of the phonons being equal to the energy of the spin transition. The Orbach process also consists of two phonons, however the absorbed phonon has enough energy to lift the spin to a much higher electronic level such that the emitted phonon energy corresponds to the difference between the spin and the ground state [12].

3 CONTRIBUTING THEORY

The theory describing how electron spin resonance and the spin-lattice relaxation mechanism can be used to deposit thermal energy into a contrast agent is presented. The contrast agent used in the calculations is Dotarem, with a brief section describing how the chemical properties of the substance contribute to spin-lattice thermal energy deposition. The temperature rates for relatively small and large magnetic RF excitation fields are calculated.

3.1 Electron Spin Resonance Hyperthermia

Focusing energy in order to locally heat damaged or diseased tissue is typically performed using magnetic fluids, radiofrequency, ultrasound and nanoparticles [13–15]. High intensity radiofrequency or ultrasound energy is focused using curved transmitters or phased arrays [16–18]. In magnetic resonance the focusing could be achieved using linear magnetic gradients (commonly known as gradient coils) or by focusing the DC external magnetic field. The first question however is can a substance under magnetic resonance conditions achieve a measurable rise in temperature.

The thermal losses and sensitivity of MRI have been well documented with the effects modelled with high precision [19]. The research field of magnetic resonance imaging has therefore been focusing mainly on the spectroscopy aspects of the technology. The only published theoretical investigation into whether or not magnetic resonance of protons can induce thermal rise in a sample was demonstrated by Parker [8].

As explained by Parker the rate of heat absorption depends on two separate interaction rates, namely the interaction rate of the rf with the local magnetic moments, and the rate at which the magnetic moments exchange thermal energy with their surrounding environment.

Parker derived and showed that the proton thermal energy transfer rate for 1 g of water in tissue is

$$\frac{dQ_h}{dt} \approx 3 \times 10^{-9} \frac{B_0^2}{\tau_1}, \tag{56}$$

and using clinical nuclear magnetic resonance (NMR) parameters $\tau_1 = 0.1$ s, $B_0 = 1$ T, with a heat capacity for water 4.2 $\mathrm{J} \cdot \mathrm{g}^{-1} \cdot \mathrm{K}^{-1}$, results in

$$\frac{dT}{dt} \approx 0.7 \times 10^{-8}\ \mathrm{K} \cdot \mathrm{s}^{-1}, \tag{57}$$

which approximates to under 1 °C every two years. The resultant temperature rise is clearly not practical even when B_0 is increased by an order of magnitude. Also, as B_0 increases the rf frequency increases, due to the Larmor precession relationship, which results in surface heating due to conventional rf absorption [8]. Recently however large fields of 7 T, at frequencies as high as 300 MHz, have been used for imaging with no noticeable heating due to the rf surface absorption [20].

The Italian National Research Council and their institute for Applied Physics compiled an online database for the electromagnetic properties of body tissues from 10 Hz to 10 GHz [21]. The electromagnetic skin depth of fat tissue is halved in the frequency range from 46 MHz (commonly used in MRI) to 800 MHz. The loss tangent of blood and fat tissue interestingly decreases by an order of magnitude for the same range of increasing frequencies.

A natural question arises as to whether or not a different spin resonant particle could be used, such as an electron, which has a larger magnetic moment and a significantly smaller τ_1 relaxation time compared to that of a proton. The electron has a magnetic moment which is approximately one thousand times larger than that of a proton, with a spin-lattice relaxation time, in certain compounds and conditions, approximately a billion times smaller [9, 22, 23].

The electron has a gyromagnetic ratio γ which is three orders of magnitude larger than that of a proton. The difference in magnitude is a result of the mass of the particles [29]. The electron being much less massive than a proton results in a much larger gyromagnetic ratio, and hence a larger magnetic dipole moment. There are also a greater number of electrons, at an arbitrary external magnetic field strength B_0, in a lower energy state compared to that of protons [12], as shown for the steady-state population ratio given by

$$\frac{N_1}{N_2} = e^{\frac{\hbar \gamma B_0}{k T_0}}. \tag{58}$$

3.1.1 Electron spin-lattice relaxation time

The mechanism whereby the nuclear spins obtain thermal equilibrium with the surrounding bulk material, known as the lattice, is called *spin-lattice relaxation.* A spin system is said to be “informed” of the temperature of the lattice [24]. A steady-state description of a spin resonance experiment can be thought of as two competing processes, one process being the establishment of Boltzmann distribution and the other process the disruption of the spin populations caused by the driving electromagnetic field [25].

At thermal equilibrium there are more particles in a spin-down configuration than a spin-up configuration, and given that the probability to transition from each state is the same, it results in a net absorption of energy. Eventually, as the rf power continues to increase the spin system will *saturate* resulting in no further energy absorption. Electrons however, having a much smaller spin-relaxation time, allow for more rf power to be applied before saturation is reached.

The other advantage of using electrons is that they are significantly smaller, in fact they are considered point particles, which allows for $\tau_2 \approx \tau_1$, and results in the energy absorbed by the electron spin system to be immediately distributed and deposited into the lattice [26].

3.1.2 Characteristics of Dotarem®

The DOTA ligand has unique properties compared to other ligands such as DTPA, which is used in Magnevist. The symmetry and rigidity of the DOTA ligand results in a six-times longer electronic τ_1 time, commonly expressed as τ_{1e}, compared to other linear structured contrast agents [27]. The longer relaxation time, as shown by the calculations in this section, increases the effect under investigation. ProHance is a contrast agent which has a similar structure, and therefore electron spin properties, to that of Dotarem [28].

3.1.3 Continuous-wave excitation

The concern about whether pulsed or continuous irradiation of the sample should be used is addressed by a paragraph from John A. Weil’s book on electron paramagnetic resonance [7]:

> “Note that with B_1 turned off, the photon density ρ_ν is essentially zero, so that no induced transitions take place. However, the spontaneous photon emission is enhanced when the spin magnetic moments are in phase (super-radiant system), that is, while FID is appreciable. [In cw EPR, the spins are not correlated. Hence most of the energy is lost from the spins goes to the ‘lattice’ of atoms and only some (usually a negligible amount) goes back to B_1 (via incoherent spontaneous emission).]”

3.1.4 RF power absorbed by a spin-system

The rf power P_{rf} absorbed by a spin-system is derived by Slichter [29], which is

$$P_{\mathrm{rf}} = n_0 \hbar \omega \frac{w_e}{1 + 2 w_e \tau_{1e}}, \tag{59}$$

where w_e is the induced electronic transition probability and is defined as a function of frequency given by

$$w_e(\omega_0) = \frac{\pi}{2} \gamma^2 B_1^2 (S + m_S)(S - m_S + 1) g(\omega_0), \tag{60}$$

The secondary spin quantum number m_S ranges from $-S$ to S in unit intervals with $g(\omega_0)$ representing the Lorentzian line-shape function normalised to unit area [29]. At the resonant angular frequency ω_0 the lineshape function is

$$g(\omega_0) = \frac{\tau_{2e}}{\pi}. \tag{61}$$

The parameter τ_{2e} is the spin-spin relaxation time constant and represents the lifetime of the phase coherence among the spins. Given that the macroscopic electronic transition probability equation is applicable to substances where all the transitions occur at the same frequency [12], the states can be summed over all transitions using the following relation

$$\sum_{-(S-1)}^{S} (S + m_S)(S - m_S + 1) = \frac{2}{3} S(S+1)(2S+1), \tag{62}$$

$$w_e(\omega_0) = \frac{1}{3} \gamma^2 B_1^2 S(S+1)(2S+1)\tau_{2e}. \tag{63}$$

The steady-state population difference n_0 between two spin-states, m_S and $m_S + 1$, is given by

$$n_0 = \frac{2NS(S+1)\hbar\gamma B_0}{3kT}. \tag{64}$$

Substituting Equations 63 - 64 into Equation 59 results in the rf power absorbed by the spin-system per unit volume as

$$P_{\mathrm{rf}} = \frac{2N\gamma^2\hbar^2 S(S+1) B_0^2 w_e}{3kT(1 + 2w_e\tau_{1e})}. \tag{65}$$

The parameter values for the variables described in Equation 65 are shown in Table 3.1.

Table 3.1: List of parameters used to calculate rf power and temperature rise, with the electronic spin relaxation times τ_{1e} and τ_{2e} obtained from Rast and Atsarkin [22, 23].

Parameter	**Value**	**Units**
γ	1.7608592×10^{11}	$\mathrm{rad \cdot s^{-1} \cdot T^{-1}}$
N	3.011×10^{20}	number of Gd atoms per ml
$\hbar$	$1.0545717 \times 10^{-34}$	$\mathrm{J \cdot s \cdot rad^{-1}}$
S	7/2	resultant spin angular momentum
m_S	1/2	secondary spin quantum number
B_0	30.6	mT
k	$1.3806503 \times 10^{-23}$	$\mathrm{J \cdot K^{-1}}$
T	310.15	K
$\tau_{1e,2e}$	0.1	ns
B_1	1.5	mT
$w_e(\omega_0)$	2.93×10^{8}	$\mathrm{s^{-1}}$

The number of spins and relaxation time values are estimated for the Dotarem® solution, which has a concentration of 0.5 $\mathrm{mmol \cdot ml^{-1}}$ and a density of $\rho_v = 1.1753\ \mathrm{g \cdot ml^{-1}}$. Solving Equation 65 using the parameter values in Table 3.1 with the unit volume in ml, yields

$$P_{\mathrm{rf}} = 65.99\ \mathrm{W \cdot ml^{-1}}.$$

Under adiabatic conditions the thermal input-power P_t is equated to the rf spin-power P_{rf}, with the temperature temporal gradient $\frac{dT}{dt}$ related by the following

$$\Delta Q_h = mC\Delta T, \tag{66}$$

$$\frac{dT}{dt} = \frac{P_t}{\rho_v C}. \tag{67}$$

Assuming the heat capacity of water $C = 4.18\ \mathrm{J \cdot g^{-1} \cdot K^{-1}}$ for the Dotarem solution, and substituting the value into Equation 67, results in a temperature rate of

$$\frac{dT}{dt} = 13.43\ {}^{\circ}\mathrm{C \cdot s^{-1}}.$$

The electron spin-relaxation time τ_{1e} is a critical parameter in the spin-thermal system as it effectively determines the efficiency at which the absorbed rf energy is converted into thermal energy within the lattice. The statement that $\tau_{1e} \approx \tau_{2e}$, which is only true for frequencies below 5 GHz, is validated by Atsarkin et al. [23]. The article shows that for DOTA type aqueous complexes τ_{1e} varies between 0.1 ns and 1 ns for 100 MHz − 10 GHz. As a result of this range and the selected lower frequency a conservative value of τ_{1e} is used in Equation 65.

A maximum temperature rate can be obtained using the same parameters in Table 3.1, as demonstrated in Figure 3.1.

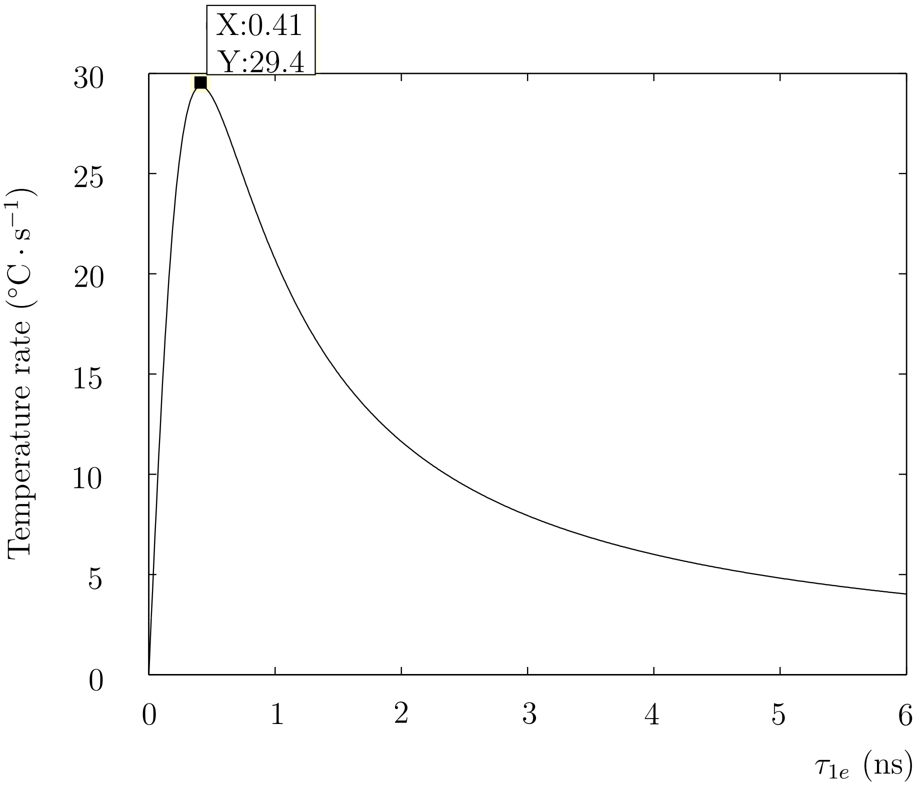

Figure 3.1: The temperature gradient of DOTA complex as a function of the spin-lattice relaxation time τ_{1e}.

The maximum temperature rate is significant for tumour ablation as it is comparable to current non-invasive methods, such as HIFU, which can provide up to 14.3 °C · s^{-1} [6]. The τ_{1e} relaxation time at which this maximum occurs however is nearly an order of magnitude higher than the τ_{1e} time of current contrast agents. The contrast agents will therefore most likely need to be redesigned in order to achieve this optimal temperature rate.

3.1.5 RF power absorbed by a saturated spin-system

The rf power P_{rf} absorbed by a spin-system, in a different form compared to Equation 59, as derived by Abragam [24], is given by

$$P_{\mathrm{rf}} = \frac{\omega_0 \gamma B_1^2 \tau_2 M_0}{1 + (\tau_2 \Delta\omega)^2 + \gamma^2 B_1^2 \tau_{1e} \tau_{2e}}, \tag{68}$$

which for a saturated spin-system, i.e. $\gamma^2 B_1^2 \tau_{1e} \tau_{2e} \gg 1$ ($B_1 \approx 1$ T), is reduced to:

$$P_{\mathrm{rf,sat}} = \frac{B_0 M_0}{\tau_{1e}}. \tag{69}$$

The bulk magnetisation M_0 for a spin, integer or half integer S, system is given by

$$M_0 = \frac{N \gamma^2 \hbar^2 S\left(S+1\right) B_0}{3kT}. \tag{70}$$

The power absorbed by the saturated spin-system is therefore

$$P_{\mathrm{rf,sat}} = \frac{N \gamma^2 \hbar^2 S\left(S+1\right) B_0^2}{3kT\tau_{1e}}. \tag{71}$$

Using the same parameters shown in Table 3.1, but with B_1 substantially increased in order to achieve saturation and solving Equation 71, yields

$$P_{\mathrm{rf,sat}} = 1192 \text{ W}.$$

Once again assuming that the specific heat of the solution is similar to that of water i.e. $C = 4.18 \text{ J} \cdot \text{g}^{-1} \cdot \text{K}^{-1}$, and substituting the value into Equation 67, results in a temperature temporal gradient of

$$\frac{dT}{dt} = 242.6 \text{ °C} \cdot \text{s}^{-1}.$$

Under these saturation conditions the result is significantly more effective compared to current non-invasive ablation techniques. However, the SAR = 185 GW when using the specific absorption rate (SAR) derived in section 5.3.2 with the dimensions of the test capsule and parameters in Table 3.1, for a $B_1 = 1$ T. Further, to achieve such a large B_1 value *in situ* is also a difficult, if not an impossible, task.

3.2 Aims of Research

The above contributing theory suggests that if the electron spin-system is excited under the specified conditions that a resulting temperature rise of at least $13.43\ ^{\circ}\mathrm{C} \cdot \mathrm{s}^{-1}$ would result.

The theory also suggests that for small spin-lattice relaxation times, $\tau_{1e} < 1$ ns, that the resulting temperature rate is small and should be approximately linear against time. The linear relationship is tested and compared to experimental results for further validation of the theory presented.

It is therefore hypothesised, and tested using appropriate thermometry, that electron spin-resonance in a clinical contrast agent can be used to deposit a measurable amount of thermal energy in the substance.

The presented theory, calculations and measurements of the temperature rises in paramagnetic gadolinium-based contrast agents, due to electron spin-resonance, are the aims and contributions of this research.

Subsidiary aims

The research requires the design and measurement of the external electromagnetic configuration. The investigation into whether these fields can be obtained practically is performed. Specifically the magnitude and homogeneity of the DC magnetic field is simulated and tested, as well as the simulation and indirect measurement of the rf field magnitude using the observed temperature change of the tested substances.

4 COMPUTATIONAL SIMULATIONS

The experimental components used in the research are presented. The various designs and selected parameters are detailed. Electromagnetic and thermal models of the sample and fibre optic thermometer are compared to experimental data for parameter adjustment and verification.

4.1 Outline of Experimental Design

The experiment will require the following three major components: external DC magnetic field, rf excitation and contrast agent. The DC magnetic field is the stationary field which determines the frequency at which the electrons resonate. The rf source emits an orthogonal magnetic field, relative to the stationary field, oscillating at the Larmor frequency. The rf field deposits energy into the contrast agent medium through the spin-resonance relaxation effect. The thermal measurement of the contrast medium is recorded using an appropriate thermometry technique.

4.2 DC Magnetic Field Coil System

The electrons in the spin sample have a resonance according to Larmor's precession theory, which simply states

$$\omega_0 = \gamma B_0, \tag{72}$$

that is to say the electron will precess at a frequency that is directly proportional to the local DC magnetic field strength. The reality however is that on an atomic scale the electron is not isolated and is in the presence of other spin particles such as electrons and nucleons, resulting in a local magnetic field strength which changes from point-to-point. The distribution of resonant frequencies is thus not homogeneous over the sample space. The inhomogeneities of the external DC magnetic field can also contribute to this frequency distribution or what is commonly known as spectrum broadening.

It is therefore advantageous to minimise the inhomogeneity of the external DC magnetic field as this will help narrow the spectrum and thus allow for the spin sample to resonate at a single frequency and effectively absorb more power. The strength of the DC magnetic field is required to be around 30 mT, which means that a relatively large current will circulate in the coils. The DC coil system and its specifications are unique with no company available to supply such a custom apparatus. It was therefore decided that the coil system be built and tested in-house using the Genmin laboratories at the University of Witwatersrand.

The design requirement of the coil system is to produce a magnetic field that is practically homogeneous in a reasonable volume of approximately $15 \times 8 \times 8$ cm^3. The magnetic flux density required in this volume should be at least 30 mT, which is equivalent to an H-field of 24.7 kA $\cdot$ m^{-1}. Various designs were considered including a spherical 4-coil, 6-coil and 8-coil system [30, 31], as well as a bi-planar 4-coil and 6-coil system [32, 33]. The final, most effective, design was chosen to consist of eight circular coils placed horizontally with a common axis so that they circumscribed a sphere as shown in Figure 4.1.

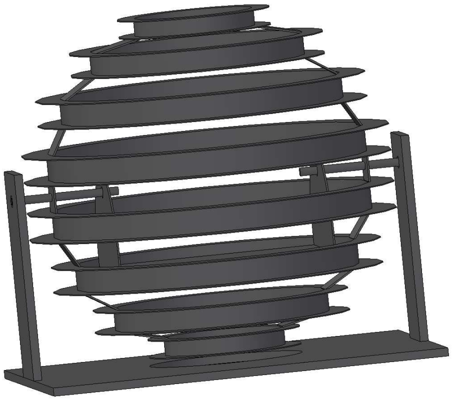

Figure 4.1: Spherical layout of coil-formers used to generate a homogeneous static magnetic field.

The chosen design has a superior magnetic field homogeneity compared to the other designs, as well as a comparatively larger region of homogeneity [30]. The details of the coils are shown in Table 4.1 with a mechanical drawing shown in Figure 4.2. The number of turns used for each coil is such that the turns ratio is close to the optimal values outlined by Pittman and Waidelich [30].

Table 4.1: DC coil specifications and dimensions.

Coil	**Number of Turns**	**Radius (cm)**	**Vertical Position (cm)**
1	268	20.81	±3.49
2	239	18.53	±10.08
3	184	14.22	±15.59
4	109	8.29	±19.40

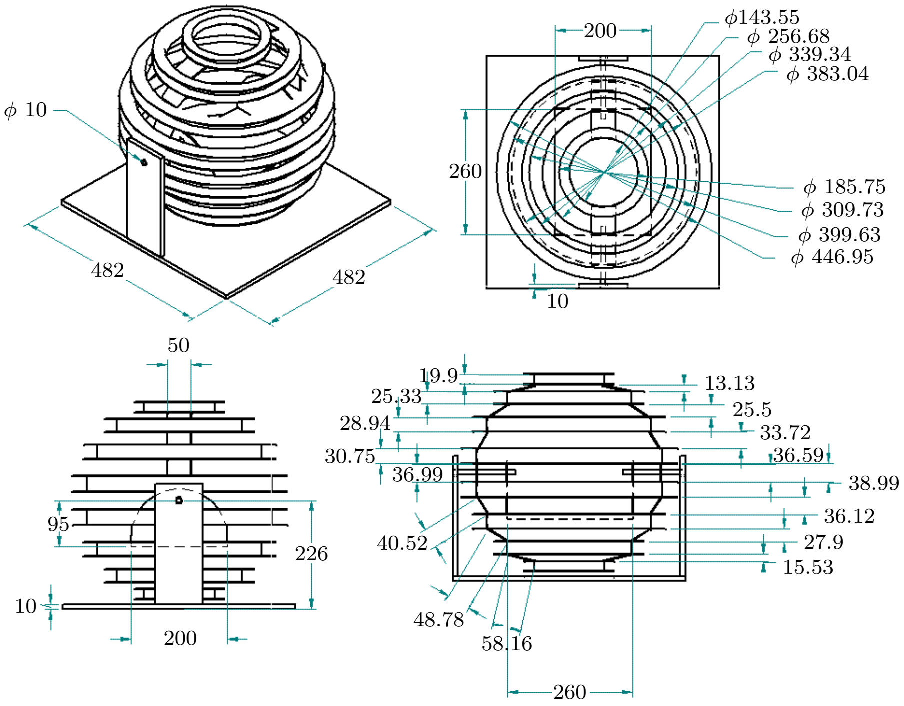

Figure 4.2: Isometric, top, front and side view of the DC coil system (units in mm).

The homogeneity of the DC magnetic coil, which is simulated at 0.032196 %, in a spherical volume with radius 10 cm, is shown in Figure 4.3. It is assumed that since the sample-container size is smaller by approximately 0.0061 % than the simulated spherical volume, that the homogeneity will be sufficient to achieve a desired effect.

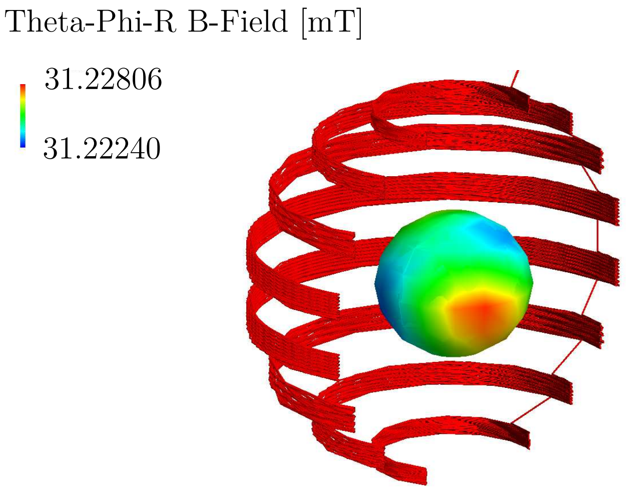

Figure 4.3: Simulation intensity map illustrating the homogeneity of the 31 mT magnetic field in a diameter of 160 mm.

The homogeneity of the magnetic field represented as a line-graph is shown in Figure 4.4.

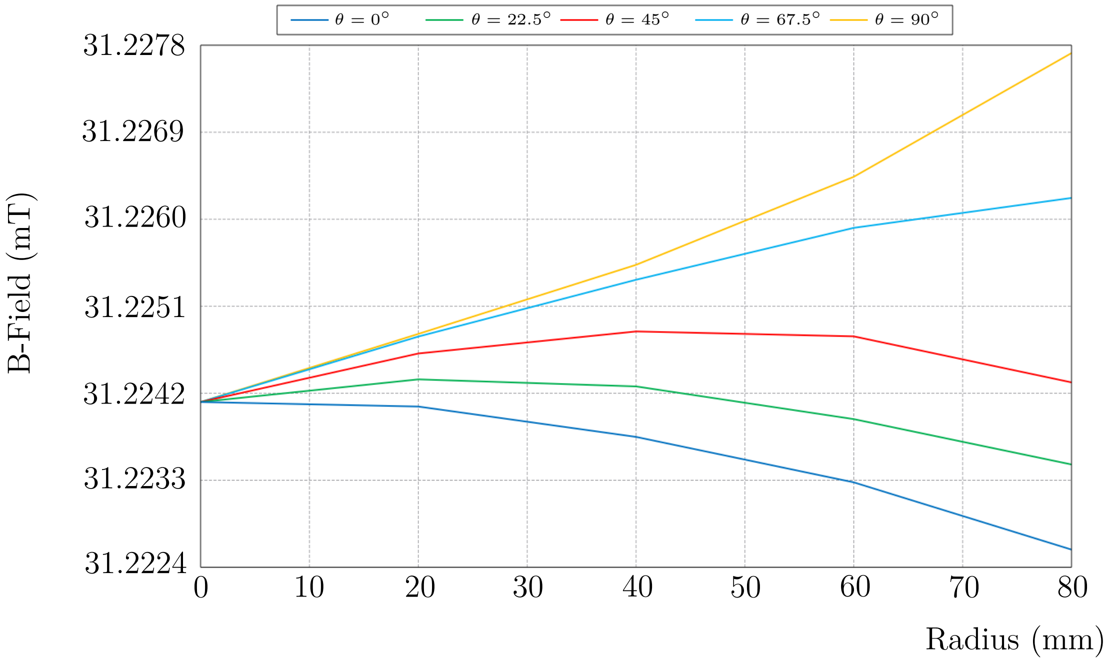

Figure 4.4: Cartesian plot of the magnetic flux density within a 80 mm radius at 22.5° azimuthal increments.

4.3 RF Resonators

The constant rf excitation field B_1, with a bandwidth in the order kHz compared to the spin-system linewidth of MHz, is generated using a resonant cavity in which the sample is situated. The homogeneity and magnitude of the magnetic field relative to the electric field are of key importance. A initial design is presented with the final selected resonator analysed and simulated.

4.3.1 Helical coil resonator

The constraints imposed by the physical dimensions of the test sample in order to obtain a high DC magnetic field homogeneity, and the selected operational frequency of the system, leads to a necessary design which uses a small rf cavity as opposed to using discrete self-resonant components.

The first real design considered, in order to achieve the large magnetic field strengths, was that of the helical resonator. The helical resonator is shown in Figure 4.5.

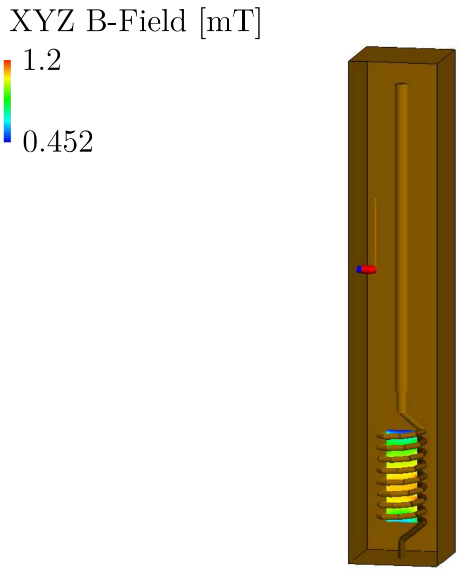

Figure 4.5: FEKO design of the helical resonator.

Design equations

The design equations of the helical resonator, as first described by Zverev [34], are summarised as follows

$$Z_0 = \frac{136\ 190}{df_0}, \tag{73}$$

$$N_h = \frac{2674}{df_0}, \tag{74}$$

$$Q = 35.9d\sqrt{f_0}, \tag{75}$$

where Z_0 is the characteristic impedance, d (unit cm) is the mean helix diameter, f_0 is the resonant frequency (unit MHz), N_h is the number of coil helices and Q the quality factor. Using $f_0 = 800$ MHz and calculating d, N_h and Q for a typical characteristic impedance of 50 Ω, gives $d = 3.4$ cm, $N_h = 0.98$ and $Q = 3\ 457$.

The parameter values give some insight into the practical implementation of the device. It was found after simulations that for a input power of 50 W the helical resonator is unable to generate 3 mT. The 3 mT is double the amount provided in Table 3.1 due to the linear polarisation of the helical coil resonator. The resonator also has poor homogeneity and electric field properties in the sample space and thus another design is considered.

4.3.2 Loop-gap resonator

A typical loop-gap resonator (LGR) is shown in Figure 4.6.

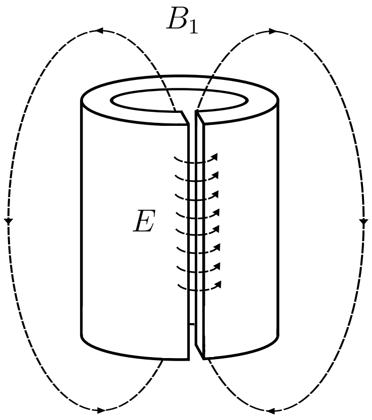

Figure 4.6: Field lines of the loop-gap resonator without shielding.

A list of the advantages, as mentioned by Rinard [35], are

- Large filling factor
- Reasonable physical size for low frequencies
- Large B_1 per square root Watt
- Fairly uniform B_1 over sample
- Good separation of E and B fields

The experimental investigation into the rf magnetic field homogeneity of the loop-gap resonator was performed by Ono et al [36]. The research performed by Ono et al, illustrates the loop-gap resonator performance in terms of the rf field homogeneity and how the loop-gap resonator can be adjusted for further improvement.

Design equations

The design equations for the loop-gap resonator have been presented by Rinard [35]. The inductance of the loop L and capacitance C of the gap are given as

$$L = \frac{\mu_0 \pi r^2}{z + 0.9r}, \tag{76}$$

$$C = \epsilon_r \epsilon_0 \frac{(w+t)\,(z+t)}{n_g t}. \tag{77}$$

where r is the inside loop radius, z the length of the loop-gap resonator, ϵ_0 the permittivity of free-space, w gap width, t gap thickness and n_g number of loop gaps. The resonant frequency and resistance of the loop-gap resonator are given by

$$f_0 = \frac{1}{2\pi\sqrt{LC}}, \tag{78}$$

$$R = 2\sqrt{\frac{\mu_0 \pi f_0}{\sigma}} \left(\frac{\pi r + \frac{w}{3}}{z} \right). \tag{79}$$

The total root-mean-square B_{1t} per square root Watt input power P is calculated using the following methodology for a single loop

$$B_{1t} = \frac{\phi}{A}, \tag{80}$$

$$\phi = LI, \tag{81}$$

where ϕ is the total loop magnetic flux and A the cross-sectional area of the loop. The circulating current I is given by

$$I = \sqrt{\frac{P}{R}}. \tag{82}$$

Combining the set of equations leads to

$$\frac{B_{1t}}{\sqrt{P}} = \frac{L}{A\sqrt{R}}. \tag{83}$$

The peak circular component of the total magnetic field is given by $B_{1p} = \frac{B_{1t}}{\sqrt{2}}$, which leads to

$$\frac{B_{1p}}{\sqrt{P}} = \frac{L}{A\sqrt{2R}}. \tag{84}$$

A proportionality relating the peak magnetic field strength to the loop-gap properties is derived by Froncisz and Hyde [37],

$$B_{1p} \propto \sqrt{\frac{QP}{f_0 r^2 z}}. \tag{85}$$

The equation describes how the power incident on the resonator, quality factor and frequency each affect the magnetic field magnitude. The loop-gap radius r however has a larger effect compared to the other parameters, and hence another reason for it to be made small, approximately 10 mm.

The loop-gap resonator, excited via inductive coupling, was designed and simulated in FEKO® [38], as illustrated by the computer-aided design (CAD) diagram in Figure 4.7. The loaded loop-gap resonator was also simulated in FEKO using the various tested samples. In order to understand how the samples interact with the LGR a detailed model of the samples is presented.

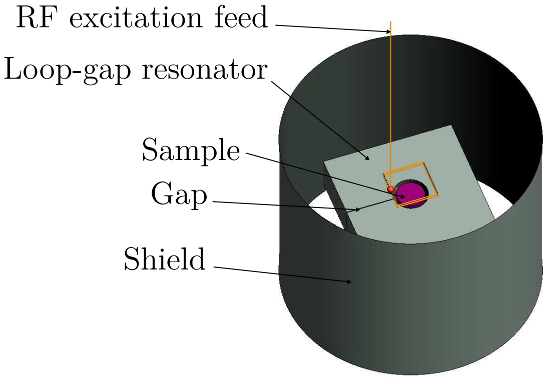

Figure 4.7: The loop-gap resonator as designed in FEKO.

4.4 Electromagnetic & Chemical Properties of the Sample

The electromagnetic properties of a material are given by the relative complex magnetic permeability $\hat{\mu}_r(\omega)$ and the relative complex permittivity $\hat{\epsilon}_r(\omega)$ [39]. The relative permeability and permittivity can be expanded as

$$\hat{\mu}_r(\omega) = \mu_r'(\omega) - j\mu_r''(\omega), \tag{86}$$

$$\hat{\epsilon}_r(\omega) = \epsilon_r'(\omega) - j\epsilon_r''(\omega). \tag{87}$$

The real part ($'$) represents the energy storage ability of the material, whereas the imaginary part ($''$) represents the energy loss associated with the material. The time averaged power density loss is derived using the Poynting relation [39], and is given by

$$P_d = -\frac{\omega}{2}\int_V \left(\mu_0\mu_r''\mathbf{H}\cdot\mathbf{H}^* + \epsilon_0\epsilon_r''\mathbf{E}\cdot\mathbf{E}^*\right)dv - \frac{1}{2}\int_V \sigma_c\mathbf{E}\cdot\mathbf{E}^* dv, \tag{88}$$

which is further compacted into

$$P_d = -\frac{\omega}{2}\int_V \left(\mu_0\mu_r''\mathbf{H}\cdot\mathbf{H}^*\right)dv - \frac{1}{2}\int_V \sigma_t\mathbf{E}\cdot\mathbf{E}^* dv. \tag{89}$$

The conduction term is given by $\sigma_t = \sigma_c + \sigma_d$, with the term $\sigma_d = \omega\epsilon_0\epsilon_r''$ representing the equivalent "conductivity" due to the dipole relaxation losses. The electromagnetic properties, obtained from literature [39], of various liquid samples are shown in Table 4.2.

Table 4.2: Complex permittivity and permeability of various test substances with the MRI contrast agents at 0.5 M vial concentration, sourced from [39].

Solution	ϵ_r'	$\sigma_t\vert_{3\text{GHz}}$**(S/m)**	σ_c **(S/m)**	$\sigma_d\vert_{3\text{GHz}}$**(S/m)**	μ_r'	μ_r''
Water	77.76	2.098	0.0002	2.098	1.087	-0.0001
Saline*	75.25	3.456	1.4100	2.046	–	–
Magnevist	49.75	3.320	0.568	2.752	1.474	0.0088
Dotarem	56.65	3.402	0.435	2.967	1.276	0.0029
ProHance	60.54	2.857	0.0504	2.807	1.690	0.02

The results show that the lowest conducting σ_c contrast agent is ProHance due to the fact the other two contrast agents are known to be anionic compounds: Magnevist is Gd[DTPA]$^{2-}$ and Dotarem Gd[DOTA]$^{-}$ [39]. The chelate of the compound is therefore responsible for the increase in σ_c not the charge number of the gadolinium ion [39]. The slight increase in σ_c of ProHance is a result of the small amount of excipients found in the contrast agent medium [39]. It is therefore noted that Magnevist and Dotarem are relatively weak electrolytes whereas ProHance is non-electrolytic.

The values, besides that of σ_c, in Table 4.2 are only valid at 3 GHz, however assuming a square dependence on frequency the values can be adjusted accordingly. The square dependence is assumed from the statement by Ogunlade [39], which is that σ_d of water is increased from 0.0024 $\text{S}\cdot\text{m}^{-1}$ at 100 MHz, to 0.243 $\text{S}\cdot\text{m}^{-1}$ at 1 GHz. The σ_d therefore of water, saline, Magnevist, Dotarem and ProHance is 0.181 $\text{S}\cdot\text{m}^{-1}$, 0.176 $\text{S}\cdot\text{m}^{-1}$, 0.237 $\text{S}\cdot\text{m}^{-1}$, 0.255 $\text{S}\cdot\text{m}^{-1}$ and 0.241 $\text{S}\cdot\text{m}^{-1}$ at 880 MHz respectively.

---

[*] Physiological saline 9 $\text{g}\cdot\text{l}^{-1}$ NaCl

The total conductance σ_t therefore of water, saline, Magnevist, Dotarem and ProHance is 0.1812 $\mathrm{S \cdot m^{-1}}$, 1.586 $\mathrm{S \cdot m^{-1}}$, 0.805 $\mathrm{S \cdot m^{-1}}$, 0.6903 $\mathrm{S \cdot m^{-1}}$ and 0.2914 $\mathrm{S \cdot m^{-1}}$ respectively. The total conductance of saline for example is 1.586 $\mathrm{S \cdot m^{-1}}$ at 880 MHz, whereas for blood is 1.529 $\mathrm{S \cdot m^{-1}}$ at 880 MHz [21], which further validates the assumption of square-dependence.

4.4.1 Magnetic loss

The magnetic loss of the medium is represented by μ_r'' and as shown in Table 4.2 is relatively small compared to the total conductive σ_t loss at 3 GHz. The reason, as described by Ogunlade [39], is because the magnetic loss mechanisms are generally low frequency phenomena in the range of kHz-MHz. The magnetic properties are therefore not included in the modelling due to this fact and also given that the operating frequency is in the range of MHz-GHz.

4.4.2 Sample permittivity

The relative permittivity ϵ_r', although not explicitly given in Equation 88, has a significant affect on the power loss. The 0.5 M contrast agents Magnevist, Dotarem and ProHance contain 469 g, 376.8 g and 279.4 g of solute in 1 l of solvent respectively [39]. A higher solute concentration results in a larger number of displaced water molecules for a given volume. Together with the high permittivity of water, substances like ProHance and Saline have a resulting larger ϵ_r.

The larger permittivity in ProHance and Saline will in effect reduce the electric field and corresponding power loss. The conclusion is that substances like ProHance are better suited for testing purposes as both its conductivity σ_c and permittivity ϵ_r' result in low losses, both induction and electric.

4.4.3 Contrast agent structure

The development of contrast agents is both interesting and important in terms of their chemical structure and properties. The following information with regard to ProHance, compared to the other contrast agents, can be obtained from Tweedle [28]. The chelate structures of the contrast agents used in experimentation are shown in Figure 4.8.

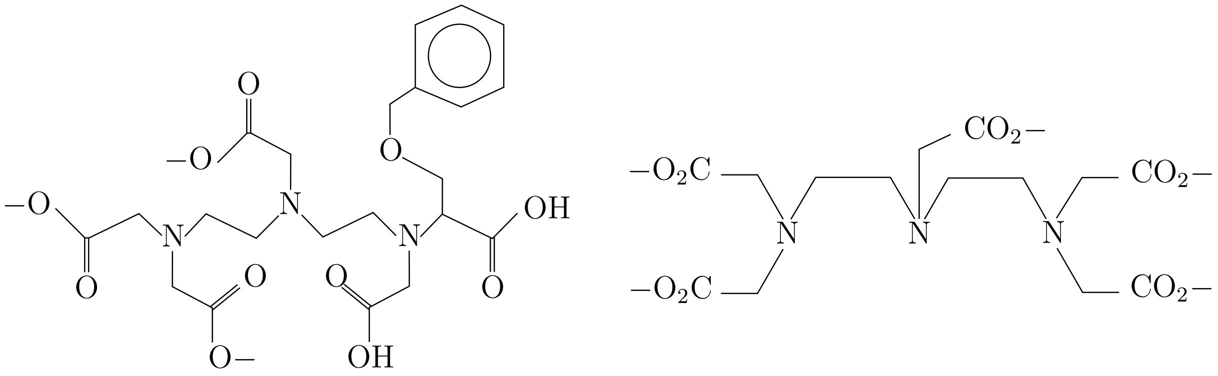

BOPTA
Gadobenate

DTPA
Gadopentetate

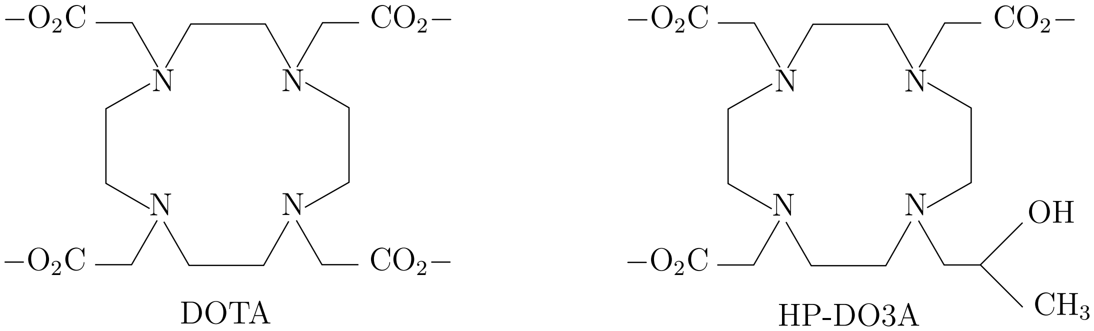

DOTA
Gadoterate

HP-DO3A
Gadoteridol

Figure 4.8: Chelate structures of the contrast agents used in the study [28].

Compared to the other contrast agents ProHance is the only molecule having both non-ionic and macrocyclic properties. The non-ionic property of ProHance allows for greater osmotolerance, dosing and formulation flexibility. The macrocyclic property gives the molecule greater thermodynamic stability. The relative chemical properties of the contrast agents are compared in Table 4.3. The extra NMG$^+$ (N-methylglucammonium) molecules used to neutralise the chelates of Dotarem and Magnevist results in a higher solution conductivity, osmolality and viscosity.

Table 4.3: Contrast agent conductivity at 20 °C, molar osmolality and viscosity at 37 °C, sourced from [28].

Agent	**Conductivity ($\mathbf{S \cdot cm^2/mmol}$)**	**Osmolality (Osmol/kg)**	**Viscosity (cP)**
ProHance	1	0.63	1.3
Omniscan	5.5	0.65	1.4
Magnevist	117	1.96	2.9
Dotarem	54	1.35	2.0
MultiHance	–	1.97	5.3

4.5 Specific Absorption Rate Simulation

The specific absorption rate is simulated in the electromagnetic (EM) simulation software FEKO [38]. FEKO has a hybrid finite element method (FEM)/method of moments (MoM) technique which optimises the simulation performance when the modelled system has a mixture of homogeneous metal structures (antennas, resonators etc) and inhomogeneous complex dielectric structures (humans, test samples etc). The SAR is defined as

$$SAR = \int_{sample} \frac{\sigma(\mathbf{r})|\mathbf{E}(\mathbf{r})|^2}{\rho(\mathbf{r})} d\mathbf{r}, \tag{90}$$

and has units of $\mathrm{W} \cdot \mathrm{kg}^{-1}$. An example is that mobile cell phones in Europe have a SAR limited to 2.0 $\mathrm{W} \cdot \mathrm{kg}^{-1}$ averaged over 10 g of tissue. Equation 90 shows that if the conductance is decreased then the SAR will decrease linearly.

The simulation results for the various test solutions, which are shielded with copper strips, are shown in Table 4.4 using the MoM/multilevel fast multipole method (MLFMM) with volume equivalence principle (VEP) solver, and Table 4.5 using the FEM solver. The tabulated results are for a transmitted power of 50 W, with the source voltage standing wave ratio (VSWR) given and the volume averaged SAR measured over the entire sample.

Table 4.4: Volume averaged SAR simulation results for shielded substances using the MoM/MLFMM VEP dielectric setting with 50 W input power.

Solution	f_0 **(MHz)**	**VSWR**	E **(kV/m)**	$2B_1$ **(mT)**	**SAR (W/kg)**
Water	819.65	1.23	7.91	3.27	18,310
Saline	819.30	1.50	6.35	2.50	100,520
Magnevist	820.87	1.16	7.33	2.70	64,180
Dotarem	820.62	1.10	7.92	2.77	58,606
ProHance	818.19	1.12	9.45	3.10	31,740

Table 4.5: Volume averaged SAR simulation results for shielded substances using the FEM dielectric setting with 50 W input power.

Solution	f_0 **(MHz)**	**VSWR**	E **(kV/m)**	$2B_1$ **(mT)**	**SAR (W/kg)**
Water	841.18	1.22	9.05	3.24	18,890
Saline	839.50	1.69	6.33	2.34	116,360
Magnevist	840.53	1.24	8.62	2.62	67,550
Dotarem	841.42	1.14	8.40	2.71	54,606
ProHance	838.55	1.10	9.56	3.07	33,900

The input power levels irradiating the sample, shown in Table 4.6, are similar to those used in experimentation. In the experimental results section the transmitted power is measured using the forward and reverse power built-in detection system of the rf amplifier. The temperature rise of each sample due to the SAR, assuming a specific heat value of water $C = 4.183\ \mathrm{J \cdot g^{-1} \cdot K^{-1}}$, is presented in Table 4.6.

Table 4.6: Average of FEM and MoM SAR with resulting temperature rise for shielded substances using power levels comparable to experimentation.

Solution	$\boldsymbol{P}$ **(W)**	$\mathbf{2}\boldsymbol{B_1}$ **(mT)**	**SAR (W/kg)**	$\frac{\Delta T}{\Delta t}$ **(°C/s)**	$\frac{\Delta T}{P\Delta t}$ **(°C/s/W)**
Water	1.75	0.607	853	0.204	0.117
Saline	2.01	0.464	4,200	1.01	0.502
Magnevist	1.91	0.516	1,610	0.384	0.201
Dotarem	1.91	0.536	2,162	0.517	0.271
ProHance	1.91	0.603	1,160	0.277	0.145

The results show that a reasonable magnetic flux density, $B_1 \approx 0.3$ mT in the samples is obtained for low-input powers. Water being less conductive than the other substances has a relatively low SAR value as compared to Saline. Although the SAR values are high for each substance the effect could be minimised by using a pulsed rf input or by using appropriate shielding around the patient.

It is noted that the purpose of this research is to demonstrate a measurable effect of electron spin resonance heating in well-known paramagnetic liquid substances, with developments toward a practical technology left for future work.

4.5.1 T1 fibre optic thermometer model

A fibre optic thermometer is used in the experiments to measure the temperature rise in the sample. The fibre optic thermometry allows for the temperature measurement to be performed within a large rf field and high voltage environment as the probe contains no metal elements [40]. The dimensions and materials of the fibre optic are shown in Figure 4.9.

The probe dynamics are modelled and compared to measurement using a standard step response. The step up and step down response is performed by clasping the last 5 mm of the probe between the fingers until steady-state is reached and then released. The fibre optic is modelled as a thermal circuit as shown in Figure 4.10. The subscripts of the circuit elements relate to the probe materials (t-PTFE coating, p-polyimide), fingers (s-skin) and the ambient conditions (a-air).

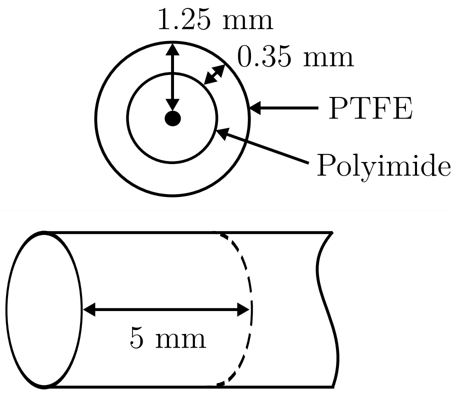

Figure 4.9: Cross-sectional and side view of the Neoptix T1 fibre optic probe.

As shown in Figure 4.10 the resistor R_s, as well as the voltage source, is switched at a later time during the experiment to achieve the ambient step down response when the fingers release the probe.

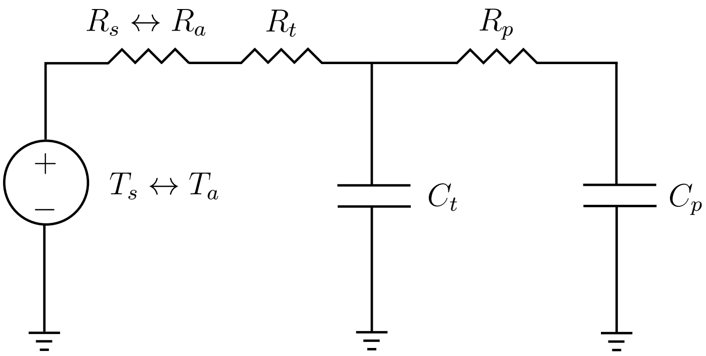

Figure 4.10: Thermal circuit equivalent model of the Neoptix fibre optic thermometer T1 probe.

The thermal resistors in the circuit model are calculated using the following formulae

$$R_s = \frac{l_s}{A_s k_s}, \tag{91}$$

$$R_a = \frac{l_a}{A_a k_a}, \tag{92}$$

$$R_t = \frac{l_t}{A_t k_t}, \tag{93}$$

$$R_p = \frac{l_p}{A_p k_p}, \tag{94}$$

where l is the thermal conductor thickness, A is the cross-sectional area and k the thermal conductivity. The differential equations for the thermal system are as follows

$$Q_t = m_t C_t T_t, \tag{95}$$

$$Q_p = m_p C_p T_p, \tag{96}$$

$$\dot{Q}_t = \frac{T_s - T_t}{R_s + R_t}, \text{ for } t \leq 62 \text{ s}, \tag{97}$$

$$\dot{Q}_t = \frac{T_a - T_t}{R_a + R_t}, \text{ for } t > 62 \text{ s}, \tag{98}$$

$$\dot{Q}_p = \frac{T_t - T_p}{R_p}, \tag{99}$$

where Q represents the sensible heat stored in the respective material, C is the specific heat capacity and m the mass of the substance.

The properties of the probe materials, skin and temperature sources are presented in Table 4.7. The thickness of the skin l_s and the air sleeve, via the process of adsorption, l_a are assumed to be 2 mm and 1 mm respectively, with the thermal conductivity of human skin obtained from Holmes [41]. The contact length for the probe is 5 mm with a cylindrical radius given in Figure 4.9. The conductive area for the polytetrafluoroethylene (PTFE) and polyimide materials is calculated by using the outer circumference and the contact length.

Table 4.7: List of parameters used in the T1 probe circuit model.

Parameter	**Value**	**Units**
R_s	122.35	$\text{K} \cdot \text{W}^{-1}$
R_a	1018.59	$\text{K} \cdot \text{W}^{-1}$
R_t	35.65	$\text{K} \cdot \text{W}^{-1}$
R_p	265.26	$\text{K} \cdot \text{W}^{-1}$
m_t	26	mg
m_p	18	mg
C_t	1.005	$\text{J} \cdot \text{g}^{-1} \cdot \text{K}^{-1}$
C_p	1.09	$\text{J} \cdot \text{g}^{-1} \cdot \text{K}^{-1}$
T_s	31.2	°C
T_a	20	°C

The plot in Figure 4.11 shows good agreement, with a calculated normalised root-mean-square error (NRMSE) of 3.66 %, between the model and the experimental results. Note that only two parameters T_s and T_a have been adjusted accordingly.

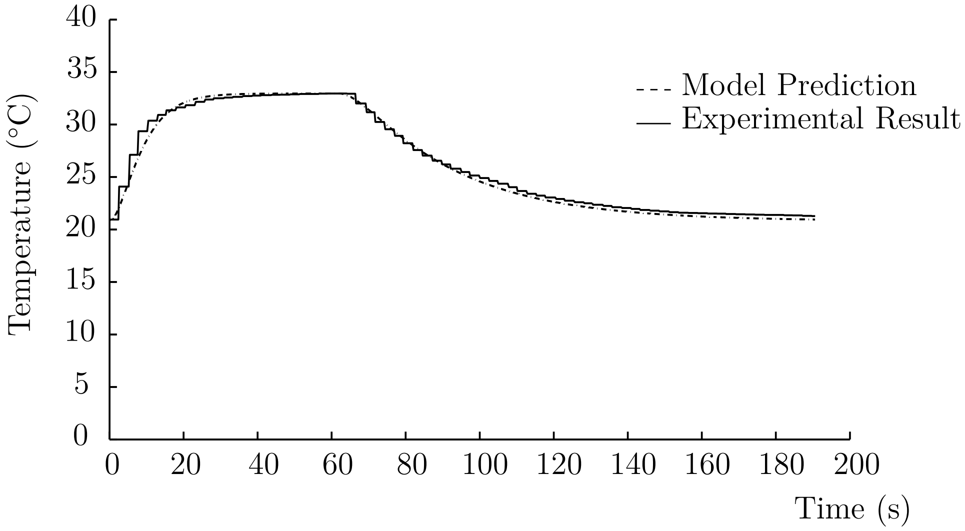

Figure 4.11: Model prediction and experimental step-response of the fibre optic probe.

4.5.2 Sample tube thermal model

The contrast agents are placed within a PTFE tube as shown in Figure 4.12. The thermal and dielectric properties of the PTFE material made it a suitable choice for a container. The dimensions are similar to that of the loop in the loop-gap resonator. The PTFE tube is cut with both ends open. The ends of the tube were sealed initially using PTFE tape and then later caped with PLA plastic. The one side of the container is drilled out so that the polyimide fibre optic probe can be inserted securely.

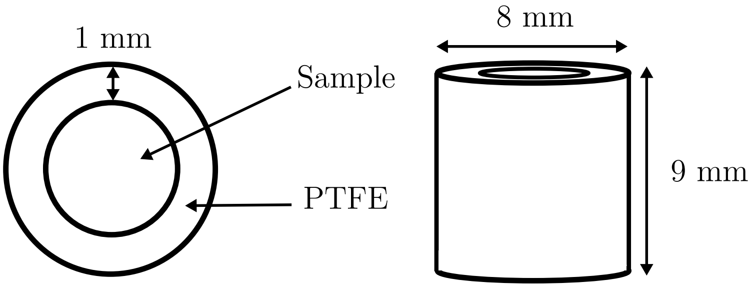

Figure 4.12: Top and front view of the unshielded PTFE sample container.

The PTFE tube/container can contain a sample with a volume of approximately 0.25 ml. A thermal circuit equivalent model of the tube with a liquid water sample inside is illustrated in Figure 4.13.

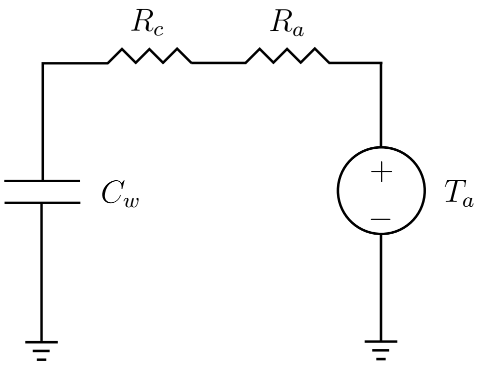

Figure 4.13: Circuit thermal model of sample tube containing water.

The model assumes that a 1 mm layer of air, which via adsorption surrounds the PTFE container, which is a similar assumption used in the fibre optic thermometer model. The subscripts in the thermal circuit model are: w-water, a-air and c-PTFE container. The thermal resistors in the circuit model are calculated using the following formulae

$$R_a = \frac{l_a}{A_a k_a}, \tag{100}$$

$$R_c = \frac{l_c}{A_c k_c}. \tag{101}$$

The differential equations for the thermal system, assuming the water sample is at a higher temperature compared to the ambient temperature, are as follows

$$Q_w = m_w C_w T_w, \tag{102}$$

$$\dot{Q}_w = \frac{T_w - T_a}{R_c + R_a}. \tag{103}$$

The thermal properties of the water, container and initial conditions are presented in Table 4.8.

Table 4.8: List of parameters used in the sample tube model.

Parameter	**Value**	**Units**
R_c	39.52	$\mathrm{K \cdot W^{-1}}$
R_a	163.75	$\mathrm{K \cdot W^{-1}}$
m_w	254.5	mg
C_w	4.1813	$\mathrm{J \cdot g^{-1} \cdot K^{-1}}$
$T_w(0)$	21	°C
T_a	17.1	°C

The decay-response, i.e. no exciting source or input, from steady-state of liquid water inside the sample tube is shown in Figure 4.14. The NRMSE for the model fit of the water sample inside the container using the experimental data is 4.59 %.

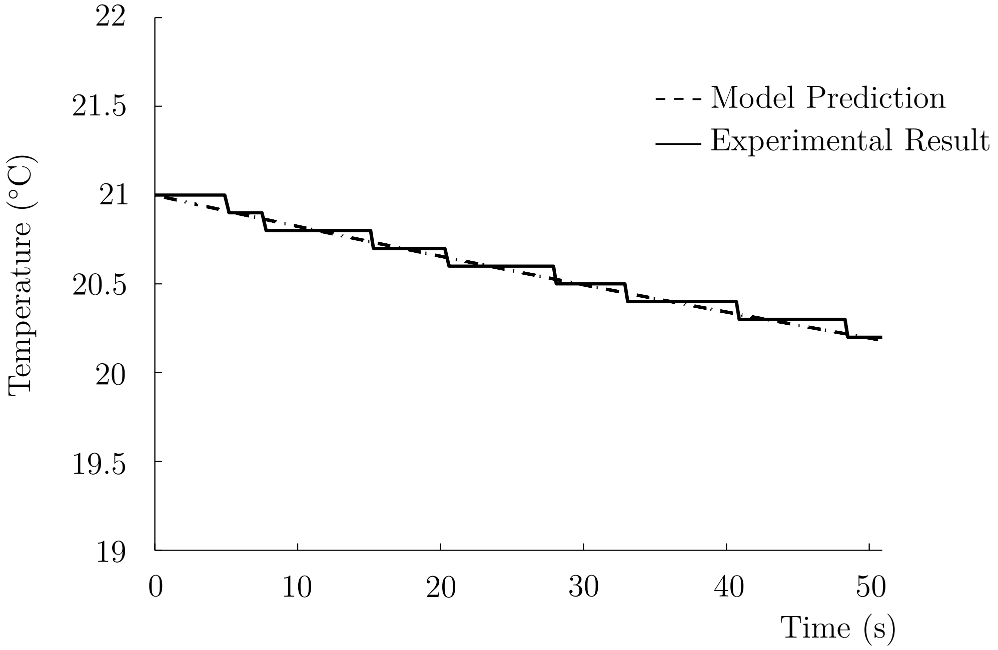

Figure 4.14: Model prediction and experimental decay-response of the water sample inside the container.

It should be noted that the temperature measurement is performed using the T1 temperature probe [40], and an assumption is made that the 250 ms response time to reach 63 % of the final value of the probe does not affect the reading. Further, the fact that the probe occupies a relatively small-volume (24.5 nl) compared to the container (254 µl) results in the thermal dynamics of the container being accurately measured.

4.5.3 Thermal model of sample tube with realistic probe

Combining the fibre optic thermometer model with the sample tube model allows one to determine certain unknown parameters. An important unknown parameter is the power due to Ohmic loss ($\dot{Q}_l$) in the sample; that is to say the heating created by the influences of magnetic and electric fields on the conductive sample. The second unknown parameter which can be determined from the combined system model is the specific heat capacity of the liquid, which is not stated in the literature for the contrast agents.

The system equations for the combined model are given as

$$\dot{Q}_w = \dot{Q}_l - \frac{T_w - T_a}{R_c + R_a} - \frac{T_w - T_t}{R_t}, \text{ for } t \leq 30 \text{ s}, \tag{104}$$

$$\dot{Q}_w = -\frac{T_w - T_a}{R_c + R_a} - \frac{T_w - T_t}{R_t}, \text{ for } t > 30 \text{ s}, \tag{105}$$

$$\dot{Q}_t = \frac{T_w - T_t}{R_t} - \frac{T_t - T_p}{R_p}, \tag{106}$$

$$\dot{Q}_p = \frac{T_t - T_p}{R_p}. \tag{107}$$

where $\dot{Q}_l$ is the power due to the Ohmic losses in the liquid sample. It is assumed that $\dot{Q}_l$ stays constant during the 30 second irradiation of the sample, which is validated by experimentation. The combined system step response of liquid water using a pulse input of 3.88 W and duration of 30 seconds, is shown in Figure 4.15.

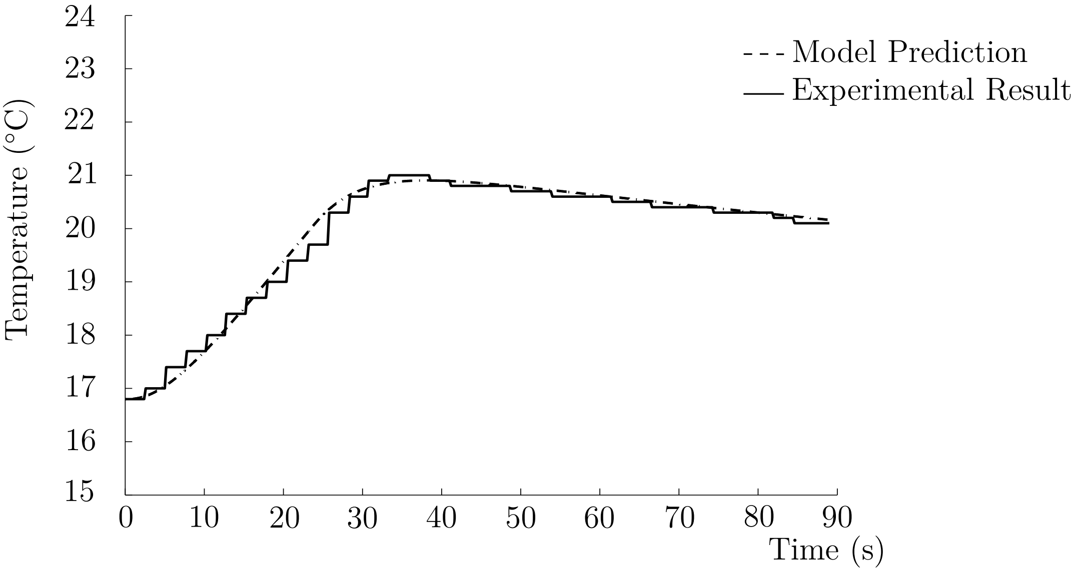

Figure 4.15: Model prediction and experimental step response results of the combined system with water sample.

The model and experimental results show good agreement as presented in the plot. Using this combined model one can determine the Ohmic loss and specific heat capacities of the contrast agents.

The model and experimental results for Saline, using an input of 3.07 W for a duration of 27 seconds is shown in Figure 4.16.

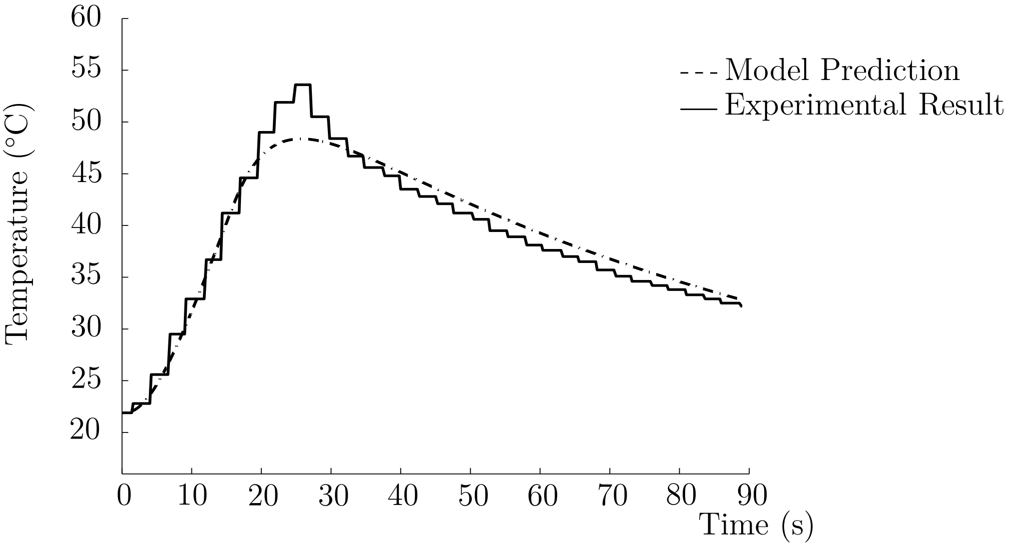

Figure 4.16: Model prediction and experimental step response results of the combined system with Saline sample.

The model and experimental results for MultiHance, using an input of 3.47 W for a duration of 25 seconds is shown in Figure 4.17.

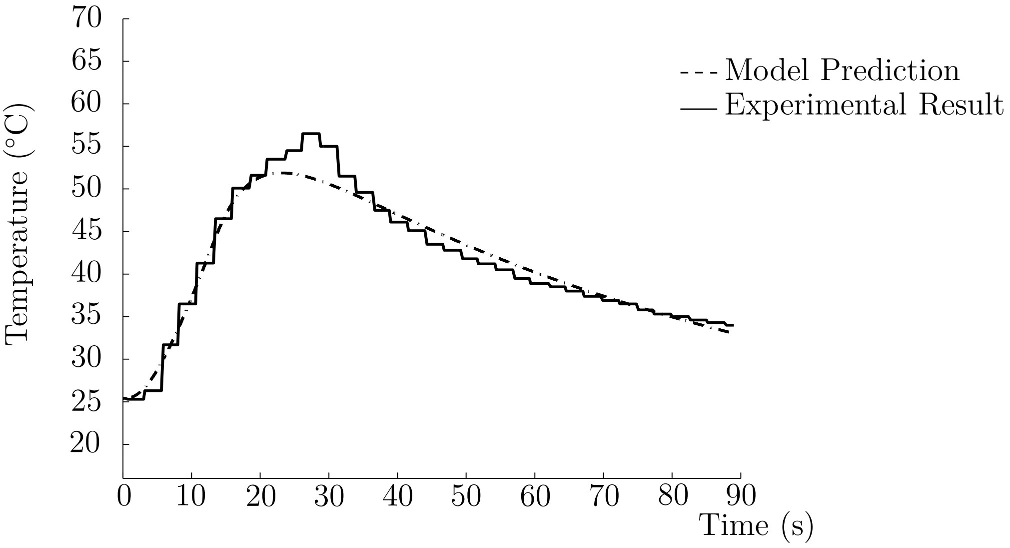

Figure 4.17: Model prediction and experimental step response results of the combined system with MultiHance sample.

The model and experimental results for Magnevist, using an input of 3.16 W for a duration of 25 seconds is shown in Figure 4.18.

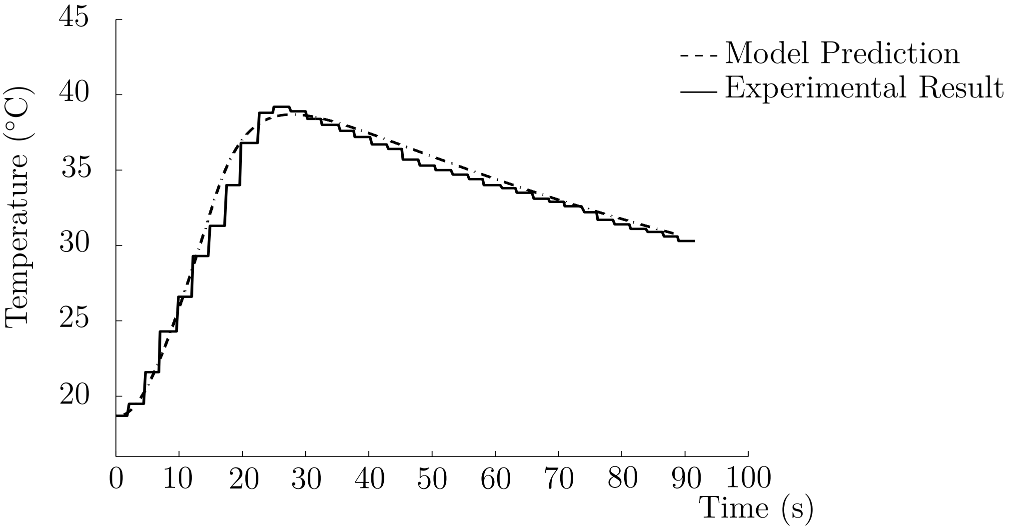

Figure 4.18: Model prediction and experimental step response results of the combined system with Magnevist sample.

The model and experimental results for Dotarem, using an input of 3.67 W for a duration of 26 seconds is shown in Figure 4.19.

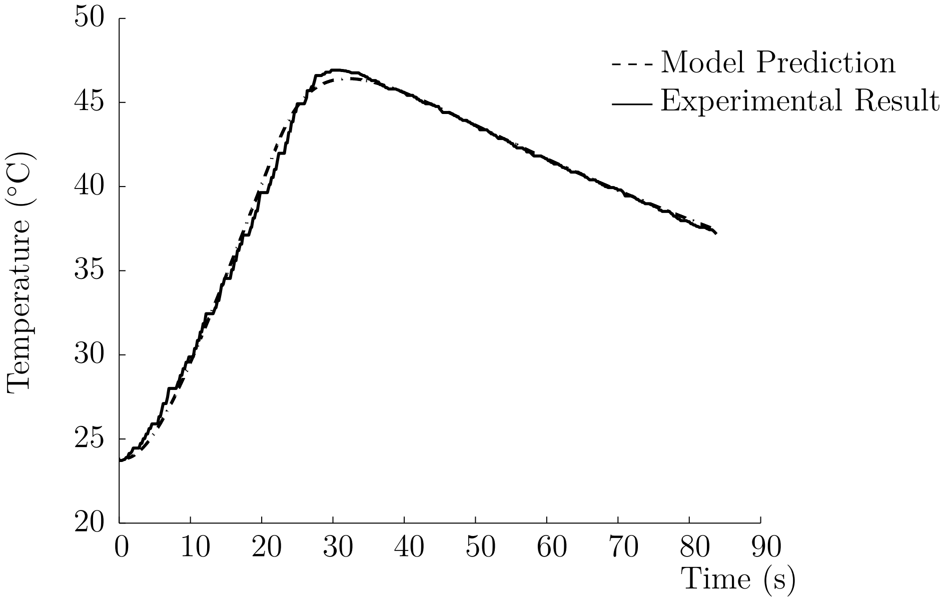

Figure 4.19: Model prediction and experimental step response results of the combined system with Dotarem sample.

The model and experimental results for ProHance, using an input of 3.62 W for a duration of 25 seconds is shown in Figure 4.20.

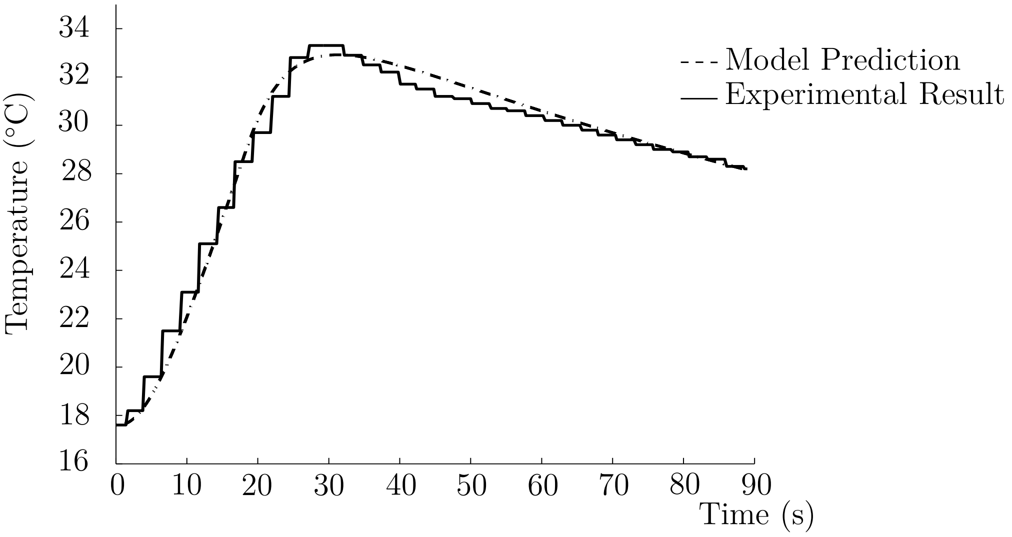

Figure 4.20: Model prediction and experimental step-response results of the combined system with ProHance sample.

The model and experimental results of the decay-response from steady-state for water, as shown in Figure 4.21.

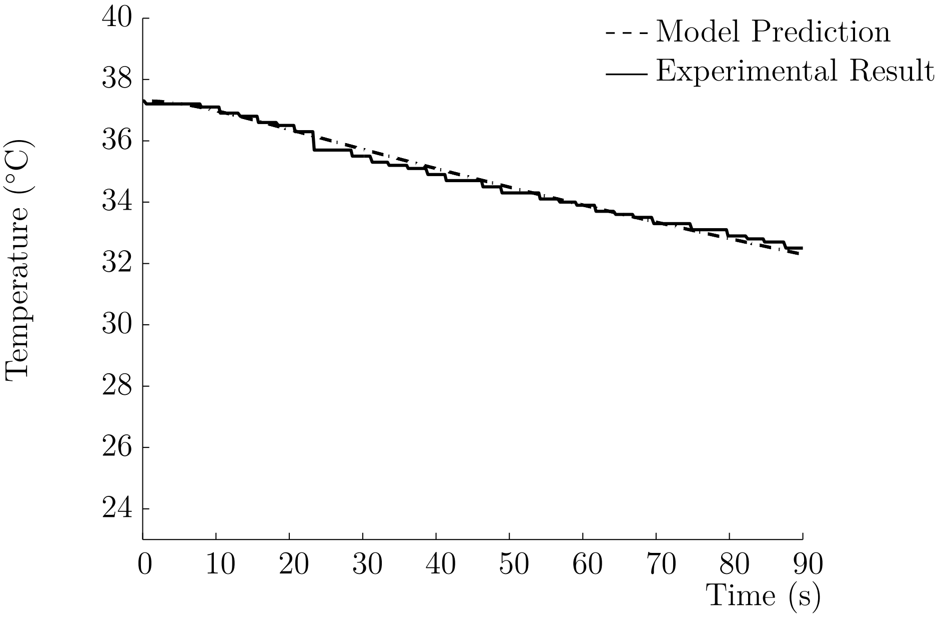

Figure 4.21: Model prediction and experimental decay-response results of the combined system with water sample.

The model and experimental results of the decay-response from steady-state for saline, as shown in Figure 4.22.

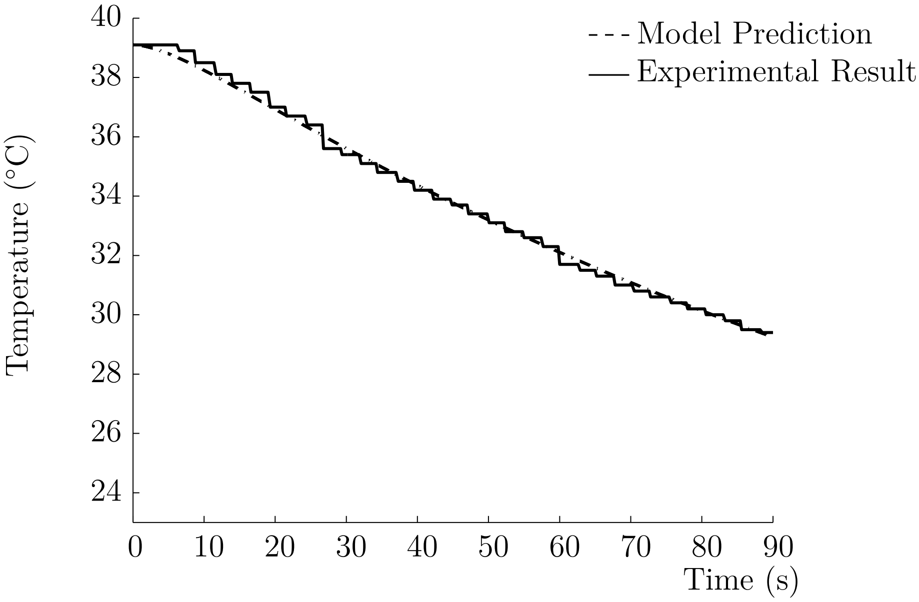

Figure 4.22: Model prediction and experimental decay-response results of the combined system with saline sample.

The model and experimental results of the decay-response from steady-state for MultiHance, as shown in Figure 4.23.

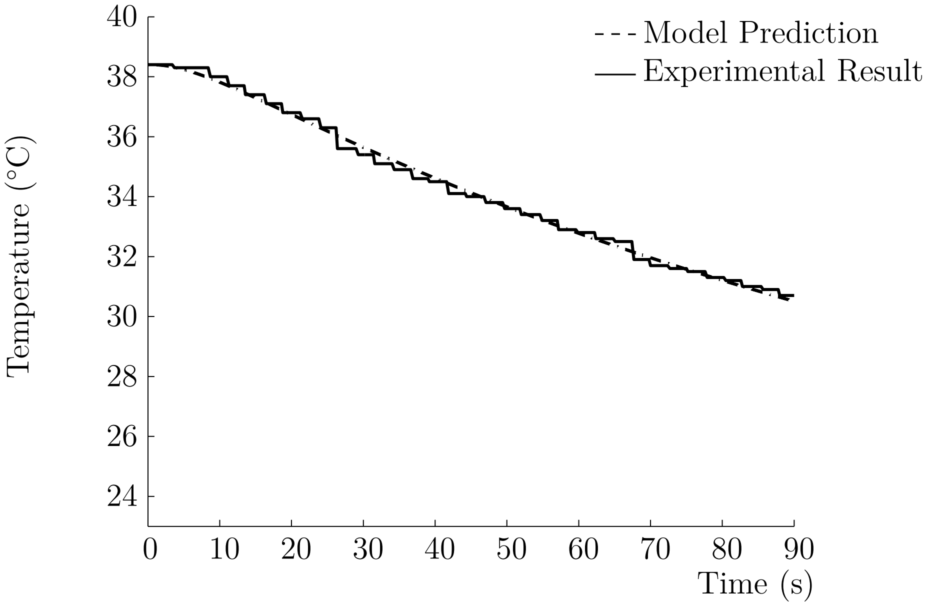

Figure 4.23: Model prediction and experimental decay-response results of the combined system with MultiHance sample.

The model and experimental results of the decay-response from steady-state for Magnevist, as shown in Figure 4.24.

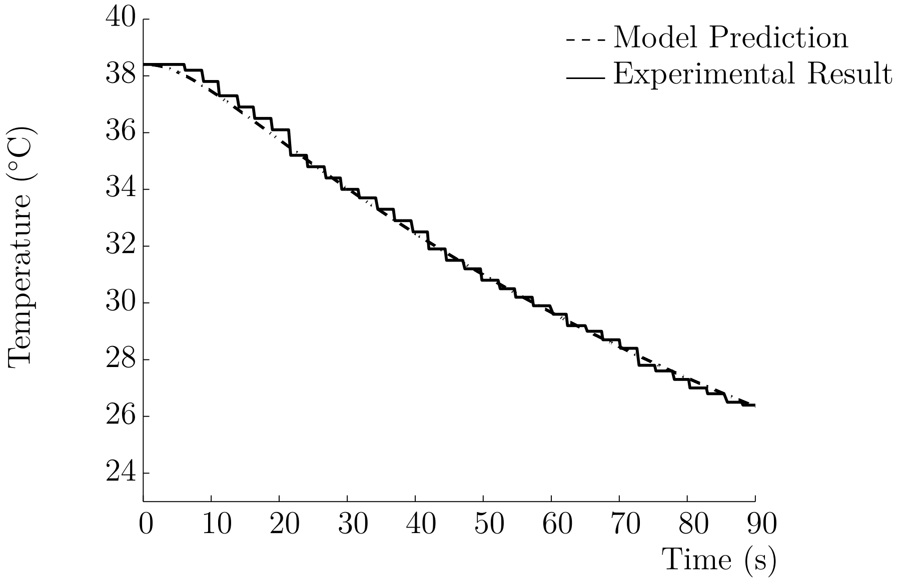

Figure 4.24: Model prediction and experimental decay-response results of the combined system with Magnevist sample.

The model and experimental results of the decay-response from steady-state for Dotarem, as shown in Figure 4.25.

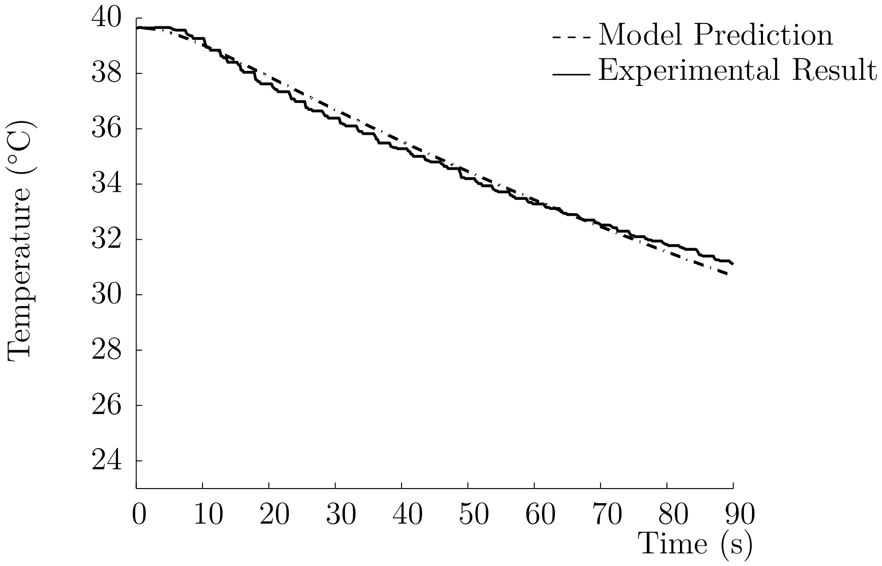

Figure 4.25: Model prediction and experimental decay-response results of the combined system with Dotarem sample.

The model and experimental results of the decay-response from steady-state for ProHance, as shown in Figure 4.26.

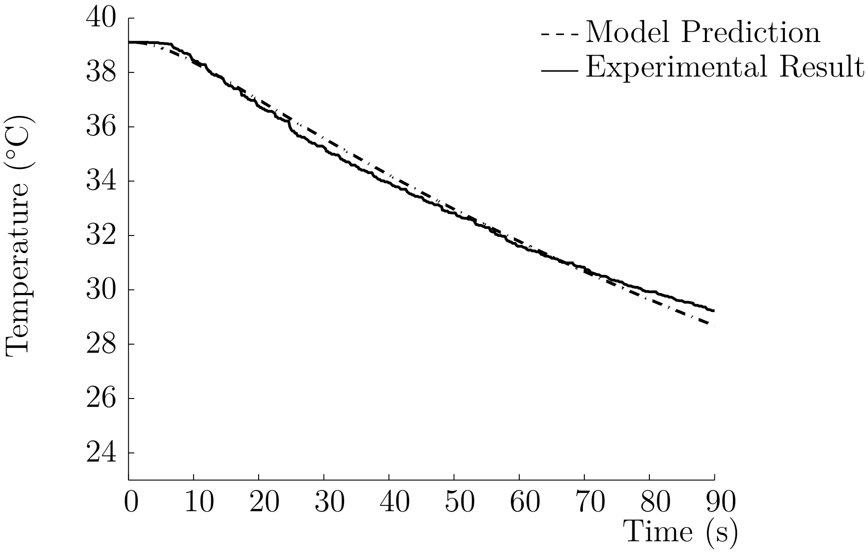

Figure 4.26: Model prediction and experimental decay-response results of the combined system with ProHance sample.

It is evident from the step-response curves, Figures 4.15–4.20, that the RF exposure time varies with an average of approximately 25 s. Each substance heated differently, and care was taken to avoid temperature rises above 55 °C for fear of causing the capsule to explode.

The model parameters are obtained by minimising the NRMSE of the model fit, for the six substances, and are given in Table 4.9.

Table 4.9: List of estimated parameters: pulsed-response (C_Δ), decay-response (C_d) and average response ($\bar{C}$) with associated errors for the various substances used in the combined thermal model.

Substance	$\boldsymbol{m}$ **(g)**	$\boldsymbol{C_\Delta}$	**NRMSE %**	$\boldsymbol{C_d}$	**NRMSE %**	$\boldsymbol{\bar{C}}$ $(\mathbf{J \cdot g^{-1} \cdot K^{-1}})$
Water	0.25447	4.18	3.28	4.53	3.20	4.36
Saline	0.25447	1.35	5.83	2.63	1.86	1.99
MultiHance	0.3105	1.0	5.19	1.86	2.02	1.43
Magnevist	0.3041	1.7	3.60	1.59	1.65	1.65
Dotarem	0.2991	1.78	1.67	2.72	2.95	2.25
ProHance	0.28933	2.10	2.52	2.36	2.57	2.23

The average between the pulsed-response (C_Δ) and decay-response (C_d) is used to determine the specific heat values of the substances. It is shown in Table 4.9 that the errors for the model fits are relatively small and that the model predicts the responses of the experiments fairly accurately.

It is interesting to note how the specific heat capacity between different substances varies. Water has the highest specific heat due to the hydrogen bonding between the molecules whilst the high solute concentration of the contrast agents tends to decrease their specific heat capacity value.

4.5.4 Ohmic power loss

The combined model of the thermal properties of the sample tube and fibre optic thermometer is used to determine the bulk ohmic losses of each sample. The Ohmic power loss is presented in Table 4.10. The Ohmic loss is also normalised to the input power used during each experiment and presented as the 'Power Ratio' in Table 4.10.

Table 4.10: Ohmic power loss and power ratio of each substance for a given input power P_{in} as determined from the combined thermal model, and the experimental results.

Substance	**P_{in} (W)**	**Ohmic Loss (W)**	**Power Ratio (dB)**
Water	3.88	0.219	-12.5
Saline	3.07	0.902	-5.3
MultiHance	3.47	0.972	-5.5
Magnevist	3.16	0.9	-5.5
Dotarem	3.67	0.765	-6.8
ProHance	3.62	0.646	-7.5

The results show that water has the lowest power ratio, due to its low conductivity properties, as opposed to saline which has the highest. It is noted from the results that although ProHance has a relatively low DC conductivity, it is the total conductivity that significantly determines the Ohmic loss in the material.

4.5.5 Specific absorption rate prediction

Using the combined thermal model and the experimental results the SAR for each substance can be estimated. The results are compared to the SAR predictions using FEKO, as shown in Table 4.11. The results show that there is good agreement between the modelled and experimental results which helps to validate the rf magnetic values B_1 used in the calculations.

Table 4.11: SAR predictions for unshielded samples using FEKO compared to the experimental pulse-response results.

Substance	P_{in} **(W)**	f **(MHz)**	**FEKO SAR** $(\mathbf{W \cdot kg^{-1}})$	**SAR** $(\mathbf{W \cdot kg^{-1}})$
Water	3.88	855.9	861.4	861.3
Saline	3.07	860.4	3,795	3,408
MultiHance	3.47	859.5	–	3,131
Magnevist	3.16	857.1	2,873	2,960
Dotarem	3.67	857.3	2,527	2,558
ProHance	3.62	857.3	2,324	2,233

It should be noted that the frequencies listed in Table 4.11 are the experimental set values determined by the resonance of the loaded LGR. The LGR resonant frequency depends on the sample's conductivity, permittivity and permeability which differ for each tested substance. Comparing these results to Table 4.6 illustrates counter-intuitively that using no copper strips for shielding the sample is beneficial and results in a lower SAR, as described further in section 6.2.

5 EXPERIMENTAL APPARATUS

The specifications and part numbers of the equipment used in the experiment are presented. The manufactured DC coil system is characterised in terms of its field strength and homogeneity. A variety of configurations for the sample container are considered, modelled and selected based on the dielectric and inductive losses.

5.1 Auxiliary Equipment

5.1.1 DC bench power supply

The supply for the DC coil system should have sufficient power to overcome the copper wire resistance of the total coil length ≈ 1.7 km. The supply should be at least 1300 W in order to drive 10 A through the total resistance of 13 Ω. The EA-PS 8360-15 DT 1500 W laboratory power supply was purchased based on these requirements [42].

5.1.2 RF amplifier

A solid-state personal communication power amplifier, with $500-900$ MHz that can supply $0-50$ W under continuous wave operation, was purchased from HD Communications corporation (New York) in order to generate the large magnetic fields ($0-3$ mT) in the loop-gap resonator [43]. A photograph of the rf amplifier is shown in Figure 5.1.

Figure 5.1: Photograph of the rf amplifier with a sucroform coaxial feed to the loop-gap resonator within the DC coil system, inside the anechoic chamber.

5.1.3 General materials

Aluminium coil formers, 1.7 km of copper wire and other various components such as brass screws were required to manufacture the DC coil system. The loop-gap resonator required Rexolite_1422, a dielectric used in the gap section of the resonator, as well as Sucroform_141 for the rf coaxial cable feed. The department has a number of components and equipment available, such as oscilloscopes, multimeters etc. The department also has the Terranova Earth Field MRI which is used to characterise and measure the homogeneity of the spherical DC magnetic field coil system [44].

5.2 DC Magnetic Coil System

5.2.1 Setup

The DC coil system is shown in Figure 5.2, and was initially tested and characterised outside the anechoic chamber using a Hall-sensor and Terranova MRI probe. The stability of the power supply and relatively large inductance of the coil system (1.34 H) prevented the magnetic field from fluctuating more than 0.1 mT for a period greater than 30 minutes. The result of the coil resistance (12 Ω) and coil inductance is a 112 ms rise time.

Figure 5.2: Photograph of the DC coil system with the low-field Terranova unit placed inside.

The DC coil system was later placed in the anechoic chamber, as shown in Figure 5.3. The anechoic chamber is designed to filter any spurious DC and AC signals.

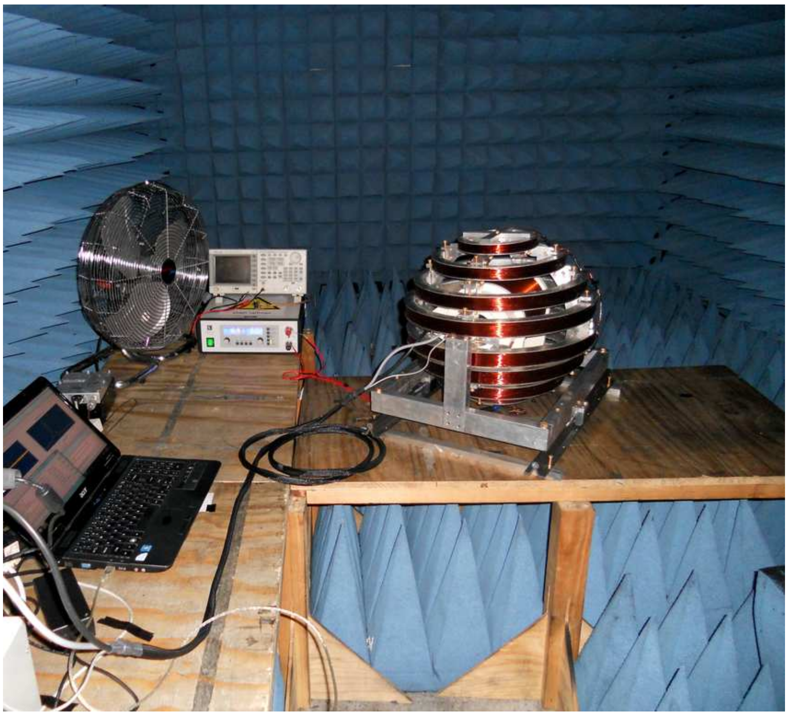

Figure 5.3: Photograph of the experimental setup in the anechoic chamber. Right: the Terranova is placed inside the coil system, Middle: power supply, Left: cooling fan and laptop with installed Terranova software.

5.2.2 Characterisation

The free-induction-decay experimental results of a 500 ml water filled bottle placed in the Terranova-EFNMR (Earth's Field Nuclear Magnetic Resonance) apparatus are shown in Figure 5.4 and Figure 5.5. A current of $15 - 20$ mA is driven through the DC coils in order to generate the $40 - 70$ μT, which is the lower and upper measurement limit of the Terranova system [44].

The free induction decay (FID) signal of water is relatively short lived when compared to the FID obtained under the earth's magnetic field [44]. The spin-spin relaxation time τ_2^* for this water bottle experiment is typically 1 s when using the homogeneous field of the earth.

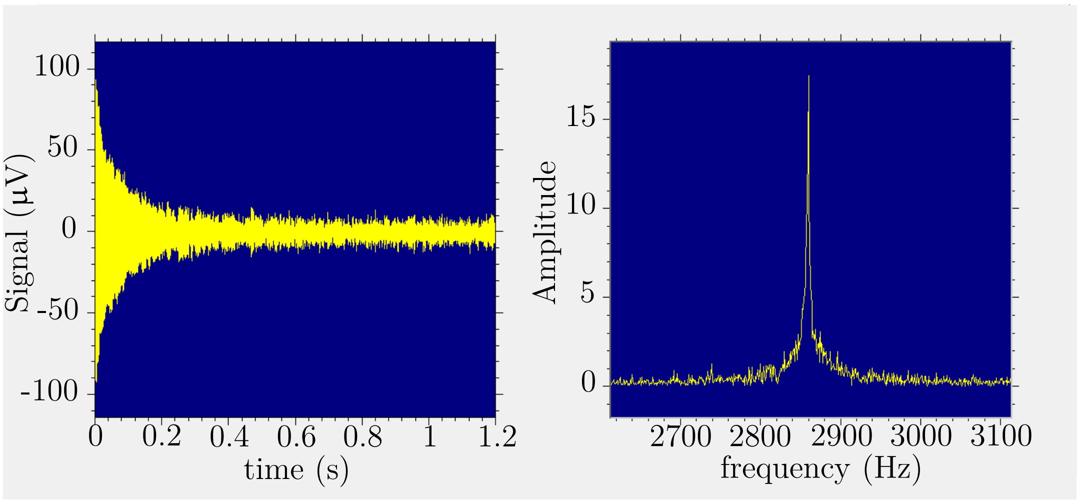

Figure 5.4: Free induction decay signal of water using the Terranova pulse-collect experiment in the anechoic chamber with no shimming.

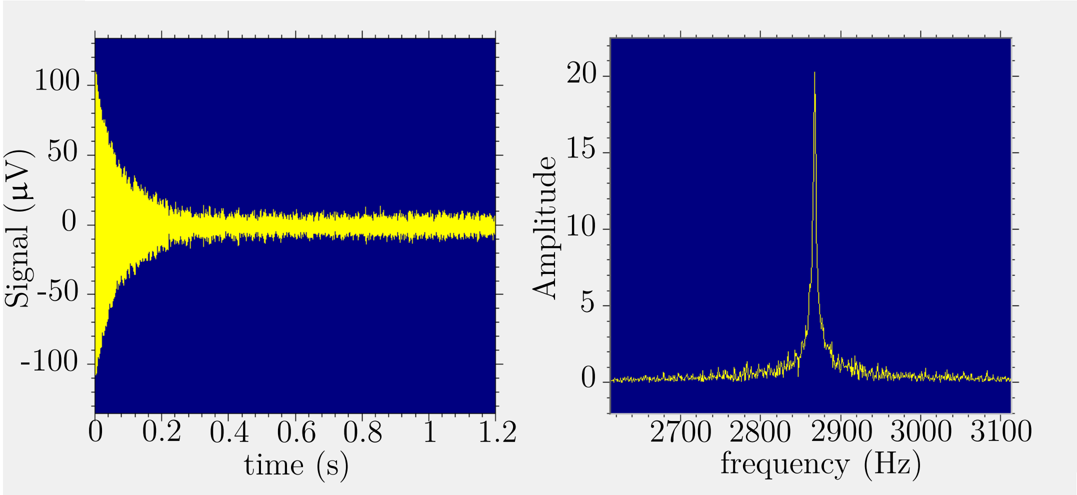

Figure 5.5: Free induction decay signal of water using the Terranova pulse-collect experiment in the anechoic chamber with shimming.

The homogeneity of the DC field is calculated using the spin-spin relaxation times, as shown in the following equation

$$\frac{\Delta B}{B_0} = \frac{1}{\gamma B_0}\left(\frac{1}{\tau_2^*} - \frac{1}{\tau_2}\right), \tag{108}$$

which is simplified using the Larmor expression as

$$\frac{\Delta B}{B_0} = \frac{1}{\omega_0}\left(\frac{1}{\tau_2^*} - \frac{1}{\tau_2}\right). \tag{109}$$

The DC coil system homogeneity results for both the shimmed and non-shimmed experiments, which is a feature of the Terranova system, are shown in Table 5.1.

Table 5.1: Coil system homogeneity results for shimmed and non-shimmed experiments.

Parameters	**Shimmed**	**Non-Shimmed**
Frequency (Hz)	2868	2860
τ_2^* (ms)	59	57
τ_2 (ms)	1760	1760
Homogeneity (ppm)	909	945

The results show that there are no major homogeneity differences between the shimmed and non-shimmed experiments. Of course, these results can be used to justify the absence of shim coils in the final experimental setup. A further justification for the absence of shim coils in the final setup is that the sample size used is 0.25 ml which is 2000 times smaller than the 500 ml water bottle used in the Terranova.

A filtered back projection and spin-echo image of a double, water filled, tube phantom are shown in Figure 5.6 and Figure 5.7 respectively.

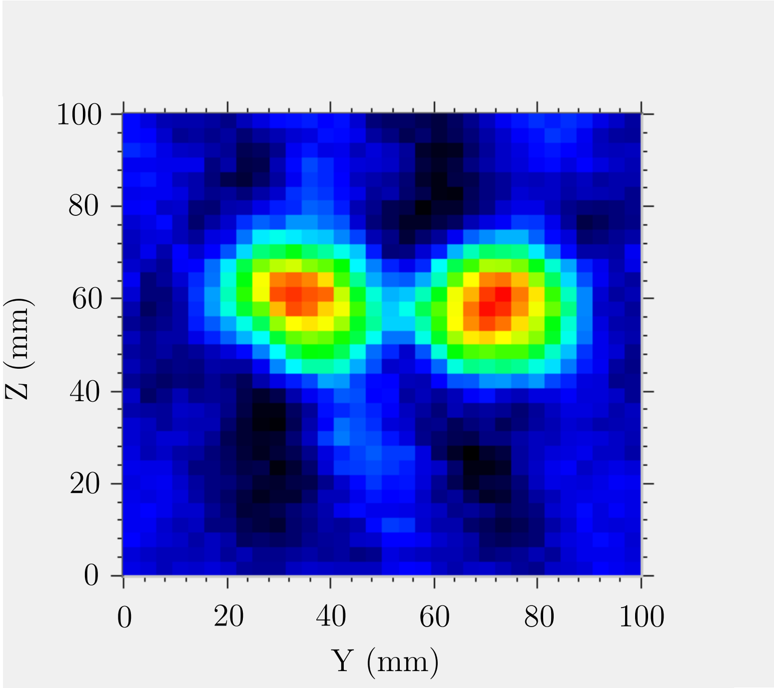

Figure 5.6: Filtered back projection image of the water filled two-tube phantom with shimming.

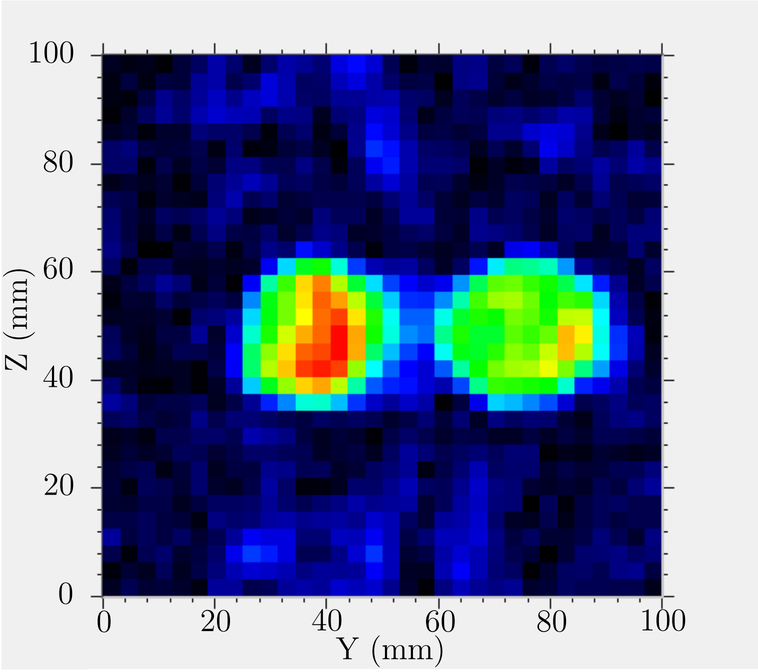

Figure 5.7: Spin-echo image of the water filled two-tube phantom with shimming.

The matrix size of the image is 32 with a field of view of 100 mm for each axis. A list of parameters used for image acquisition is shown in Table 5.2, with an acquisition time of approximately 15 minutes. The relatively good image quality indicates that the DC coil system is capable of replacing the Earth's magnetic field.

Table 5.2: Terranova parameters for the filtered back projection (FBP) and spin-echo (SE) imaging techniques.

Parameters	**FBP Image**	**SE Image**
Frequency (Hz)	2867	2867
Bandwidth (Hz)	64	64
Number of scans	6	8
Phase gradient duration (ms)	–	100
Pulse duration (ms)	5000	4500
Repetition time (s)	10	10
Phase cycle step	2	2
Completion time (min)	15	40

The DC coil system is therefore able to produce a homogeneous DC magnetic field, approximately 0.5 ppm in the small sample volume of 0.254 cm^3, which is comparable to the industrial standards for NMR and EPR experimentation [45].

5.3 Sample Properties & Losses

Theoretical and experimental evidence both suggest that the dielectric and inductive losses in a conductive sample cannot simply be ignored. A photograph of the sample container with the T1 optic thermometer is shown in Figure 5.8.

Figure 5.8: Photograph of the sample-container with a T1 optic thermometer placed inside.

5.3.1 Dielectric loss

The dielectric loss is due to the electric lines of force passing through the sample as a result of distributed capacitance in the resonator [46]. To distinguish the dielectric loss from the inductive loss, the total electric field $\mathbf{E}_i$ is given by

$$\mathbf{E}_t = -\nabla V - \frac{\partial \mathbf{A}}{\partial t} = \mathbf{E}_c + \mathbf{E}_i, \tag{110}$$

where $\mathbf{A}$ is the magnetic vector potential, V the electric scalar potential, $\mathbf{E}_c$ is the conservative field component and $\mathbf{E}_i$ the induced non-conservative field component [47]. The effect of $\mathbf{E}_i$ is given in the following section. The dielectric loss effect of $\mathbf{E}_c$ is modelled as a resistor R_c [19], and is given by

$$R_c = \tau \omega^3 L^2 C_d, \tag{111}$$

where τ is the power factor of the distributed capacity, ω_0 the resonant angular frequency, L the resonator inductance and C_d the distributed capacitance. It is interesting to note that the distributed capacitance has unity exponent compared to the inductance and resonant frequency.

Shielding

The dielectric loss effects can be minimised using a copper foil shield placed alongside the slot in the resonator, as first demonstrated by Ono et al [48]. The copper foil acts to distribute the electric field lines closer to the slot and less so through the sample. The adapted drawing of Ono's patented design is shown in Figure 5.9.

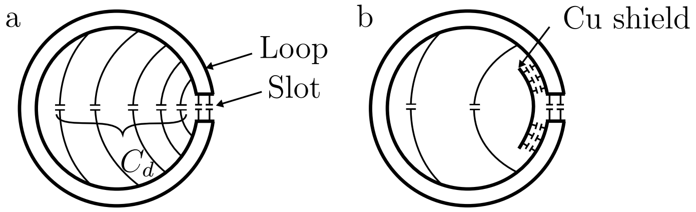

Figure 5.9: Effect of copper foil shielding used in a loop-gap resonator. a) no shield, b) with shield. Adapted from Ono [48].

The second type of shielding involves using copper wires attached to the sample container circumferentially, which in effect creates a Faraday shield, as shown in Figures 5.10 and 5.11. It is suggested by the research of Park et al [47], that eight copper strips can reduce sample heating by 88 % for 0.2 $\mathrm{S \cdot m^{-1}}$ conductive samples.

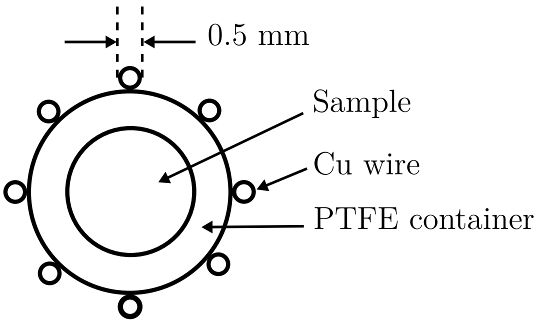

Figure 5.10: Copper wire used as shielding around sample.

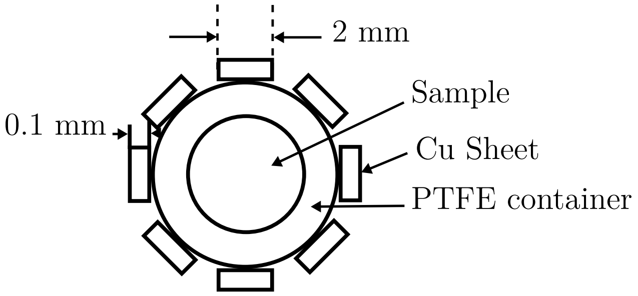

Figure 5.11: Copper sheets used as shielding around sample.

5.3.2 Inductive loss

Following the model by Hoult and Lauterbur [19], the inductive losses of a conductive sample in a spherical volume can be derived, as shown in Figure 5.12.

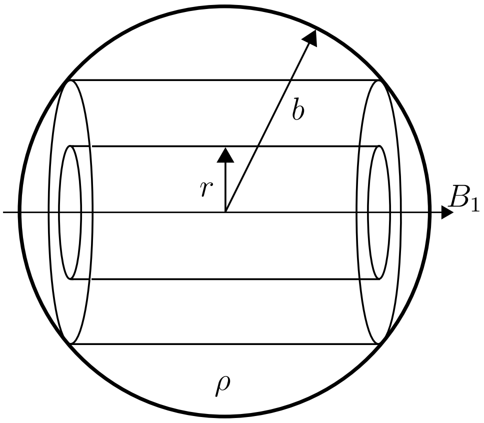

Figure 5.12: Spherical model used to derive inductive losses in a conductive sample, adapted from Hoult [19].

The elemental conductance dG is given by

$$dG = \frac{(b^2 - r^2)\, dr}{\pi r \rho}, \tag{112}$$

where ρ is the specific resistivity of the sample. The induced electromotive force (EMF) V is given by

$$V = -2\pi r^2 \frac{\partial B_1}{\partial t} = 2\pi r^2 \omega_0 B_1 \sin(\omega_0 t)\,. \tag{113}$$

It must be noted that the magnetic field B_1 is half the total magnetic field due to linear polarisation of the RF resonator, hence the need for the factor 2 in Equation 113. The time average of the voltage squared multiplied by the elemental conductance is integrated for r ranging from 0 to b, with the resulting average power W given by

$$W = \frac{4\pi \omega_0^2 B_1^2 b^5}{15\rho}. \tag{114}$$

Using the non-optimal values in Table 3.1, a sample conductivity of $0.1\ \mathrm{S \cdot m^{-1}}$ and a radius $b = 3.93$ mm, chosen such that the net sample volume is 0.254 ml, the calculated value for the temperature rise due to inductive loss is

$$\frac{dT}{dt} = 4.08\ {}^\circ\mathrm{C \cdot s^{-1}}. \tag{115}$$

The induction loss is significant, as it is 30 % of the predicted loss due to the electron spin resonant effect calculated in Section 3.1.4. The sample used in the experiment is in fact cylindrical as shown with its dimensions in Figure 5.13,

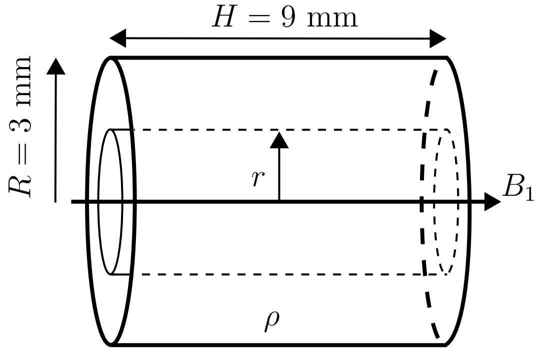

Figure 5.13: Cylindrical model used to calculate induction loss in experimental setup.

The elemental conductance of the cylindrical model is given by

$$dG = \frac{Hdr}{2\pi r\rho}, \tag{116}$$

which leads to the average power of

$$W = \frac{H\pi\omega_0^2 B_1^2 R^4}{4\rho}, \tag{117}$$

using the parameter values in Figure 5.13 and a conductivity of 0.1 $\mathrm{S \cdot m^{-1}}$, the temperature gradient is calculated as

$$\frac{dT}{dt} = 3.00\ °\mathrm{C \cdot s^{-1}}. \tag{118}$$

The inductive losses are smaller for a cylindrical container compared to a spherical container of equal volume. The calculations also illustrate the necessity of a reduced sample size, which results in an increased DC magnetic field homogeneity and a significant reduction of inductive loss.

The reduced inductive loss for a smaller sample size in effect lowers the thermal noise floor which is also beneficial for experimental measurements. The large inductive loss is of clinical concern, however the inductive loss could be reduced if a lower rms (i.e. pulsed waveform) B_1 source is used at the optimal spin-power resonance frequency and τ_{1e} value.

6 EXPERIMENTAL RESULTS

The sample and container conductivity properties are characterised. The thermal drift of the sample without a DC field and constant input RF power is measured. The heating measurements due to electron paramagnetic resonance of the six substances are displayed. A statistical and model analysis of the data is performed.

6.1 Electrical Conductivity

The electrical conductivity of the various liquid substances was measured using the $ECTestr11+$ from EUTECH instruments [49]. The results of the DC conductivity measurements are shown in Table 6.1. The literature results, abbreviated as Lit. in Table 6.1, from Ogunlade are used for comparative purposes [39].

Table 6.1: Electrical conductivities of the liquid test substances, with MRI contrast agents at 0.5 M vial concentration.

Substance	**Temp. (°C)**	**Meas.** $\boldsymbol{\sigma_c}$ **(**$\mathbf{S \cdot m^{-1}}$**)**	**Lit.** [39] $\boldsymbol{\sigma_c}$ **(**$\mathbf{S \cdot m^{-1}}$**)**
Distilled Water	21.3	0.78×10^{-3}	0.2×10^{-3}
Saline	21.2	1.453	1.4100
MultiHance	21.8	0.401	–
Magnevist	21.9	0.607	0.568
Dotarem	21.8	0.431	0.435
ProHance	21.2	0.0483	0.0504

The electrical conductivity proves to be a critical parameter in experimentation as a sample with higher conductivity, with all other parameters set equal, shows a greater increase in temperature due to eddy-current losses. The eddy-currents in the liquid also shield the nutation field B_1 to some degree.

The combined result is that the sample has less thermodynamic stability (i.e. the container is likely to rupture and increase Gd-ligand dissociation), with the rf power absorbed by the spins greatly reduced. The signal-to-noise ratio is effectively reduced and the measurement of the temperature change which is due entirely to the investigated phenomena, becomes challenging.

6.2 Comparison of Shielded & Unshielded Samples

The consequences of electrical field shielding using copper strips attached to the PTFE sample tube is demonstrated via experiment. The results in Table 6.2 show the temperature rates for the various substances with each substance averaged over five 30 second tests.

Table 6.2: Shielding effect of copper strips attached to PTFE sample tube.

Sample	**Container**	**f (MHz)**	**Thermal Response ($^\circ\mathrm{C} \cdot \mathrm{s}^{-1} \cdot \mathrm{W}^{-1}$)**
Air	Unshielded	861.24	0.0058
	Shielded	860.69	0.0798
Water	Unshielded	856.94	0.023
	Shielded	855.88	0.130
Saline	Unshielded	856.34	0.336
	Shielded	860.36	0.331
MultiHance	Unshielded	857.64	0.281
	Shielded	859.46	0.203
Magnevist	Unshielded	857.14	0.236
	Shielded	859.06	0.258
ProHance	Unshielded	857.26	0.128
	Shielded	859.11	0.199
Dotarem	Unshielded	855.50	0.253
	Shielded	859.50	0.274

The thermal response represents the temperature rate due to a rf step input with an average duration of 30 seconds. The temperature rate is normalised with respect to the rf input power ($^\circ\mathrm{C} \cdot \mathrm{s}^{-1} \cdot \mathrm{W}^{-1}$), which enables a comparison between the different experimental results.

As shown in Table 6.2 the tested substances are not shielded effectively by the copper strips, and in some cases the shielded substances performed poorly compared to the unshielded samples. Given that the sample container length is comparable to the resonator depth a possible mechanism which explains the findings in Table 6.2 is fringing which couples to the copper strips on the sample. Based on these results the unshielded PTFE capsule is used for the substances in the final experimental design.

It is interesting to note that the 'shielded' capsule has an inverse effect for the lower conductive liquids such as Water and ProHance. The tabulated results illustrate that shielding the sample container inside of a loop-gap resonator is more subtle and complex than the suggestions made by Park et al [47].

6.3 Thermal Drift

The thermal response of the substance in the loop-gap resonator with a constant rf input, and without a DC magnetic field, is recorded in order to understand the thermal deviations of that substance. The results illustrate that the temperature of each substance in the loop-gap resonator drifts under constant input power conditions, as shown in Figure 6.1. The absolute average thermal drift ranges from $0.8 - 1.7\ \text{m}^\circ\text{C} \cdot \text{s}^{-1}$.

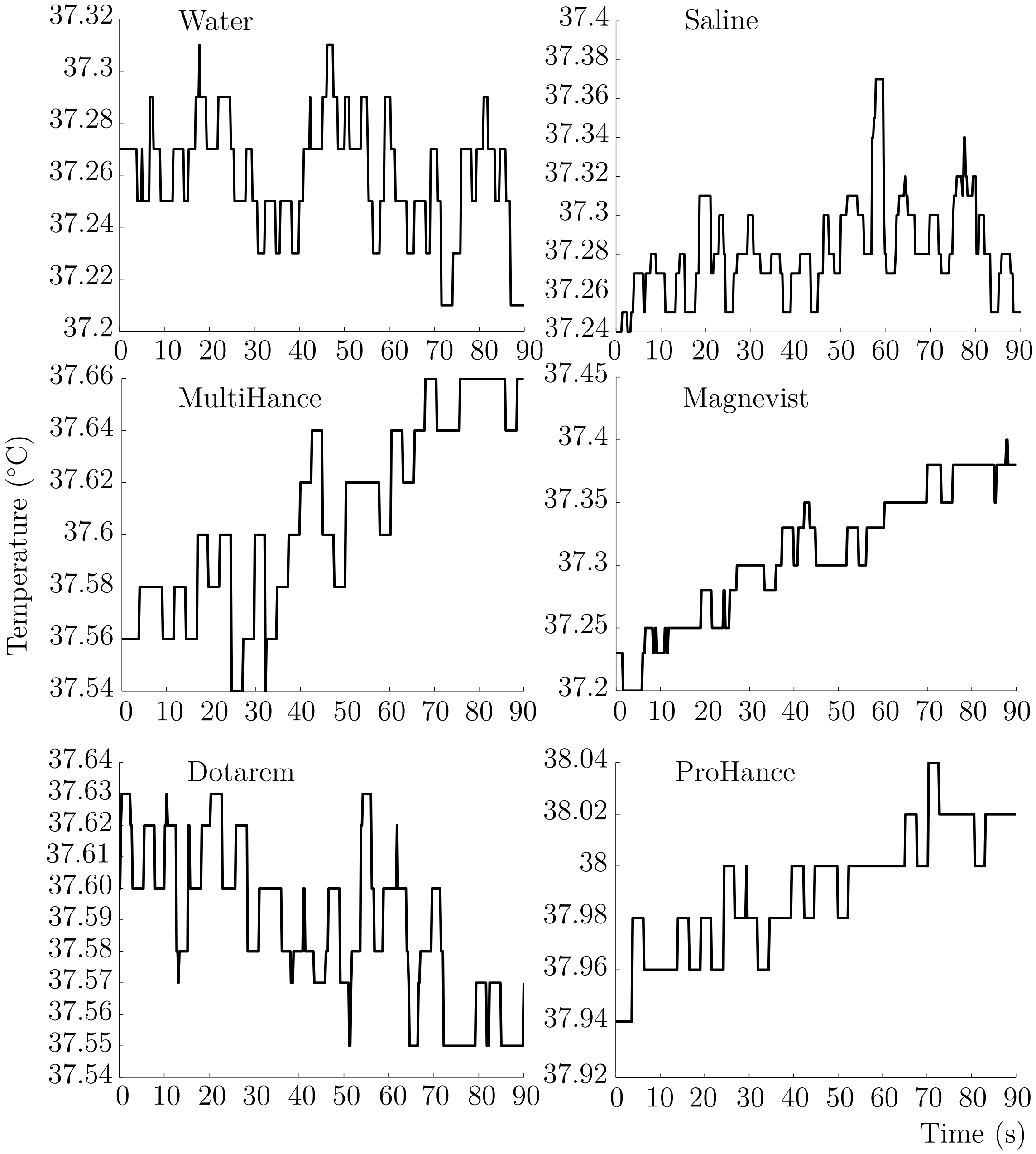

Figure 6.1: Thermal drift of the substances averaged over five measurements recorded during the DC-Off interval.

The ambient temperature of the anechoic chamber was recorded before and after each experiment, with an average experiment recording of 18 minutes. The ambient temperature of the anechoic chamber, due to the heating of the DC coil system, did not increase by more than $1 - 2$ °C. Initially, before each experiment recording started, the sample was driven to approximately 37 °C and the temperature fluctuations maintained within the 0.1 °C resolution of the fibre optic thermometer. The initialisation procedure insured that an approximate steady-state was achieved prior to recording. Multiple repeated measurements were carried out in order to improve the signal-to-noise ratio.

6.4 Spin Resonance Heating Results

The thermal-response of a substance due to the interaction with the DC magnetic field, the rf loop-gap resonator and the spin-resonance phenomenon was investigated. It was found during testing that the capsule was not thermally stable at temperatures above 50 °C as the capsule would leak and display an increase in thermal drift.

Given the undesirable thermal behaviour of the sample and capsule at high temperatures the experiments were performed at a lower temperature, approximately 37 °C. The steady-state temperature of 37 °C is approximately the human-core temperature and the operating temperature of the tested contrast agents. A negative consequence however of this relatively lower steady-state temperature is the reduced rf power injected into the sample, which significantly reduces the investigated spin-resonance heating effect.

Each experiment involved ten, ninety second interval, measurements during which the rf power was supplied continuously and the DC-field switched on or off for five of those measurements. The procedure is listed as:

1. Switch on signal generator,
2. Raise sample temperature to steady-state value (≈ 37 °C),
3. Monitor transmitted power of amplifier,
4. Switch DC coil on and record for 90 s,
5. Monitor transmitted power of amplifier,
6. Switch DC coil off and record for 90 s,
7. 30 s delay to achieve approximate steady-state,
8. Repeat measurements from step 3.

It was anticipated that the sample would heat faster for the five DC-On recorded conditions and slower for the other five DC-Off recorded conditions. The approximate steady-state temperature of the samples was 37 ± 2 °C with the final results normalised to zero-offset. The normalisation process allows for the temperature change comparison between substances and conditions. The zero-offset is obtained by subtracting the initial average temperature across each condition.

The results for the six substances are shown in Figure 6.2, where the red-lines represent the DC-Off condition average measurements and the blue-lines the DC-On condition average measurements.

The small sample of results in Figure 6.2 show that ProHance and Dotarem already respond with a measurable difference in heating during the DC-On interval as opposed to the DC-Off interval. All the substances were further measured and investigated in order to reduce noise and statistically verify a reproducible phenomena.

In order to increase the signal-to-noise ratio an additional twenty five measurements were performed. A thirty sample average of the temperature responses for the six substances, with linear regression lines fitted, is shown in Figure 6.3. A control experiment for Dotarem and ProHance was performed by connecting the bottom four coils of the DC magnetic coil system in opposite direction to the upper four coils.

The reversed connection results in the same total coil current, and therefore heating of the coil, but with an approximately zero magnetic field over the sample volume. The control experiment therefore tests if the sample absorbs any heat emitted by the DC coil system.

If the thermal drift discussed in section 6.3 is stochastic in nature then a further twenty-five measurements should reduce the drift, for example ProHance should be reduced by $1.11\ \mathrm{m^\circ C \cdot s^{-1}} \div \sqrt{25} = 0.222\ \mathrm{m^\circ C \cdot s^{-1}}$. A reduced thermal drift for the additional twenty-five control ProHance experiments, as shown in Figure 6.3, is approximately the same as the predicted value. The measured reduction in variance therefore suggests that the assumption of independence is valid, the thermal drift is stochastic and that the precision of the results can be improved.

It is interesting to note that, except for the control substances, there exists a non-zero slope for the DC-Off condition. A possible reason for this residual effect is likely due to the switch delay of approximately $6 - 12$ s, which is due to the inductance of the DC coil system and data processing time. The spin system is therefore partially excited during the recorded DC-Off interval. Future refinement of the experimental procedure is therefore necessary to eliminate this residual effect.

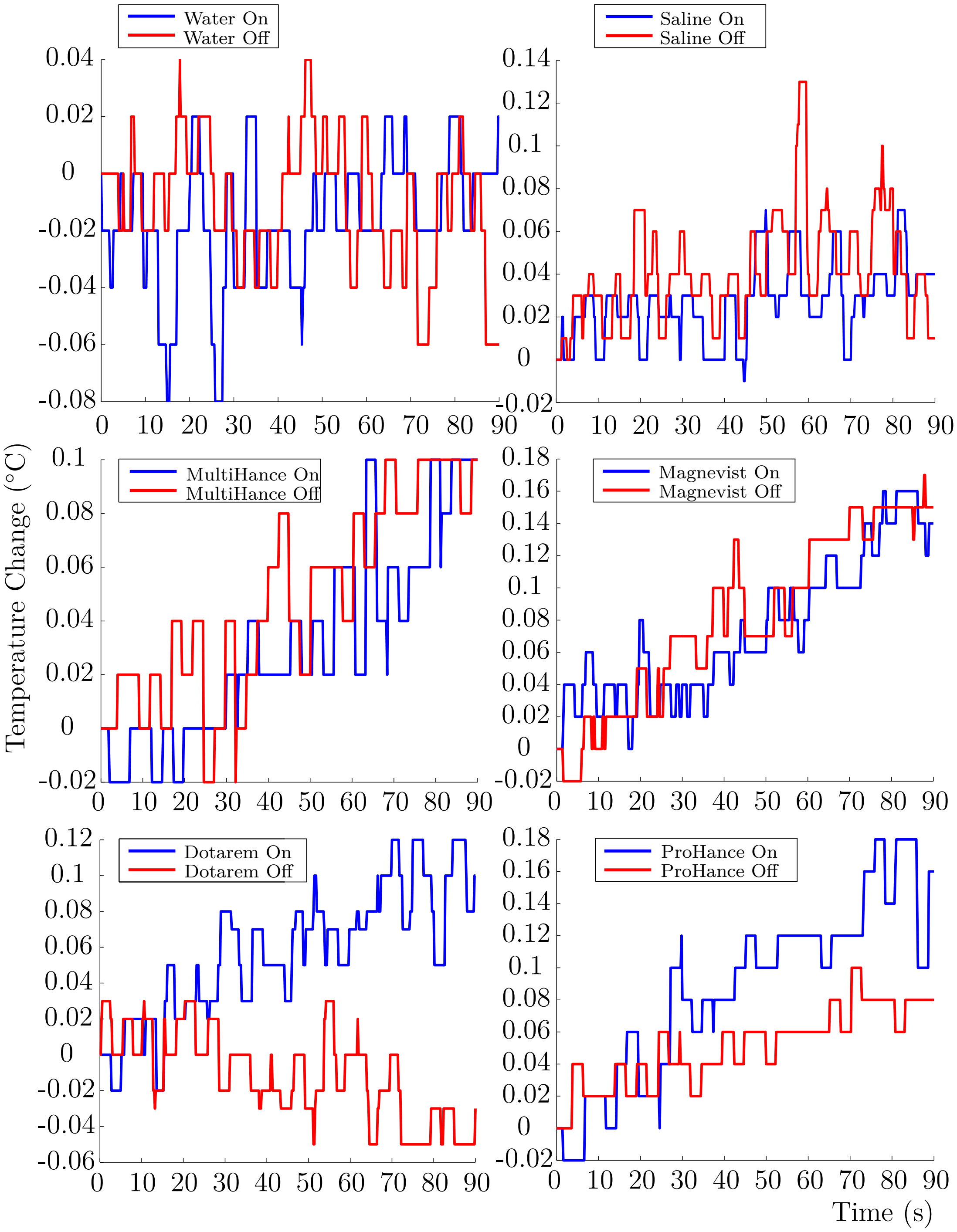

Figure 6.2: Zero-offset adjusted temperature results averaged over five measurements, with DC-On (blue) and DC-Off (red).

It is seen from the control experiment results for Dotarem and ProHance that there are no significant differences in temperature rates for when the DC-field state is switched.

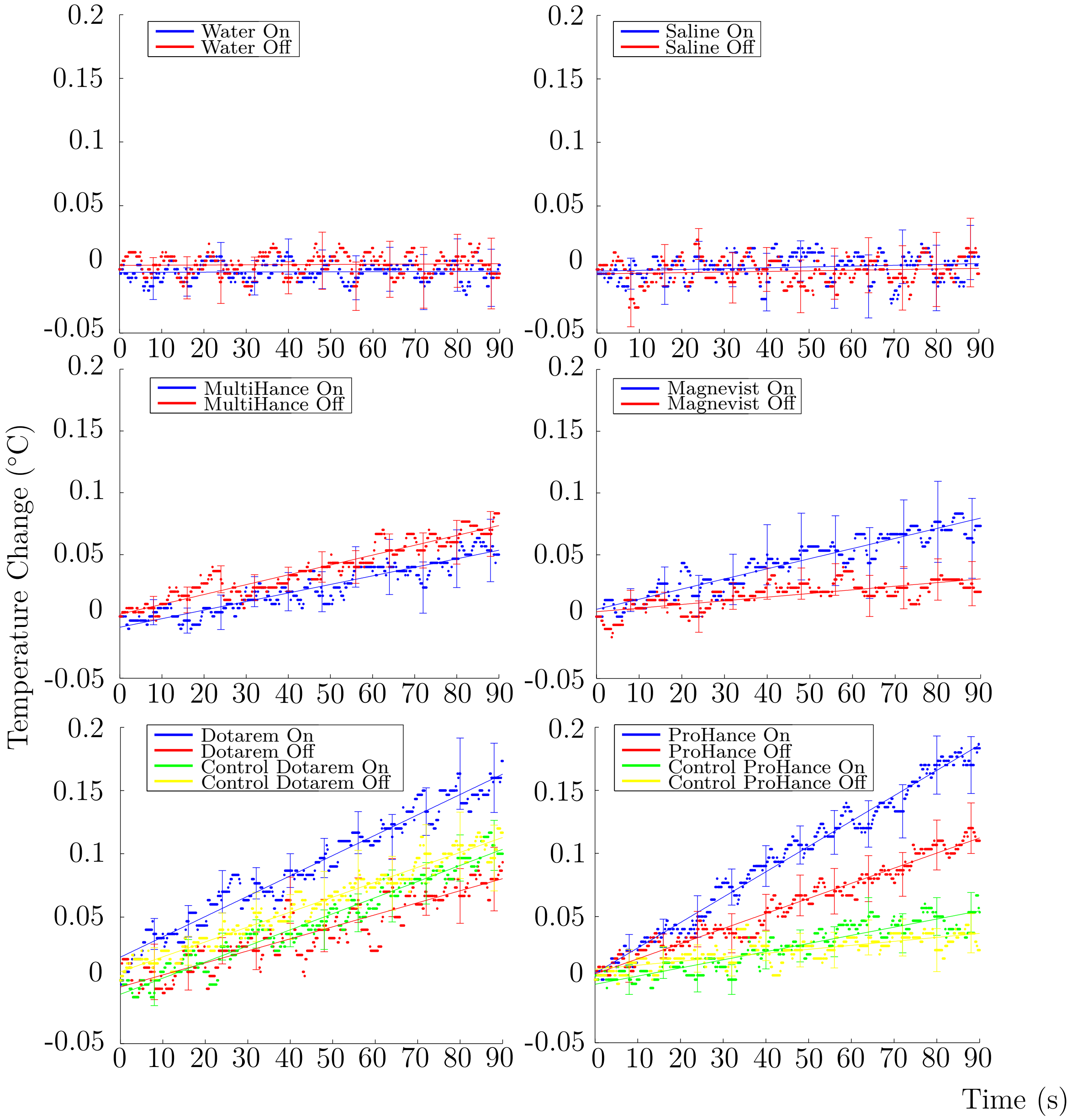

Figure 6.3: Average temperature rise over a ninety second interval for the six tested substances, with each mean value obtained over thirty experiments and standard error bars shown at every 8 s.

The means and standard errors of the four tested contrast agents are shown in Figure 6.4. It is noted from Figure 6.4 that the error bars of the contrast agents overlap at a few sample points. A statistical and descriptive analysis is performed in order to quantify the amount of separation that exists between each substance.

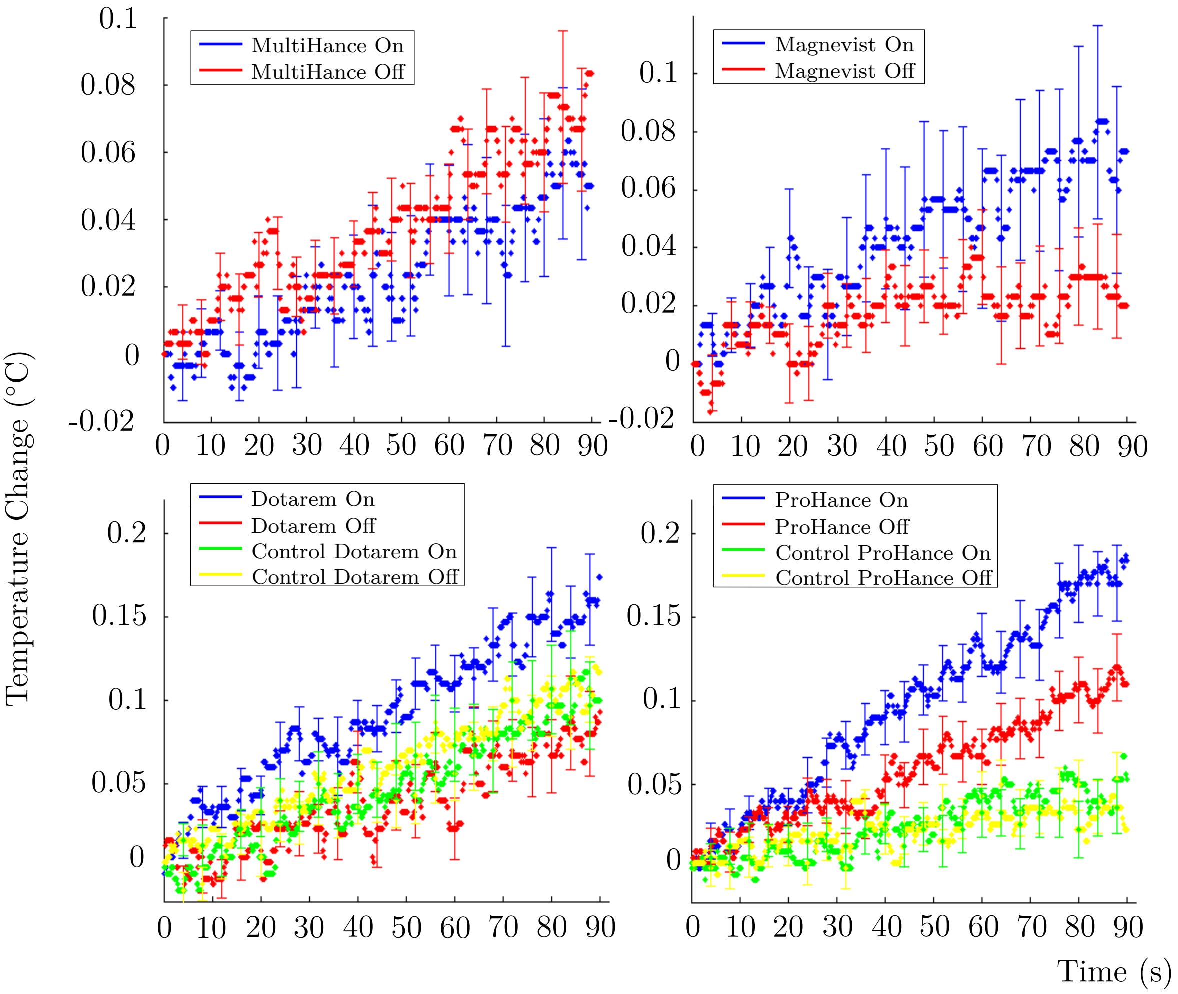

Figure 6.4: Magnified view of thirty sample average of the contrast agent data with a standard error bar shown at every 4 s.

6.4.1 Regression analysis

Given that the temperature rate is small, as predicted by the theory for a small τ_{1e} value, a first-order polynomial regression model is fitted to the data, as shown in Figure 6.3 for each substance and condition, with the linear model given by

$$y = c + bx + \varepsilon, \tag{119}$$

where c is the intercept, b the slope and ε the error term associated with the model [50]. The error term quantifies the measurement device noise, human reproducibility, fluctuations in environmental conditions, substance variability, etc. The classical unweighted least-squares method is used to determine the parameters of the regression model.

The residual variance, which is also known as the squared standard regression error, is denoted $s^2_{y/x}$. Two sets of data, each with sample size n_1 and n_2, can be compared using their linear regression slopes (b_1, b_2) and their associated error.

The slope comparison of two regression lines tests the null hypothesis $H_0 : b_1 = b_2$, and is calculated using the Student's t-test statistic [50]. The t-test statistic follows a $t_{n1+n2-4}$ distribution, and is given by

$$t = \frac{b_1 - b_2}{\sqrt{s^2_{(y/x),pool}\left(\frac{1}{\Sigma\left(x_{i,1} - \bar{x}_1\right)^2} + \frac{1}{\Sigma\left(x_{i,2} - \bar{x}_2\right)^2}\right)}}, \tag{120}$$

with

$$s^2_{(y/x),pool} = \frac{(n_1 - 2)\, s^2_{(y/x)1} + (n_2 - 2)\, s^2_{(y/x)2}}{n_1 + n_2 - 4} \tag{121}$$

The slope values for the linear regression models and the p-value results of the comparison of slopes, between the two different states, are shown in Table 6.3. The sample size for each dataset is $n_1 = n_2 = 451$, which is a result of the 0.2 s sampling time of the fibre-optic thermometer. The regression results show that the slopes are statistically the same for the control substances, water and saline.

Table 6.3: Slope values b, with subscript definitions 1 = On/cOn and 2 = Off/cOff states, and comparison results using the experimental data.

Substance	**Experiment**	b_1 **(µ°C · s^{-1})**	b_2 **(µ°C · s^{-1})**	**p-value**
Water	On-Off*	9	14	0.788
Saline	On-Off	66	48	0.475
MultiHance	On-Off	692	796	< 0.01
Magnevist	On-Off	820	295	< 0.01
Dotarem	On-Off	1607	951	< 0.01
	On-cOn†	1607	1273	< 0.01
	cOn-cOff	1273	1179	< 0.01
ProHance	On-Off	2011	1198	< 0.01
	On-cOn	2011	646	< 0.01
	cOn-cOff	646	315	< 0.01

---

[*] On: Current flows in same direction for both coils, Off: No current.

[†] cOn: Current flows in opposite direction for top and bottom coils, cOff: No current.

The results also indicate that the slopes are statistically different for the contrast agents and the control experiments for Dotarem and ProHance. Although ProHance is shown to be significantly different between the cOn-cOff states, the actual cOn state slope value is three times smaller compared to the On state slope value.

The significance obtained for the control on-off experiments is mainly due to the large number of samples, and therefore large degrees of freedom used in the comparison, as illustrated by the almost identical, yet significant, slope values of the Dotarem control results.

A qualitative interpretation of the slope values is that there exists reasonable separation, between the On and Off states, for Magnevist, Dotarem and ProHance. A descriptive analysis is therefore presented which quantifies the exact amount of separation between the substances and provides a suitable physical interpretation for the datasets.

6.4.2 Descriptive analysis

Multiple repeated experiments were performed in order to extract the signal from the noise. A signal-to-noise ratio between each condition is calculated by comparing the means using the independent sample t-test, as shown by the following

$$t = \frac{(\overline{x}_1 - \overline{x}_2) - (\mu_1 - \mu_2)}{s_{pool}\sqrt{\dfrac{1}{n_1} + \dfrac{1}{n_2}}}, \tag{122}$$

with

$$s_{pool}^2 = \frac{(n_1 - 1)\, s_1^2 + (n_2 - 1)\, s_2^2}{n_1 + n_2 - 2} \tag{123}$$

where s_{pool} is the pooled sample standard deviation. In the presented case x_1 represents the DC field-On condition and x_2 the DC field-Off condition. The number of repeated measurements is $n_1 = n_2 = 30$ with the hypothesised difference in means given by $\mu_1 - \mu_2$. The tail for the t-test is right sided ($\mu_1 - \mu_2 > 0$) due to the expectation that the DC field on state would increase the temperature more so than the DC field off state. The control substances and control conditions are expected to show no increase in temperature for either DC field state.

It was discovered during experimentation that there exists a reasonable delay, $6 - 12$ s, between switching on the DC field and observing a temperature change. The switch time of the DC coil power supply, the inductance of the coils, the thermal properties of the sample-probe system and the data transmission time contribute to this delay.

As a consequence of this time delay the t-test is applied to the data after 30 s. The delay compensation also allows for the signal, if present, to rise above the measurement noise floor. It should be noted that the t-test does not evaluate the means across the entire time range of 90 s but rather the means are calculated at the time samples, every 0.2 s, for each condition. The assumption therefore of independent samples, which is usually tested using autocorrelation, is not necessary [51].

A 5 % significance level was selected for each independent t-test performed at a given time sample. The result of multiple independent t-tests is a collection of p-values. The average of the p-values is calculated over a total number of 301 sample points.

The averaging procedure of p-values is similar to that explained by Andrade [50]. The average p-value evaluates and quantifies the amount of separation in data between the different conditions, with the results of the average p-values shown in Table 6.4.

Table 6.4: Average p-values using the t-test with a 5 % significance level.

Substance	**Experiment**	**$\bar{\text{p}}$-value**
Water	On-Off	0.584
Saline	On-Off	0.437
MultiHance	On-Off	0.277
Magnevist	On-Off	0.173
Dotarem	On-Off	0.0325
	On-cOn	0.0414
	cOn-cOff	0.671
ProHance	On-Off	0.0297
	On-cOn	0.000751
	cOn-cOff	0.372

The results in Table 6.4 show that ProHance is significantly different, with relatively low p-values ($p < 0.05$), between the treatment-on and treatment-off conditions, as well as between the treatment-on and control-on condition. The thermal responses however of MultiHance and Magnevist are significantly smaller in magnitude, which results in higher p-values ($p > 0.1$) compared to Dotarem and ProHance. The difference in thermal response is most likely due to their linear molecular arrangement leading to a shorter τ_{1e} and hence inefficient spin-power properties.

The p-value for Magnevist is high ($p > 0.1$), although the means appear to be separated, the resulting p-value is a consequence of the relatively wide-spread of values about the mean. The relatively small temperature change, 0.1 °C over 90 s, of MultiHance and Magnevist excludes the substances from a further detailed system model analysis. The results also show, as expected, that the control substances, water and saline, fail to reject the null hypothesis.

6.4.3 Model analysis

It is noted from the regression analysis results that the net temperature rate for Dotarem and ProHance, obtained from the difference in slope values of the linear regression model for the treatment DC-On and control DC-On, is 334.1×10^{-6} $°\mathrm{C} \cdot \mathrm{s}^{-1}$ and $1,364 \times 10^{-6}$ $°\mathrm{C} \cdot \mathrm{s}^{-1}$ respectively. The experimental temperature rates are significantly lower than the theoretical prediction of 1.8 $°\mathrm{C} \cdot \mathrm{s}^{-1}$, which is obtained from Eq. (67) when using similar parameters to experimentation i.e. $B_1 = 0.54$ mT and $f = 857$ MHz.

As a result of this discrepancy, between theoretical and experimental values of the spin-lattice relaxation time, further modelling under these specific conditions is performed in order to estimate the value correctly. A thermal model, adapted from section 4.5.3, of the sample, sample tube and fibre-optic probe system is given by

$$\dot{Q}_a = \dot{Q}_l + \dot{Q}_s - \frac{T_w - T_a}{R_c + R_a} - \frac{T_w - T_t}{R_t}, \tag{124}$$

$$\dot{Q}_t = \frac{T_w - T_t}{R_t} - \frac{T_t - T_p}{R_p}, \tag{125}$$

$$\dot{Q}_p = \frac{T_t - T_p}{R_p}, \tag{126}$$

where $\dot{Q}_a$ is the net-thermal power in the contrast agent, $\dot{Q}_l$ is the liquid Ohmic-power loss, $\dot{Q}_s$ is the spin-power, T_w is the temperature of water, T_a is the ambient temperature, R is the thermal resistance (subscript a-1 mm air sleeve, c-PTFE sample container, t-PTFE outer fibre optic probe coating and p-polyimide inner fibre optic probe coating). The constant model parameters, other than the specific heat, were determined using a rf pulse-response for water, since water has a well-known specific heat value.

The specific heat capacity of each contrast agent is then estimated, as performed in section 4.5.3, using the average of the model parameters for a rf pulse-response and a negative-edge (on-off) step-response, an example of which is shown for ProHance in Figure 6.5.

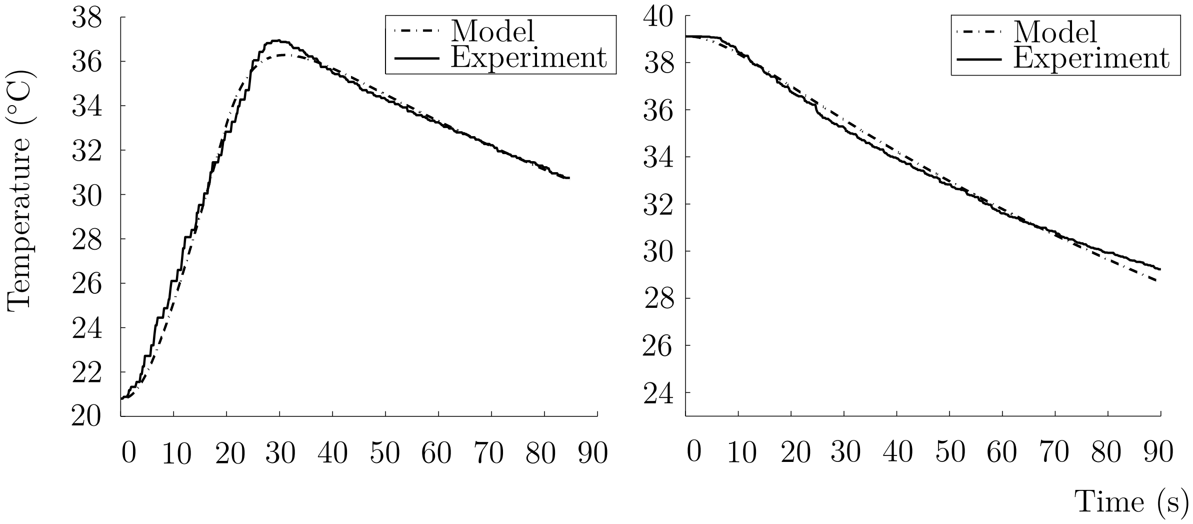

Figure 6.5: Experimental and model estimate for the specific heat capacity of ProHance using the average of the pulse (C_Δ) and decay (C_d) response.

The minimum of the normalised root-mean-square error (NRMSE) is used to determine the best model estimate of the specific heat capacity value for each response, as shown in Table 6.5.

Table 6.5: Specific heat capacity of Dotarem and ProHance using pulse and decay modelled data.

Substance	C_Δ	**NRMSE (%)**	C_d	**NRMSE (%)**	$\bar{C}$ $(\mathbf{J \cdot g^{-1} \cdot K^{-1}})$
Dotarem	1.78	1.67	2.72	2.95	2.25
ProHance	2.1	2.52	2.36	2.57	2.23

Using the estimated parameters of the container and substances, the Ohmic-loss and spin-power are estimated for the treatment-on and control-on conditions for Dotarem and ProHance, with the model fits shown in Figure 6.6.

The heating rates were adjusted in order to minimise the normalised root-mean-square error, with the results shown in Table 6.6. The spin-lattice relaxation time τ_{1e} is estimated from the model of spin-power heating rates, experimental values for B_1 and Eq. (65), with the results shown in Table 6.6.

Table 6.6: Model estimate of total-power, Ohmic loss, spin-power and spin-lattice relaxation time τ_{1e} for Dotarem and ProHance.

Substance	$\dot{Q}_T$ **(W)**	**Err. (%)**	$\dot{Q}_l$ **(W)**	**Err. (%)**	$\dot{Q}_s$ **(W)**	τ_{1e} **(ps)**
Dotarem	0.1135	8.18	0.1081	7.36	0.005375	0.26
ProHance	0.1076	4.56	0.1032	9.97	0.004400	0.15

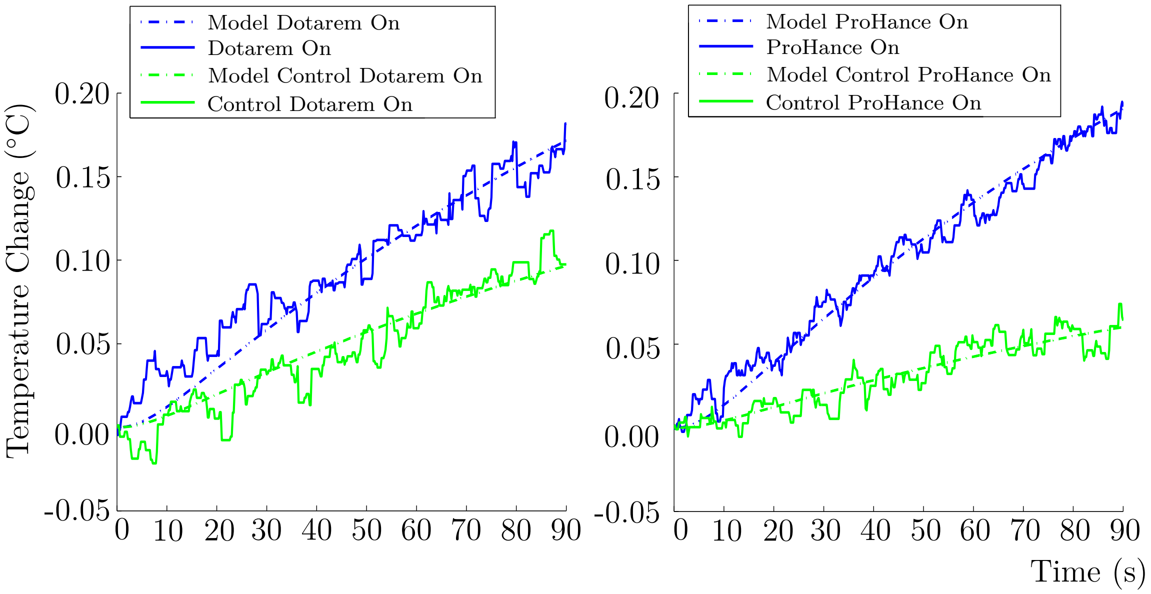

Figure 6.6: Model estimates for Dotarem and ProHance treatment-control condition responses.

It is noted from Table 6.6 that the estimated relaxation times are approximately three orders of magnitude smaller than the theoretical estimate of 0.1 ns. A reason for the discrepancy is most likely due to the high concentration effects which increase the dipole-dipole relaxation processes.

Another possible reason for the discrepancy is the fast molecular tumbling rates and the low resonant Larmor frequency, which significantly decreases the electronic spin-relaxation time [52]. The $300-500$ ps rotational and $1-2$ ps vibrational correlation times tend to broaden the spectral density function which enhances the relaxation processes [53]. The spin-relaxation parameters are also not well-known in the low-frequency ranges at relatively high temperatures.

The experiment therefore provides an alternative procedure for measuring the spin-relaxation time. Under similar experimental conditions a molecule with a slower spin-lattice relaxation time would result in larger spin-power and temperature rates.

In the current operating region the spin-power effect is approximately linear against relaxation time, as seen from Eq. 65 for $\tau_{1e,2e} \ll 0.1$ ns. The consequence of this linearity is that an order of magnitude increase in τ_{1e} will result in an order of magnitude increase in spin-power.

6.5 Summary of Results

The six substances were tested in a 0.254 ml unshielded PTFE capsule. The initial thermal drift after 5 measurments was measured at approximately 1.11 $\mathrm{m°C \cdot s^{-1}}$ for ProHance and after an additional 25 measurements was averaged to 0.222 $\mathrm{m°C \cdot s^{-1}}$. Dotarem and ProHance showed the most significant temperature increase to electron spin resonance heating.

The statistical analysis illustrates that the lack of DC on-off separation for the control substances is statistically significant. The apparent statistical significance of the DC on-off separation for the Dotarem and ProHance control experiments is due to the large number of data points used in the analysis.

The model analysis of the Dotarem and ProHance results show that a spin-power of $4-5$ mW is necessary in order to achieve the observed heating rate. Using this spin-power value, it is estimated that the spin-lattice relaxation time is three orders-of-magnitude smaller than the theoretical presented value of 0.1 ns.

A reason for this discrepancy is that the spin-relaxation parameters are generally not well known at frequencies below 9 GHz. Assuming the theoretical value is accurate, then the causes of the observed increase in relaxation processes could be due to the fast vibrational correlation times and high solution concentrations which both increase the dipole-dipole interactions.

Although the observed heating rate is much smaller than the calculated value, the rate it is still 167 000 times larger than the temperature rate calculated using protons. The results therefore suggest that this effect is real and measurable, and can be further increased by using a substance with a longer spin-lattice relaxation time τ_{1e}.

7 CONCLUSION

A summary of the research findings and results, obtained from both theory and experimentation, is presented. A discussion on the mechanisms and reasons behind the research results is provided. Recommendations for future work, and use of other potential hyperthermia agents are detailed.

7.1 Overview

The use of paramagnetic gadolinium-based contrast agents as possible hyperthermia agents is explored in the thesis. The literature shows that many different types of hyperthermia agents and techniques have been explored as cancer hyperthermia treatments. Non-invasive modalities, such as high-intensity focused ultrasound, show a promising alternative to current surgical procedures and treatments of neoplasms. The use of magnetic resonance as a potential hyperthermia technique or clinical modality has been explored both theoretically and experimentally in this research.

The first step however in achieving a viable hyperthermia agent is to test whether or not the agent, in this case a gadolinium-based contrast agent, can absorb thermal energy and produce a measurable temperature rise. The experimental design and setup enables the testing of this initial phase. The relatively simple loop-gap resonator and spherical DC coil array allowed for the hypothesis to be tested.

The sample container was modelled and selected based on the dielectric and inductive losses. The fibre optic thermometer allowed for the measurement of the sample temperature without any electromagnetic interference when placed inside the resonator. The calibration, characterisation and testing of equipment ensured the results would be measured precisely.

The six substances (four contrast agents and two control liquids) were investigated using the experimental apparatus. Experimental results of the loop-gap resonator, sample-tube and the DC coils helped to verify the simulations.

The six substances were tested experimentally using a pulsed signal (step-on and step-off) in order to characterise the thermal properties of the sample container. Using the theoretical model of spin-power together with the thermal properties of the sample-container, a comparison between the model and experimental results was made.

The need for a more effective material, by possible modification of current contrast agents, has become evident from this research. Substances that contain longer relaxation time parameters are likely to significantly increase the efficiency of spin resonance heating.

7.2 Discussion

The designed DC magnetic coil system is able to lift the energy level degeneracy of protons in a low-field nuclear magnetic resonance system with satisfactory results, confirming its suitability in the experimental setup. The magnetic field of the loop-gap resonator is measured indirectly by observing the SAR of the six substances and then compared to the finite-element model. The thermal properties and behaviours of the six substance were accurately modelled.

The thermal characteristics of the six substances as measured in the loop-gap resonator with constant RF input power, and without an applied DC magnetic field, displayed a random thermal drift component. The precise reason for the thermal drift behaviour of the contrast agents is unclear, but may be caused by the fluctuating temperature of the substance which in turn affects the resonance frequency of the loop-gap resonator. The DC field tests illustrate that only two out of the four contrast agent substances have a measurable effect due to the spin-resonance heating phenomenon.

The spin-lattice relaxation time is not well-known in the literature for the experimental conditions used. It is seen from the literature that multiple parameters affect the spin-lattice relaxation time of gadolinium-based contrast agents. The theoretical model and predictions were based on an estimate of τ_{1e}, by extrapolation of the results of models developed previously. The experimental results described in this thesis show that in the low-frequency domain and using high substance concentration, the spin-relaxation time in contrast agents is much smaller than originally estimated.

The thermal power generated by spin-resonance relaxation in Dotarem and ProHance was found to be relatively small, in the range of mW. However a temperature rise was measured and verified statistically through multiple repeated treatment and control experiments. The main result or conclusion based on this research is that the spin-relaxation time plays a significant role in determining the efficiency in spin-resonance heating.

7.3 Future Work

In order to improve this technology, and to amplify or enhance this effect, a different molecule is required. The use of carbon nanotubes is a popular approach to hyperthermia treatment [54]. In order to slow down the relaxation process, a more rigid molecular structure to attach the gadolinium ions is hypothesised. Increasing the electron spin-relaxation time of gadolinium ions by attaching them to ultra-short carbon nanotubes could be a possible solution. The increased spin-lattice relaxation time would increase the spin-power properties of the substance significantly.

7.3.1 Gadonanotubes

Gadonanotubes have been shown to be 100 times more efficient contrast agents compared to current clinical contrast agents [55]. Gadonanotubes are composed of ultra-short carbon nanotubes, which were shown to be best suited for cellular uptake [55]. The aquated gadolinium ions form clusters within the framework of the nanotubes. Studies have revealed that the gadonanotubes act as superparamagnetic molecular magnets [56].

The applications of gadonanotubes are many with the main focus being that of contrast imaging. Other applications include the use of gadonanotubes as guided-therapy probes [56]. The results of generating heat in gadonanotubes using conventional rf methods have shown a relatively small effect [54]. The use of superparamagnetic particles however is favoured as they have been shown to produce more heat at safer (lower) alternating magnetic fields compared to ferromagnetic materials [55].

It is hypothesised by the author that a more efficient thermal response can be generated using the electron paramagnetic resonance of the gadonanotubes. The stereochemical rigidity of the carbon nanotube framework together with the concentrated yet separated clusters of Gd^{3+} ions could lead to a more efficient transfer of spin-energy into the lattice.

7.3.2 Focusing spin-power

In order to achieve thermal ablation of tumour tissue, a significant amount of thermal energy needs to be deposited in the treatment region. The treatment region selection, using conventional MRI techniques [57, 58], is hypothesised as a possible modality. The increase in cellular uptake of the thermal agent, by attaching appropriate molecules such as antibodies, is another hypothesised modality in which the focusing of spin-power could be achieved.

REFERENCES

[1] A. Ko, M. Dollinger, and E. Rosenbaum. *Everyone's Guide to Cancer Therapy: How Cancer Is Diagnosed, Treated, and Managed Day to Day.* EVERYONE'S GUIDE TO CANCER THERAPY. Andrews McMeel Publishing, 2008.

[2] J. van der Zee. "Heating the patient: a promising approach?" *Annals of Oncology*, vol. 13, no. 8, pp. 1173–1184, 2002.

[3] T. Livraghi, L. Solbiati, M. F. Meloni, G. S. Gazelle, E. F. Halpern, and S. N. Goldberg. "Treatment of Focal Liver Tumors with Percutaneous Radio-frequency Ablation: Complications Encountered in a Multicenter Study." *Radiology*, vol. 226, no. 2, pp. 441–451, 2003.

[4] S. Laurent, S. Dutz, U. O. Häfeli, and M. Mahmoudi. "Magnetic fluid hyperthermia: focus on superparamagnetic iron oxide nanoparticles." *Advances in Colloid and Interface Science*, vol. 166, no. 1, pp. 8 – 23, 2011.

[5] J. G. Lynn, R. L. Zwemer, A. J. Chick, and A. E. Miller. "A new method for the generation and use of focused ultrasound in experimental biology." *The journal of general physiology*, vol. 26, no. 2, p. 179, 1942.

[6] J. Kennedy, G. Ter Haar, and D. Cranston. "High intensity focused ultrasound: surgery of the future?" *British Journal of Radiology*, vol. 76, no. 909, pp. 590 – 599, 2003.

[7] J. Weil and J. Bolton. *Electron Paramagnetic Resonance: Elementary Theory and Practical Applications*, pp. 305 – 362. Wiley, 2007.

[8] D. L. Parker. "Applications of NMR Imaging in Hyperthermia: An Evaluation of the Potential for Localized Tissue Heating and Noninvasive Temperature Monitoring." *Biomedical Engineering, IEEE Transactions on*, vol. BME-31, no. 1, pp. 161 – 167, 1984.

[9] A. H. Morrish. *The physical principles of magnetism*, pp. 57 – 133. Wiley series on the science and technology of materials. Wiley, 1965.

[10] K. Buschow and F. de Boer. *Physics of Magnetism and Magnetic Materials*, pp. 22 – 26. Focus on biotechnology. Springer US, 2007.

[11] X. Xiang and H. Yang. "Intracellular thermal ablation using nano-particle electron spin resonance heating.", Nov. 30 2006. URL `http://www.google.com/patents/US20060269612`. US Patent App. 11/410,512.

[12] A. Abragam and B. Bleaney. *Electron Paramagnetic Resonance of Transition Ions*, pp. 64 – 123. International series of monographs on physics. OUP Oxford, 2012.

[13] T. O. Tasci, I. Vargel, A. Arat, E. Guzel, P. Korkusuz, and E. Atalar. “Focused RF hyperthermia using magnetic fluids.” *Medical physics*, vol. 36, no. 5, pp. 1906 – 1912, 2009.

[14] H. Ling and S.-W. Lee. “Focusing of electromagnetic waves through a dielectric interface.” *JOSA A*, vol. 1, no. 9, pp. 965 – 973, 1984.

[15] D. P. O’Neal, L. R. Hirsch, N. J. Halas, J. D. Payne, and J. L. West. “Photo-thermal tumor ablation in mice using near infrared-absorbing nanoparticles.” *Cancer letters*, vol. 209, no. 2, pp. 171 – 176, 2004.

[16] A. J. Fenn, V. Sathiaseelan, G. A. King, and P. R. Stauffer. “Improved localization of energy deposition in adaptive phased-array hyperthermia treatment of cancer.” *Lincoln Laboratory Journal*, vol. 9, no. 2, 1996.

[17] G. R. Ter Haar. “High intensity focused ultrasound for the treatment of tumors.” *Echocardiography*, vol. 18, no. 4, pp. 317 – 322, 2001.

[18] D. Melodelima, W. A. N’Djin, A. Battais, S. Chesnais, M. Rivoire, and J.-Y. Chapelon. “Thermal ablation of liver tumors by high-intensity-focused ultrasound using a toroid transducer. Results of animal experiments.” In *Ultrasonics Symposium (IUS), 2009 IEEE International*, pp. 224 – 227. IEEE, 2009.

[19] D. Hoult and P. C. Lauterbur. “The sensitivity of the zeugmatographic experiment involving human samples.” *Journal of Magnetic Resonance (1969)*, vol. 34, no. 2, pp. 425 – 433, 1979.

[20] G. Adriany, V. de Moortele, F. Wiesinger, S. Moeller, J. P. Strupp, P. Andersen, C. Snyder, X. Zhang, W. Chen, K. P. Pruessmann, et al. “Transmit and receive transmission line arrays for 7 Tesla parallel imaging.” *Magnetic resonance in medicine*, vol. 53, no. 2, pp. 434 – 445, 2005.

[21] D. Andreuccetti, R. Fossi, and C. Petrucci. “An Internet resource for the calculation of the dielectric properties of body tissues in the frequency range 10 Hz–100 GHz.” Website, 2012. `http://niremf.ifac.cnr.it/tissprop/`, accessed 6-April-2013.

[22] S. Rast, P. H. Fries, E. Belorizky, A. Borel, L. Helm, and A. E. Merbach. “A general approach to the electronic spin relaxation of Gd(III) complexes in solutions. Monte Carlo simulations beyond the Redfield limit.” *The Journal of Chemical Physics*, vol. 115, no. 16, pp. 7554 – 7563, 2001.

[23] V. Atsarkin, V. Demidov, G. Vasneva, B. Odintsov, R. Belford, B. Radüchel, and R. Clarkson. "Direct measurement of fast electron spin-lattice relaxation: method and application to nitroxide radical solutions and Gd^{3+} contrast agents." *The Journal of Physical Chemistry A*, vol. 105, no. 41, pp. 9323 – 9327, 2001.

[24] A. Abragam. *The principles of nuclear magnetism.* International series of monographs on physics. Clarendon Press, 1961.

[25] B. Soher, C. Wyatt, S. Reeder, and J. MacFall. "Noninvasive temperature mapping with MRI using chemical shift water-fat separation." *Magnetic Resonance in Medicine*, vol. 63, no. 5, pp. 1238 – 1246, 2010.

[26] N. Oppenheimer and T. James. *Nuclear Magnetic Resonance.* No. v. 176 in Methods in enzymology. Academic Press, 1989.

[27] A. Borel, J. F. Bean, R. B. Clarkson, L. Helm, L. Moriggi, A. D. Sherry, and M. Woods. "Towards the Rational Design of MRI Contrast Agents: Electron Spin Relaxation Is Largely Unaffected by the Coordination Geometry of Gadolinium (III)–DOTA-Type Complexes." *Chemistry-A European Journal*, vol. 14, no. 9, pp. 2658 – 2667, 2008.

[28] M. F. Tweedle. "The ProHance story: the making of a novel MRI contrast agent." *European Radiology*, vol. 7, no. 5, pp. 225 – 230, 1997.

[29] C. Slichter. *Principles of Magnetic Resonance.* Springer Series in Solid-State Sciences. Springer, 1990.

[30] M. E. Pittman and D. L. Waidelich. "Three and four coil systems for homogeneous magnetic fields." *Aerospace, IEEE Transactions on*, vol. 2, no. 1, pp. 36 – 45, 1964.

[31] G. Gottardi, P. Mesirca, C. Agostini, D. Remondini, and F. Bersani. "A four coil exposure system (tetracoil) producing a highly uniform magnetic field." *Bioelectromagnetics*, vol. 24, no. 2, pp. 125 – 133, 2003.

[32] P. S. Morgan, S. Conolly, and A. Mazovski. "Design of uniform field biplanar magnets." In *5th Meeting of ISMRM*, p. 1447. 1997.

[33] L. L. Tsai, R. W. Mair, M. S. Rosen, S. Patz, and R. L. Walsworth. "An open-access, very-low-field MRI system for posture-dependent ^{3}He human lung imaging." *Journal of Magnetic Resonance*, vol. 193, no. 2, pp. 274 – 285, 2008.

[34] A. I. Zverev. *Handbook of filter synthesis.* Wiley, 1967.

[35] S. Eaton, G. Eaton, and L. Berliner. *Biomedical EPR: Free radicals, metals, medicine, and physiology*. Biological Magnetic Resonance. Kluwer Academic/Plenum Publishers, 2005.

[36] M. Ono, A. Suenaga, and H. Hirata. "Experimental investigation of RF magnetic field homogeneity in a bridged loop-gap resonator." *Magnetic resonance in medicine*, vol. 47, no. 2, pp. 415 – 419, 2002.

[37] W. Froncisz and J. S. Hyde. "The loop-gap resonator: a new microwave lumped circuit ESR sample structure." *Journal of Magnetic Resonance (1969)*, vol. 47, no. 3, pp. 515 – 521, 1982.

[38] EM Software & Systems - SA (Pty) Ltd. "FEKO." `www.feko.info`. 32 Techno Avenue, Technopark, Stellenbosch, 7600, South Africa, 2014.

[39] O. Ogunlade and P. Beard. "Electric and magnetic properties of contrast agents for thermoacoustic imaging." In *SPIE BiOS*, vol. 89432V. International Society for Optics and Photonics, 2014.

[40] Neoptix. "T1 fibre optic temperature probe.", 2014. URL `http://www.neoptix.com/t1-sensor.asp`.

[41] K. R. Holmes. "Thermal properties." *cortex (dog)*, vol. 491, p. 16, 2009.

[42] Elektro-Automatik. "EA-PS 8360-15 DT Laboratory power supply.", 2013. URL `http://shop.elektroautomatik.de/shop/`. Datasheet.

[43] HD Communications corp. "HD30031 Solid State Personal Communication Power Amplifier.", 2013. URL `www.rfamplifiers.com`. Datasheet.

[44] Magritek. "Terranova-MRI: Earth's Field MRI Teaching System.", 2013. URL `http://www.magritek.com/products/terranova/`. Overview.

[45] Cyromagnetics, inc. "NMR & EPR Systems." Website, 2016. `http://www.cryomagnetics.com/products/nmr-epr-systems/`, accessed 8-June-2016.

[46] D. Gadian and F. Robinson. "Radiofrequency losses in NMR experiments on electrically conducting samples." *Journal of Magnetic Resonance (1969)*, vol. 34, no. 2, pp. 449 – 455, 1979.

[47] B. Park, T. Neuberger, A. G. Webb, D. C. Bigler, and C. M. Collins. "Faraday shields within a solenoidal coil to reduce sample heating: Numerical comparison of designs and experimental verification." *Journal of Magnetic Resonance*, vol. 202, no. 1, pp. 72 – 77, 2010.

[48] M. Ono, K. Sha, M. Suzuki, T. Ogata, and E. Yoshida. "ESR spectrometer having split-ring resonator.", Jan. 5 1988. US Patent 4,717,880.

[49] Eutech Instruments. "ECTestr11+ portable conductivity meter.", Jan. 27 2016. URL `http://www.eutechinst.com/pdt-para-EC-ectestr11+.htm`.

[50] J. Andrade and M. Estévez-Pérez. "Statistical comparison of the slopes of two regression lines: a tutorial." *Analytica chimica acta*, vol. 838, pp. 1 – 12, 2014.

[51] P. O'Shaughnessy and J. E. Cavanaugh. "Performing T-tests to Compare Autocorrelated Time Series Data Collected from Direct-Reading Instruments." *Journal of occupational and environmental hygiene*, , no. 12, pp. 743 – 752, 2015.

[52] A. Elster and J. Burdette. *Questions & Answers in Magnetic Resonance Imaging*, pp. 32 – 33. Mosby, 2001.

[53] S. Rast, P. H. Fries, and E. Belorizky. "Static zero field splitting effects on the electronic relaxation of paramagnetic metal ion complexes in solution." *The Journal of Chemical Physics*, vol. 113, no. 19, pp. 8724 – 8735, 2000.

[54] S. Phounsavath. *RF heating of ultra-short single-walled carbon nanotubes and gadonanotubes for non-invasive cancer hyperthermia*. Ph.D. thesis, Rice University, Houston, Texas, January 2014.

[55] B. Sitharaman and L. J. Wilson. "Gadonanotubes as new high-performance MRI contrast agents." *international Journal of Nanomedicine*, vol. 1, no. 3, p. 291, 2006.

[56] R. Sethi, Y. Mackeyev, and L. J. Wilson. "The gadonanotubes revisited: a new frontier in MRI contrast agent design." *Inorganica Chimica Acta*, vol. 393, pp. 165 – 172, 2012.

[57] G. Morrell and A. Macovski. "Three-dimensional spectral-spatial excitation." *Magnetic Resonance in Medicine*, vol. 37, no. 3, pp. 378 – 386, 1997.

[58] A. A. Schricker, J. M. Pauly, J. Kurhanewicz, M. G. Swanson, and D. B. Vigneron. "Dualband spectral-spatial RF pulses for prostate MR spectroscopic imaging." *Magnetic resonance in medicine*, vol. 46, no. 6, pp. 1079 – 1087, 2001.

BIBLIOGRAPHY

[AB12] A. Abragam and B. Bleaney. *Electron Paramagnetic Resonance of Transition Ions.* International series of monographs on physics. OUP Oxford, 2012.

[Bra66] F. Brailsford. *Physical Principles of Magnetism.* London, 1966.

[Kra02] W. Krause. *Contrast Agents I: Magnetic Resonance Imaging.* Contrast Agents. Springer, 2002.

[Lev01] M.H. Levitt. *Spin dynamics: basics of nuclear magnetic resonance.* John Wiley & Sons, 2001.

[LL00] Z.P. Liang and P.C. Lauterbur. *Principles of magnetic resonance imaging.* IEEE press New York:, 2000.

[Mor65] A.H. Morrish. *The physical principles of magnetism.* Wiley series on the science and technology of materials. Wiley, 1965.